

DOCTORAL THESIS IN PHYSICS

**The magnetic shape memory alloy Ni-Mn-Sn in
thin films**

Alexander Auge

Department of Physics
University of Bielefeld

July 2012

Declaration

I wrote this thesis by myself and used none but the indicated resources. Text and figures were partly taken from corresponding publications, which originate directly from this work.

Bielefeld, July 2012

(Alexander Auge)

Reviewers

Prof. Dr. Andreas Hütten

Prof. Dr. Thomas Huser

Date of submission: July 2012

Dedicated to the curious

Publications

- [1] A. Auge, A. Weddemann, F. Wittbracht, A. Hütten: Magnetic ratchet for biotechnological applications; *Appl. Phys. Lett.* 94, 183507 (2009)
- [2] A. Weddemann, F. Wittbracht, A. Auge, A. Hütten: A hydrodynamic switch: Microfluidic separation system for magnetic beads; *Appl. Phys. Lett.* 94, 173501 (2009)
- [3] C. Albon, A. Weddemann, A. Auge, A. Hütten: Tunneling magnetoresistance sensors for high resolute particle detection; *Appl. Phys. Lett.* 95, 023101 (2009)
- [4] C. Albon, A. Weddemann, A. Auge, D. Meißner, K. Rott, P. Jutzi, A. Hütten: Number sensitive detection and direct imaging of dipolar coupled magnetic nanoparticles by tunnel magnetoresistive sensors; *Appl. Phys. Lett.* 95, 163106 (2009)
- [5] A. Weddemann, A. Auge, C. Albon, F. Wittbracht, A. Hütten: On the resolution limits of tunnel magnetoresistance sensors for particle detection; *New J. Phys.* 11 113027 (2009)
- [6] A. Weddemann, A. Auge, D. Kappe, F. Wittbracht, A. Hütten: Dynamic simulations of the dipolar driven demagnetization process of magnetic multi-core nanoparticles; *J. Magn. Magn. Mater.* 322, 643-646 (2009)
- [7] A. Auge, A. Weddemann, B. Vogel, F. Wittbracht, A. Hütten: A level set based approach for modeling oxidation processes of ligand stabilized metallic nanoparticles; *Appl. Phys. Lett.* 96, 093111 (2010)

- [8] A. Weddemann, B. Eickenberg, F. Wittbracht, A. Auge, A. Hütten: A combined reaction-separation lab-on-a-chip device for low Peclet number applications; *J. Appl. Phys.* 106, 024510 (2009)
- [9] A. Weddemann, F. Wittbracht, A. Auge, A. Hütten: Positioning system for particles in microfluidic structures; *Microfluid Nanofluid* 7, 849-855 (2009)
- [10] A. Weddemann, A. Auge, C. Albon, F. Wittbracht, A. Hütten: Toward the magnetoresistive detection of single magnetic nanoparticles: New strategies for particle detection by adjustment of sensor shape; *J. Appl. Phys.* 107, 104314 (2010)
- [11] O. Schebaum, D. Drewello, A. Auge, G. Reiss, A. Thomas: Tunnel magnetoresistance in alumina, magnesia and composite tunnel barrier magnetic tunnel junctions; *J. Magn. Magn. Mater.* 323, 1525-1528 (2011) DOI: 10.1016/j.jmmm.2011.01.011
- [12] A. Weddemann, F. Wittbracht, A. Auge, A. Hütten: Particle flow control by induced dipolar interaction of superparamagnetic microbeads; *Microfluid Nanofluid* 10, 459-463 (2011)
- [13] A. Weddemann, C. Albon, A. Auge, P. Hedwig, D. Akemeier, K. Rott, D. Meißner, P. Jutzi, A. Hütten: How to design magneto-based total analysis systems for biomedical applications; *Biosensors & Bioelectronics* 26, 1152-1163 (2010)
- [14] I. Ennen, S. Löffler, C. Kübel, D. Wang, A. Auge, A. Hütten, P. Schattschneider: Site-specific chirality in magnetic transitions; *J. Magn. Magn. Mater.* 324, 2723-2726 (2012)
- [15] A. Auge, N. Teichert, M. Meinert, G. Reiss, A. Hütten, E. Yüzüak, I. Dincer, Y. Elerman, I. Ennen, and P. Schattschneider: Thickness dependence of the martensitic transformation, magnetism, and magnetoresistance in epitaxial Ni-Mn-Sn ultrathin films, *Phys. Rev. B* 85, 214118 (2012)

Conferences

- [1] A. Auge, T. Weiß, D. Akemeier, F. Wittbracht, A. Weddemann, A. Hütten: Micro total analysis system: A combination of a magnetic ratchet with giant magnetoresistance sensors; Biosensors 2010, Edinburgh, Great Britain
- [2] A. Auge, A. Weddemann, B. Vogel, F. Wittbracht and A. Hütten: Oxidation of metallic nanoparticles; Comsol Conference 2009, Mailand, Italy
- [3] A. Auge, N. Teichert, M. Meinert, I. Ennen, I. Dincer, E. Yuzuak, Y. Elerman, A. Hütten: Martensitic transformation and magnetoresistance in off-stoichiometric Ni-Mn-Sn thin films; Intermag 2011, Taipeh, Taiwan
- [4] A. Auge, N. Teichert, M. Meinert, I. Ennen, I. Dincer, E. Yuzuak, Y. Elerman, I. Ennen, P. Schattschneider, A. Hütten: Martensitic transformation and electron energy loss magnetic chiral dichroism in off-stoichiometric Ni-Mn-Sn thin films; APMAS 2011, Antalya, Turkey
- [5] A. Auge, N. Teichert, A. Hütten: Phase Field Simulations of Martensitic Transformation in Thin Films; DPG 2012, Berlin, Germany

Contents

Publications	iv
Conferences	vi
Contents	vii
1 Introduction	1
2 Fundamental Basics of Martensitic Transformations	5
2.1 Introduction	5
2.2 Phase Compatibility	15
2.3 Martensitic Transformation in real crystals and thin films	16
2.4 Summary	18
3 Analytical and preparation tools	20
3.1 Thin film deposition	20
3.2 X-Ray Diffraction and Reflectometry	21
3.3 Chemical composition analysis by X-Ray Fluorescence	23
3.4 Electric transport measurements	23
3.5 Magnetic Measurements	23
4 Phase Field Simulations	24
4.1 Phase field model	25
4.2 Implementation	27
4.3 Simulations of thin films - Geometry, approximations and solution	28
4.4 Summary and Discussion	35

5	Ni-Mn-Sn in thin films	37
5.1	Introduction	37
5.2	Structure in the austenite phase: thin film quality	41
5.3	Martensitic structure	47
5.4	Magnetism	63
5.5	Electrical transport	68
5.6	Analysis of the martensitic transformation	75
5.7	Origins of the transformation behavior	79
5.8	Magnetoresistance	87
6	Summary and Conclusions	95
7	Outlook	98
	Bibliography	99
8	Danksagung	111

1 Introduction

The functional behavior of shape memory alloys as used for, e.g., actuators and switching devices, is related to the structural instability known as martensitic transformation (MT). It is defined as a displacive, diffusionless first-order solid to solid phase transformation from the high temperature austenite to the low temperature martensite phase. Ferromagnetic shape memory alloys (FSMA) are materials that combine the shape memory effect and ferromagnetic behavior. The Heusler alloys Ni_2MnGa and off stoichiometric $\text{Ni}_{50}\text{Mn}_{25+x}\text{Z}_{25-x}$, where $Z=\text{In, Sn, Sb}$, are important examples of FSMA due to their interesting physical phenomena such as large magnetic field induced strain,[1] giant magnetocaloric effects,[2] and giant magnetoresistance.[3]

For applications such as actuators, magnetic cooling and hybrid systems, thin films are often advantageous or mandatory. It was shown that shape memory alloys in thin films can be used as microfluidic valves, micropumps and microgrippers.[4] For magnetic cooling devices, thin films offer the advantage of a high surface to volume ratio. This allows a fast heat transfer.

A general knowledge of the thin film influence on the MT is required for all these applications. Theoretical and experimental studies have shown, that the transformation behavior as well as the microstructure changes significantly in thin films.[5, 6] In investigations on the transformation behavior, a broader transition and a change in the transition temperatures has been found. The broadening of the transition as well as a reduced transition temperature can be caused by substrate constraints,[7] confinement of the nucleus and size scale effects on the the mean free path of transformation dislocations.[6] An increase in the transition temperature can be attributed to stress induced by the lattice mismatch between substrate and thin film.[5]

1. INTRODUCTION

The details of the microstructure depend strongly on material properties and external influences. In thin films the substrate as well as induced texture play a major role. The degree and kind of texture has a large influence on the allowed variants.[8] A rigid substrate leads to symmetry breaking effects in the sense that not all orientations of the austenite-martensite interfaces allow coarsening of nanotwinned martensite to macroscopic non modulated variants. [9]

Systematic studies on the influence of the film thickness on the MT are sparse in literature. Epitaxial Ni-Mn-Ga films have been investigated in the thickness range of 150 nm to 500 nm with varying composition.[9] An increasing influence of the substrate with decreasing thickness has been found due to stress induced martensite at the interface. Polycrystalline Ni-Mn-Sn films grown on Si have been investigated in the thickness range from 120 nm up to 2.5 μm by Vishnoi *et al.* [10] They found a suppression of the MT below 410 nm and an increasing transition temperature with increasing film thickness. Most other studies on the MT in thin films investigated a single film thickness in the range of several 100 nm up to several μm . [5, 11, 12, 13, 14]

This work has theoretical as well as experimental aspects. At first, phase field simulations are carried out for the well known model system NiAl in thin films. This allows us to study the influence of a rigid substrate on the martensitic transformation and the involved energy terms for different film thicknesses. The second part of this thesis involves experimental studies of Ni-Mn-Sn. This is a Heusler alloy with a very low lattice mismatch of 0.7% with respect to MgO.[15] Thus, a low stress influence can be expected and this system should be an ideal candidate to study the influence of confinement and size scale effects. Two sample series with different composition in the thickness range of 200 nm down to 10 nm are investigated using temperature dependent X-ray diffraction, magnetization and resistivity measurements.

This thesis is organized as follows:

1. Theoretical Basics: The martensitic transformation is introduced. The basics of martensitic structures, the involved energy terms and the origin of the microstructure is explained. The influence of phase compatibility, sample quality and the thin film geometry on the phase transition is introduced.

-
2. Analytical and preparation tools: The tools used in this work are shortly introduced. The emphasis lies on the specifications and limitations.
 3. Phase field simulations: This chapter has two main sections. In the first section the phase field method and its implementation into the finite element package COMSOL MULTIPHYSICS is introduced. The simulation results on the influence of the film thickness on the martensitic transformation are given in the following.
 4. Ni-Mn-Sn in thin films: This is the experimental chapter of this thesis. It involves the following sections:
 - a) Introduction: A general introduction into Heusler compounds is given. In the following the two sample series investigated in this work are described and the relation to previous work in bulk systems is given.
 - b) Structure in the austenite phase: thin film quality. This section involves the austenitic structure. This gives insight into the thin film quality which has a large impact on the transformation behavior.
 - c) Martensitic structure: The martensitic structure is investigated using temperature dependent X-ray diffraction measurements. The type of martensitic structure also plays a major role for the transformation characteristics.
 - d) Magnetism: The magnetism of the thin films is discussed and compared to available bulk data.
 - e) Electric transport: Resistivity measurements are conducted. They give insight into the transformation characteristics and the amount of residual austenite. This corresponds to the suppression of the transformation at the rigid substrate.
 - f) Analysis of the martensitic transformation: The details of the martensitic transformation are analyzed using the resistivity measurements.
 - g) Origins of the transformation behavior: The experimental available data is summarized. At last, the origins of the transformation behavior is discussed.

1. INTRODUCTION

- h) Magnetoresistance: The magnetoresistance combines resistivity, magnetism and the martensitic transformation and thus gives a overview about most prior discussion. It is also a well suited method to study the influence of a magnetic field on the MT.

2 Fundamental Basics of Martensitic Transformations

Abstract

In this chapter the theoretical basics important to understand all aspects of this work are presented. Theoretical concepts that are important for single chapters only are presented accordingly. In the first section, fundamental properties of the martensitic transformation are introduced. The concept of phase compatibility is introduced in the following section. In the last section, the influences of defects and the thin film geometry on the martensitic transformation are discussed. Note that not all details that are required for understanding can be presented in this thesis. It is assumed that the reader is accustomed to basic linear elasticity and continuum mechanics. A good introduction about both topics can be found in e.g. [16]. Further reading about martensitic transformations can be found in e.g. [8] and [17].

2.1 Introduction

The martensitic transformation is defined as a displacive, diffusionless first-order solid to solid phase transition from the high temperature austenite to the low temperature martensite phase. The first studies on martensitic transformations were undertaken by Adolf Martens on steels at the end of the 19th century. The name "martensite" was used to describe the microstructure found in quenched steels. The γ phase in steel above the critical eutectoid temperature was described as austenite, named after Sir William Chandler Roberts-Austen.

2. FUNDAMENTAL BASICS OF MARTENSITIC TRANSFORMATIONS

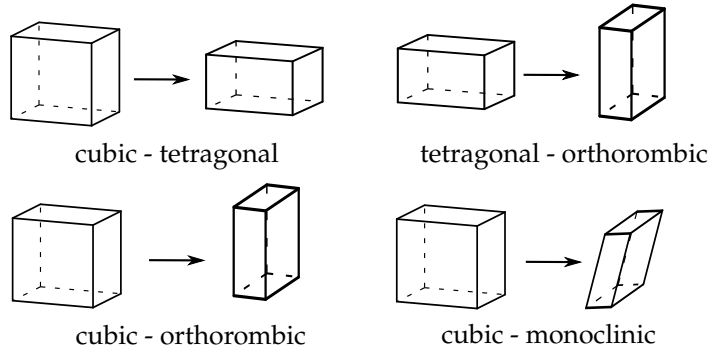


Figure 2.1: Typical examples of martensitic transformations.

Other than in steels, martensitic transformations occur in various other types of materials such as nonferrous alloys, ceramics, minerals, polymers, etc.

There are many possible types of austenite to martensite phase transformations: e.g. cubic to tetragonal, tetragonal to orthorhombic, cubic to orthorhombic and cubic to monoclinic as shown in Figure 2.1. The transformation from austenite to martensite can be expressed by the Bain or transformation matrix using the infinitesimal strain theory approximation.[8] The Bain matrix for a typical example of an austenite to martensite transformation, cubic to tetragonal, is shown in Figure 2.2. The transformation involves a change from the cubic lattice constant a_0 to the tetragonal lattice constants a and b . The relationship between these is described by the Bain matrix. Thus, during the transformation, one of the cubic axes is stretched (compressed), while the other two are compressed (stretched). If a compression or a stretch applies depends on the material. Three different orientations of the tetragonal structure in relation to the cubic austenite are possible. In Figure 2.2 this is shown by b pointing along the x , y or z axis. These three different orientations are referred to as variants of martensite. Due to symmetry relations of the crystal lattice, only a limited number of variants exists for each type of transformation. The number of martensitic variants n is given by:[8]

$$n = \frac{\text{the number of rotations in } \mathcal{P}_A}{\text{the number of rotations in } \mathcal{P}_M} \quad (2.1)$$

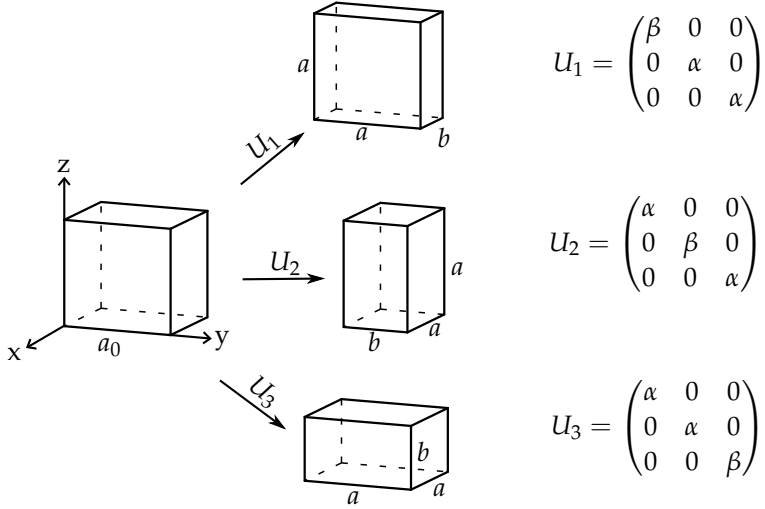
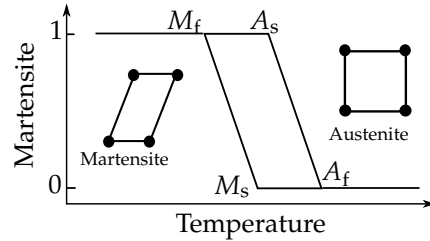


Figure 2.2: One example of an austenite to martensite transformation, cubic to tetragonal, is shown. U_1, U_2, U_3 are the Bain matrices for the three possible martensitic variants. The relation of the lattice constants of the cubic and tetragonal phase is given by $\alpha = a/a_0$ and $\beta = b/a_0$.

where \mathcal{P}_A and \mathcal{P}_M are the point groups of the austenite and of the martensite structure, respectively. Two examples are $n = 24/8 = 3$ for cubic to tetragonal and $n = 24/4 = 6$ for the cubic to orthorhombic transformation.

The martensitic phase transformation is virtually independent of time. The growth rate is close to the speed of sound in a solid and thus the transformation is very rapid.[17] However, the amount of transformation is characteristic of temperature, if other variables such as grain size are constant. On cooling, the *forward* transformation from austenite to martensite starts at the martensite start temperature (M_s) and finishes at the martensite finish temperature (M_f). The martensitic transformation is reversible so that the initial atomic configuration can be repeatedly obtained. The reversibility is associated with a temperature hysteresis due to energy losses. The *reverse* transformation from martensite to austenite begins at a temperature above M_s called austenite start

Figure 2.3: The hysteresis of a martensitic transformation.



(A_s) and completes at the austenite finish (A_f) temperature. This temperature dependence of the martensitic transformation is shown in Figure 2.3

Energetics of the martensitic phase transformation

The driving force ΔG of the martensitic transformation is the difference between the Gibbs energies of austenite G^A and martensite G^M :

$$\Delta G = G^A - G^M \quad (2.2)$$

The Gibbs energy itself is given by:

$$G = U + pV - TS \quad (2.3)$$

where U is the internal energy, p the pressure, V the volume, T the temperature and S the entropy.

The Gibbs energy offers a simple explanation on why the austenite is stable at high temperatures and low pressures[18]: Typically, the transformation from the austenite to the martensite structure leads to an increased density. The lower volume will lead to a lower value of U and pV at constant pressure. Due to the compact nature of the martensite, the phonon frequencies will be slightly higher than in the austenite. This leads to a lower entropy in the martensite phase. At low temperatures, the Gibbs energy is dominated by the enthalpy $H = U + pV$. Both values, U and V are lower in the martensite phase than in the austenite. Thus the martensite is favored at low temperatures and high pressures. On heating, TS becomes dominant. Due to the higher entropy in the austenite, a transition from martensite to austenite occurs.

The Gibbs energy can be divided into two parts: the chemical Gibbs energy G_c and the non-chemical Gibbs energy G_{nc} . The main contribution to G_{nc}^M is

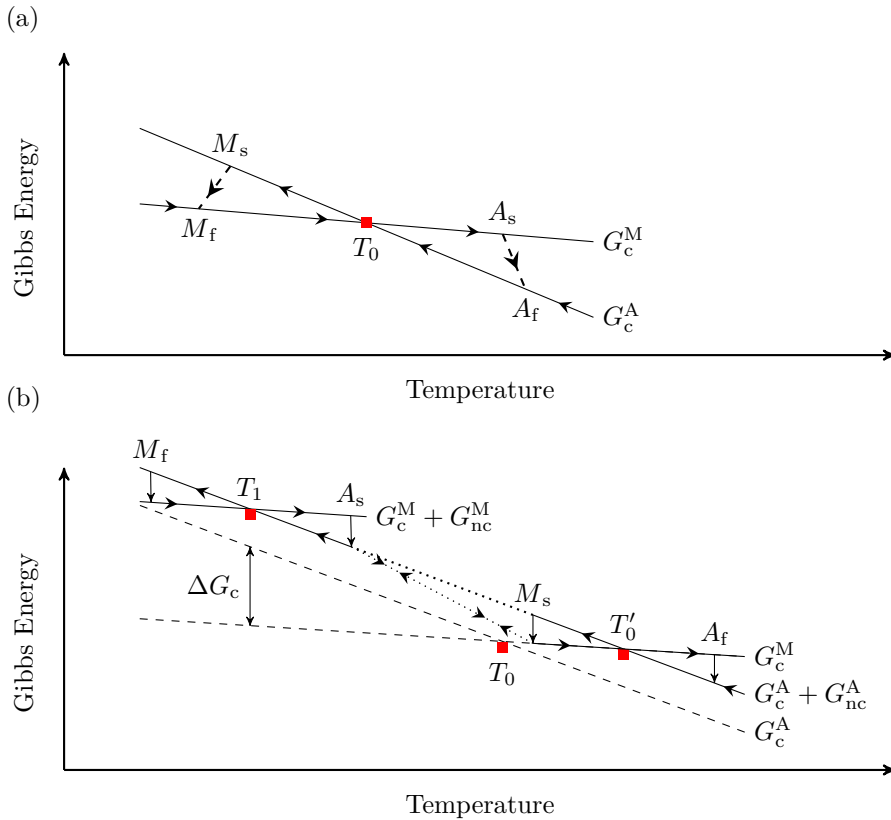


Figure 2.4: Energy diagram sketches of the Gibbs energy G . M_s/A_s and M_f/A_f mark the martensite/austenite start and finish temperatures. The arrows show the transformation path. In (a) the energy diagram for the example of low non-chemical energy G_{nc} is presented. G_c^M and G_c^A are the chemical energies of the martensite and austenite, respectively. In (b) large undercooling is present and non-chemical energy plays an important role. The dotted lines indicate the jump between the first and the last fraction of martensite that is formed during the forward transformation. The same applies for the reverse transformation for the austenite fractions.

2. FUNDAMENTAL BASICS OF MARTENSITIC TRANSFORMATIONS

elastic energy stored during the transformation. G_{nc}^A can be understood as strained austenite due to an applied stress.

The details of the temperature dependence of the transformation in terms of the Gibbs energy are discussed in the following: The response to a temperature change during the MT depends on the contribution of the non-chemical energy. Two examples, low G_{nc} and high G_{nc} contribution, are depicted in Figure 2.4. In the first example, shown in Figure 2.4 (a), the non-chemical energy has little influence on the transition. At high temperatures, the material is in the austenite phase. With decreasing temperature the energy difference between austenite and martensite reduces. At T_0 the chemical Gibbs energy of both phases is equal. Upon further cooling the material starts to transform at M_s from the austenite to the martensite. The temperature difference between T_0 and M_s corresponds to the activation energy required to initiate the transformation. This activation energy for nucleation consists of, e.g., interface energy of the martensitic nucleus and strain energy due to the deformations.[19] The temperature difference required to finish the transformation is called undercooling/overheating for the forward/reverse transformation. Upon heating, the material is in the martensite phase up to A_s . At this temperature the energy difference is sufficient to initiate the reverse transformation. At A_f the transformation is finished.

In the second example, non-chemical energies have a large influence on the transformation. The non-chemical energy G_{nc}^M of the martensite phase depends on the degree of the transformation. For clarity, only the beginning and the end of the transformation are discussed. G_{nc}^M is not present at the beginning of the transformation and the complete G_{nc}^M is present at the end of the transformation. In other word, the transformation occurs in small fractions, where only the first and the last fraction is discussed. This is shown in Figure 2.4 (b). At high temperatures the austenite is stable. Compared to the first example, M_s is shifted to a higher temperature. This is caused by the shift of G^A to higher energies due to an applied stress which increases G_{nc}^A . T'_0 marks the temperature where the G_c^M and $G_c^A + G_{nc}^A$ are equal. In the beginning of the forward transformation G_{nc}^M is not present. Thus, similar as in the first example, the transformation starts at M_s . Here, the first fraction of martensite is formed. This martensite leads to non-chemical energy G_{nc}^M . Upon further cooling the fraction of martensite and G_{nc}^M increase. Thus, each additional fraction of martensite requires additional energy to overcome the

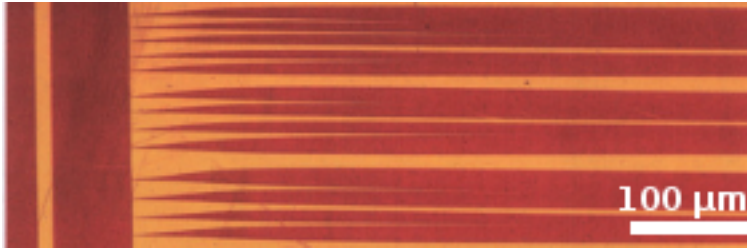


Figure 2.5: Optical micrograph of a typical martensitic microstructure in Cu-Al-Ni.[8] Each color corresponds to a variant.

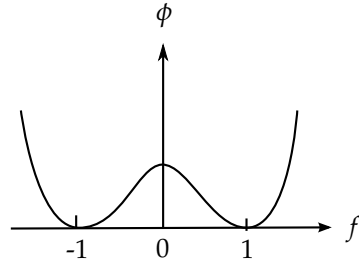
non-chemical energy. The jump from the first fraction of martensite to the last fraction of martensite that is formed is depicted as dotted line. At low temperatures, the transformation is almost complete. The total Gibbs energies are equal ($G_{nc}^A + G_c^A = G_{nc}^M + G_c^M$) at the temperature T_1 . G_{nc}^M is the accumulated non-chemical energy. T_1 is called thermoelastic equilibrium. ΔG_c indicates the additional chemical energy to reach the thermoelastic equilibrium. At M_f , the last fraction of martensite is formed and the transformation is finished. The temperature difference between T_1 and M_f is due to the required energy to overcome the energy barrier for this last fraction. Upon heating, the reverse transformation starts at A_s . Here, the first fraction of austenite is formed. With further increasing temperature, the austenite fraction increases and G_{nc}^M reduces. At A_f , the last fraction of austenite is formed.

Microstructure

The martensitic microstructure is the most characteristic observable feature of the martensitic phase transformations (see Figure 2.5). The kind of complex pattern formed by martensitic variants and their size scale depend on several factors such as material, grain size, specimen size, internal and external stresses, structural defects and the history of the sample.[8]

The origin of the microstructure can be understood in the following way[8]: a martensitic material with e.g. two variants has a multi-well energy as shown in Figure 2.6. Each variant corresponds to one of the energy wells. Consider now this material subjected to a boundary condition, e.g. an interface to a

Figure 2.6: The energy density ϕ vs. the transformation gradient f in the one dimensional example. Each energy well corresponds to one variant.



different material or austenite. Energetically, the material wants to be close to one of the wells. If the boundary condition corresponds to one of the energy wells, the material can easily accommodate one of the variants. Thus, the lattice constants fit. However, if the boundary condition is unequal to any single variant, but fits to the average value of the two variants, then the material can satisfy this boundary condition only by creating a mixture of these variants. E.g. one variant has a larger, the other a smaller lattice constant than the boundary condition. If we average over the two, the lattice constant fits. The total energy goes to zero, if this mixture of the two variants becomes very fine, i.e. the number of regions of each variant approaches infinity. However, there is also an interface energy between the variants, which increases with finer structures. The mixture of variants cannot be arbitrary because of the kinematic compatibility condition; it is given by the following equation:[8]

$$\mathbf{F} - \mathbf{G} = \mathbf{a} \otimes \hat{\mathbf{n}} \quad (2.4)$$

where \mathbf{F} and \mathbf{G} are constant matrices, \mathbf{a} is the shear direction, and $\hat{\mathbf{n}}$ is the normal of the interface plane. This condition is visualized in Figure 2.7. The important feature is an invariant plane between the two areas described by \mathbf{F} and \mathbf{G} . This is basically the condition for an unbroken body under shear and the interface is called coherent. In a slightly different form, this kind of equation is called twinning equation:[8]

$$\mathbf{Q}_1 \mathbf{U}_I - \mathbf{Q}_2 \mathbf{U}_J = \mathbf{a} \otimes \hat{\mathbf{n}} \quad (2.5)$$

where \mathbf{U}_J , \mathbf{U}_I are some constant matrices and \mathbf{Q}_1 , \mathbf{Q}_2 are some rotations.

Thus a combination of a multi-well energy, boundary conditions, kinematic compatibility and interface energy leads to the microstructure observed in martensitic materials.

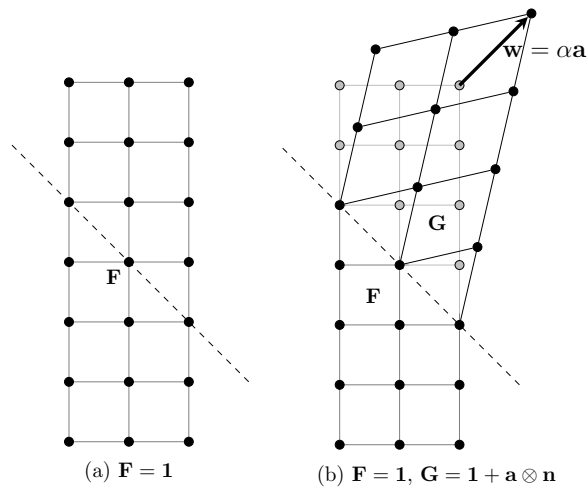


Figure 2.7: The kinematic compatibility condition. In (a) without lattice transformation. (b) A lattice transformation has been applied to part of the structure. The dashed line indicates the invariant plane.

The interface of the austenite to the martensite phase, also called *habit plane*, is an important special case of the microstructures. It is schematically shown in Figure 2.8 (a). In (b) the relevant matrices and vectors to describe the interface are shown. \mathbf{A} , \mathbf{B} describe the two variants. \mathbf{C} is the matrix of the austenite phase. λ describes the variant fraction required to fulfill the kinematic boundary condition. n is the number of deformations. α/n describes a transition range from the austenite to the twinned structure. $\hat{\mathbf{m}}$ is the orientation of the austenite-martensite interface. In Figure 2.9 a typical austenite-martensite interface is shown.

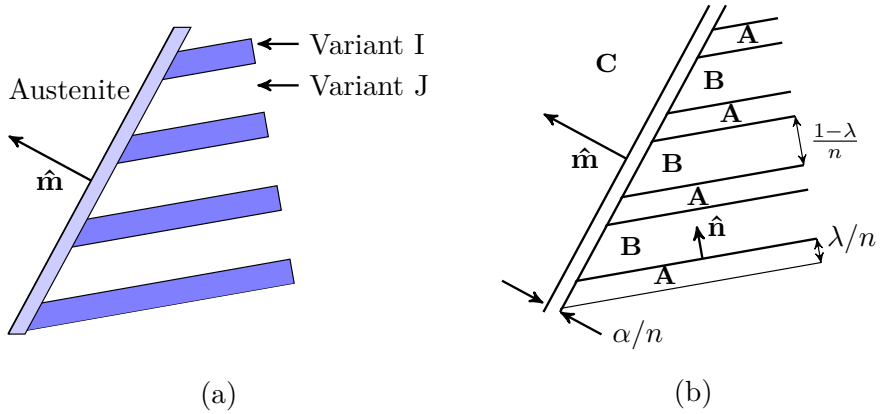


Figure 2.8: A typical austenite-martensite interface is shown in (a). The sequence of deformations that describe this interface is shown in (b). **A**, **B** describe the two variants. **C** is the matrix of the austenite phase. λ is the variant fraction required to fulfill the kinematic boundary condition. n is the number of deformations. α/n describes a transition range from the austenite to the twinned structure. \hat{m} is the orientation of the austenite-martensite interface. Adapted from [8].

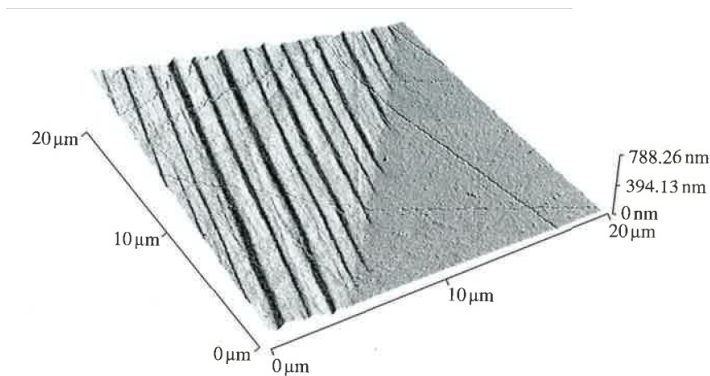


Figure 2.9: The austenite-martensite interface in Cu-Al-Ni. Taken from [8].

2.2 Phase Compatibility

The phase compatibility, also called geometric compatibility between martensite and austenite, is a measure for how well the martensite fits to the austenite. In other words, if the phases are compatible, only one single variant of martensite is required to fulfill the boundary condition to the austenite. The phase compatibility is given if $\lambda_2 = 1$, where λ_2 is the eigenvalue of the transformation stretch or Bain matrix \mathbf{U} with $\lambda_1 \leq \lambda_2 \leq \lambda_3$. For an example of a transformation stretch matrix see section 2.1. If martensite and austenite are not compatible, $\lambda_2 \neq 1$, a fine mixture of laminate twins is generated as shown in Figure 2.8 and 2.9. This fine laminate mixture is approximately compatible with the austenite, but it also involves elastic energy and interfacial energy between the variants. This energy barrier has to be overcome during the forward and reverse transformation, thus giving rise to a transformation hysteresis. An analytical form of the hysteresis width ΔH has been derived by Zhang *et al.* [20]

$$\Delta H = \frac{2\lambda T_e}{q} \sqrt{\frac{2\kappa\mu(1-\lambda)\xi}{l_c}} \quad (2.6)$$

where μ the elastic modulus, λ a scalar determining the twin fraction and κ the interfacial energy density of twins. ξ is a geometric factor measuring in a rough way the effect of different twin systems on the elastic energy stored in the austenite/martensite interface. l_c is the typical length of the austenite/martensite interface determined by the typical defect distance. T_e is the temperature where the austenite and martensite fractions are equal. q is the transformation heat. λ is approximately given by:

$$\lambda(\lambda_2) \approx \frac{1}{2} - \frac{1}{2} \sqrt{1 - \frac{4|\lambda_2 - 1|}{|a_2 n_2|}} \quad (2.7)$$

where a_2 and n_2 are the second entries of the vectors \mathbf{a} and \mathbf{n} of the twinning equation 2.5.

This influence has been experimentally verified by Cui *et al.* [21] and can be explained in the framework of the geometric nonlinear theory of martensite.[22, 8]

2.3 Martensitic Transformation in real crystals and thin films

Crystal Quality

The martensitic transformation in real crystals depends to a large degree on its quality. It is determined by the number of defects which can be of point (0D), line (1D), planar (2D) or precipitate (3D) type. Generally, such defects affect the martensitic nucleation and growth. The activation barrier for martensitic nucleation is reduced by defects due to their local strain fields. This leads to local variations of the transition temperature as e.g. determined by Malygin for dislocations[23] and precipitates.[24] The nucleation of martensite especially occurs at complex structural defects like interphase boundaries, free surfaces of aggregations of point defects.[25] Grain boundaries itself hinder the nucleation, however they are sources of dislocations which itself promote the martensitic nucleation.[26]

While defects promote the nucleation, the growth process is hindered by it. In a perfect crystal a nucleation center could transform the entire volume of the crystal, if the bulk energy is larger than the surface energy. However, in a real crystal the growth is stopped at defects and additional energy, corresponding to a small temperature change, is required to overcome the obstacle. Malygin [27] derived the following relation between the concentration of defects C and the transformation range $\Delta\tau$:

$$\Delta\tau = \frac{3k_B T_e^2}{\pi q r^3} C \quad (2.8)$$

where r is the radius of obstacles, k_B the Boltzmann constant, T_e is the temperature where the austenite and martensite fractions are equal and q is the transformation heat. Thus, $\Delta\tau$ is larger the higher the obstacle concentration and the smaller the obstacle radius. The nucleus growth advances further via motion of steps with height h and distance Λ along interfaces. Λ can thus be understood as mean free path of transformation dislocations, which is influenced by the alloy structure and the concentration of defects. The defects also lead to hysteresis due to frictional effects and they also influence the length scale of the martensite/austenite interface as discussed in section 2.2.

Size scale effects due to grain size or film thickness

Size scale effects due to grain size or film thickness have influence on the transition range and temperature. One model proposed by Malygin[28, 6] is based on smeared martensitic transitions, which takes into account thermodynamic factors influencing the phase equilibrium and structural effects affecting the kinetics of the transition. The structural effects can be understood as follows: If the film thickness or grain size has the same size scale as the mean free path of transformation dislocations Λ , the additional barriers will influence the kinetics of the transformation. The phase equilibrium, i.e. the thermodynamics of the transition, is influenced by the effective size of the martensitic nucleus ω . It is assumed that the nucleus in absence of size effects is disc-shaped with a diameter l , a height $a \ll l$ and a volume $\omega_0 = \pi a l^2/4$. The effective size of the nucleus ω is influenced by the grain size d and the film thickness h :

$$\omega = \frac{\omega_0}{1 + (l/d)^2 + l/h} \quad (2.9)$$

Taking the thermodynamics and the kinetics of the martensitic transformation into account, it is possible to derive relationships for T_e and the transformation range $\Delta\tau$. The relation for T_e is given by:

$$T_e = T_{e0} \left[1 + \frac{k_B T_{e0}}{q\omega} \times \ln \left(\frac{2k_0}{1 - k_a/3 + \Lambda/d + \Lambda/h} - 1 \right) \right] \quad (2.10)$$

where T_{e0} is the thick film limit of the equilibrium temperature, q the transformation heat, k_0 the relative density of drains (sources) for transformation dislocations, k_a is the annihilation coefficient for steps with different signs. The width of the martensitic transformation is given by:

$$\begin{aligned} \Delta\tau = \Delta\tau_0 & \left(1 + \left(\frac{l}{d} \right)^2 + \frac{l}{h} \right) \\ & \times \left[1 + \frac{k_B T_{e0}}{q\omega} \times \ln \left(\frac{2k_0}{1 - k_a/3 + \Lambda/d + \Lambda/h} - 1 \right) \right]^2 \end{aligned} \quad (2.11)$$

Here $\Delta\tau_0$ is the transformation width in the thick film limit.

However, not only thermodynamic and kinetic effects as proposed by Malygin play a role. Additional energy terms due to grain/interphase boundaries

and strain energies, as calculated by Meng *et al.* [19], can influence the grain size dependence of the transition. With decreasing grain size, an increase in the activation energy as well as a larger critical nucleus size has been found. The impact of this effect depends on the strain energy as well as the interphase energy of the material.

Rigid Substrate

Additionally to the limitation of the film thickness, a rigid substrate can influence the MT: It leads to a suppression of the MT due to the elastic energy required to transform the substrate. This is investigated in detail using phase field simulations (see chapter 4). The closer the MT to the substrate, the larger the needed additional energy in form of undercooling. This can lead to significant undercooling and nonlinearity of the transition.

2.4 Summary

The main characteristics of a martensitic transformation are summarized below:

- Dependence on time: The amount of transformation is virtually independent of time. At a constant temperature, a fraction of the austenite transforms very rapidly, after which there is no further change.
- Dependence on temperature: The transformation on cooling begins spontaneously at a fixed temperature called martensite start (M_s) and as the temperature decreases more material transforms until the transformation is complete at a temperature called martensite finish (M_f).
- Reversibility of the transformation: Martensitic reactions are very reversible in the sense that an initial atomic configuration can be repeatedly obtained. The reversibility is associated with a temperature hysteresis due to energy losses and the reverse reaction begins at a temperature above M_s called austenite start (A_s) and completes at the austenite finish (A_f) temperature.
- Effect of applied stress: Applied stress stabilizes the martensite phase.
- Nucleation and growth: The nucleation is a heterogeneous process with nucleation centers at defects and other stress concentrators.

- **Microstructure:** A characteristic feature of the martensitic transformation is the emergence of a microstructure. The exact form of the microstructure depends strongly on the type of system, but it is always a result of an energy minimization. A multi well energy is the requirement for the formation of a microstructure.
- **Size scale effects:** The transformation can be hindered by defects and confinement of the martensitic nucleus, if the characteristic defect distance and/or the martensitic nucleus are on the same size scale as the grain size or film thickness.
- **rigid substrate:** A rigid substrate hinders the transformation due to the necessary energy to strain it.

3 Analytical and preparation tools

Abstract

This chapter gives a brief introduction into the devices and techniques of preparation and characterization of the thin films studied in this work. All samples were prepared by DC and RF magnetron co-sputtering and electron beam evaporation. The structural characterization of the films was performed by x-ray diffraction and reflectivity measurements. The chemical composition analysis was done by hard x-ray fluorescence. Electric transport measurement were performed in a standard four point setup.

3.1 Thin film deposition

All thin film samples presented in this work were deposited by DC and RF magnetron co-sputtering on MgO substrates with (001) orientation. The sputter machine used for the deposition is customly designed and built by BESTEC , BERLIN. A cross section of the sputter system is shown in Figure 3.1. The base pressure of the vacuum chamber is typically better than 5×10^{-9} mbar. It is equipped with five DC and two RF three-inch magnetron sputter sources and an electron beam evaporator. The sources are placed in a confocal sputter-up geometry. The inclination of the sources is 30° with a target to substrate distance of 21 cm. The sample carrier can be rotated with up to 30 rpm to obtain a homogeneous thickness and stoichiometry across a diameter of about 100 mm. It can be radiatively heated with a ceramic heater with a power of up to 1000 W, yielding a sample carrier temperature of over 900°C . High purity (6N) argon was used as sputter gas at a pressure of 2×10^{-3} mbar. The electron

3.2. X-Ray Diffraction and Reflectometry

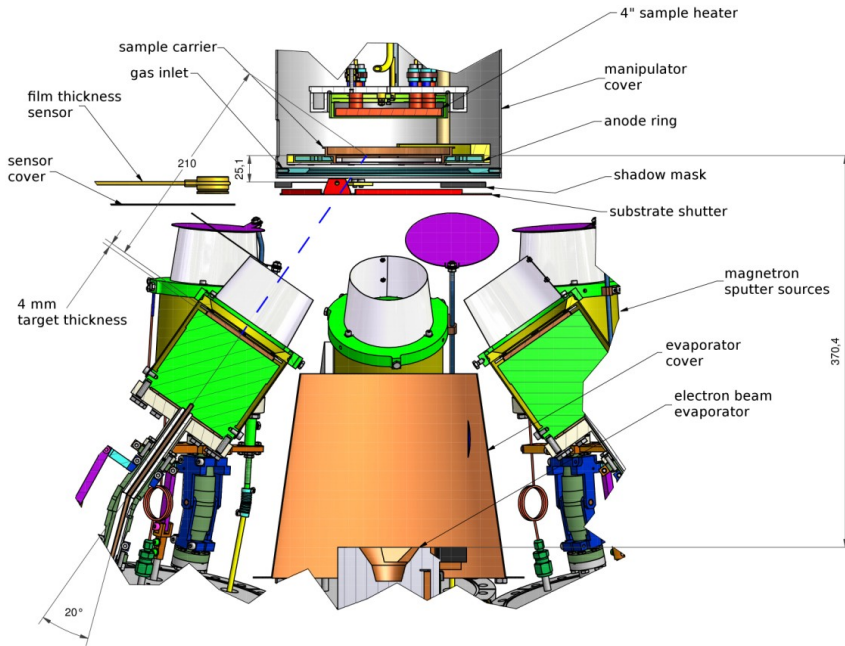


Figure 3.1: Schematic cross section of the BESTEC sputter system.[29] All sizes not specified are in mm.

beam evaporator was employed to deposit a protective MgO film on top of the sample, in order to protect the film below from oxidation. It was operated at a voltage of 6 kV and a beam current of 10 mA. The deposition process can be calibrated and monitored with a film thickness sensor.

3.2 X-Ray Diffraction and Reflectometry

For structural characterization, X-Ray Diffraction (XRD) and Reflectometry (XRR) measurements were conducted. A PHILLIPS X'PERT PRO MPD diffractometer equipped with Bragg-Brentano optics, collimator point focus optics and an open Euler cradle was used. It is operated with Cu K_{α} radiation ($\lambda = 1.5419 \text{ \AA}$). λ is the weighted average over the wavelengths of the $K_{\alpha 1}$ and

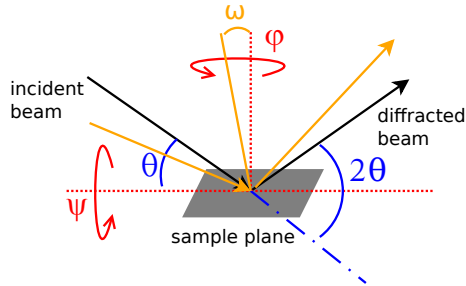


Figure 3.2: Sketch of the beam path and the relevant angles in the X-ray diffractometer. The Euler cradle allows rotating by the angle ϕ and tilting by the angle Ψ . The diffracted intensity is recorded against the scattering angle 2θ . Lattice planes that are not parallel to the sample plane can be measured by tilting the two goniometer arms by an angle ω .

$K_{\alpha 2}$ edges.[30] A heating stage, built during this work, is available for the Multi Purpose Sample stage. It consists of a resistor and a copper plate mounted to a ground plate allowing temperatures up to 100°C . There are two options used in this work to measure lattice planes which are not parallel to the sample plane. Firstly, an Euler cradle is available which allows rotating (ϕ) and tilting (Ψ) of the sample (shown in Figure 3.2). Secondly, two axis measurements $2\theta - \omega$ are possible. The latter option has the advantage of higher resolution. It can also be combined with the heating stage. At low 2θ values and large offsets ω this method has the disadvantage of decreasing intensity. If 2θ is kept constant and ω is varied, this is called a rocking curve. With this, lattice planes that are not parallel to the sample plane are measured.

High accuracy pole figure measurements with tilt angles up to $\Psi = 10^{\circ}$ were conducted using the Bragg-Brentano optics in combination with the Euler cradle. For pole figure measurements with Ψ larger than 10° , the collimator point focus optics was used instead of the Bragg-Brentano optics. X-Ray Reflectometry was employed to study roughness and the film thickness of the thin films.

3.3 Chemical composition analysis by X-Ray Fluorescence

To determine the chemical composition of the samples produced in the BESTEC, X-Ray Fluorescence (XRF) was used. For XRF measurements the XRD system gets equipped with an energy dispersive x-ray detection system. It consists of an Amptek XR-100CR Si-PIN detector and a digital pulse processor. The detector is in a box with Kapton windows under Helium atmosphere to allow detection of light elements. The sample is excited by the continuous bremsstrahlung from the Cu anode operated at 40kV. A 400 μ m Al foil is used to remove characteristic Cu radiation. The excitation spectrum is modeled with Ebels's model.[31] The fluorescence spectrum of the sample is post-processed to remove escape and sum peak, smoothed and the background is removed. Finally, a fundamental parameter analysis based on a non linear fitting algorithm is performed. The complete analysis is performed by the detector specific software.

3.4 Electric transport measurements

Electrical four point transport measurements in dependence on the sample temperature from 350 K down to about 20 K were performed in a cryostat. Magnetoresistance measurements were conducted using a variable permanent magnet (coaxial Halbach cylinder configuration, Magnetic Solutions Multimag) with a maximum field strength of 1 T in the cryostat. The magnetic field range 0 T \rightarrow -1 T \rightarrow 1 T \rightarrow -1 T is traversed in steps of 0.1 T for each temperature step. This equates to one full field loop with virgin curve.

For these measurements, the samples were prepared by standard photolithographic techniques. Further information about this topic can be found in e.g.[32].

3.5 Magnetic Measurements

Magnetic measurements were performed in a superconducting quantum interference device (QUANTUM DESIGN MPMS) in a temperature range between 10 and 330 K and a magnetic field range of 5 T. The magnetization of the samples was determined by measuring the size of the sample using a microscope. The thickness is known from XRR measurements.

4 Phase Field Simulations

Abstract

In this chapter phase field simulations of the martensitic transformation in thin films are discussed. The focus is on the understanding of the influence of the film thickness on the different energy terms and the degree of suppression of the transformation. A phase field model developed by Levitas *et al.* [33, 34] is employed. The simulations are carried out in the framework of the finite elements method which is not introduced in this thesis. Further reading about this topic can be found for example in [35].

The phase-field method is a computational approach to model and predict the evolution of morphological features and the microstructure in materials. All problems, that can be modeled by this approach, have in common that phases are separated by distinct interfaces. The description of a microstructure is achieved using conserved or non-conserved order parameters that are continuous across the interfacial regions. A typical example for a conserved problem is the spinodal decomposition.[36] This is a phase separation mechanism, where no new phases develop. Thus, conserved order parameters are required. A typical example of a non-conserved problem is a solid state phase transition with crystallographic orientations (variants).[33, 34] Here, the new phase requires additional order parameters for each variant. Hence, non-conserved order parameters have to be used. The temporal and spatial evolution of the order parameters is governed by the Cahn-Hilliard nonlinear diffusion equation[37] for conserved problems or the Allen-Cahn relaxation equation[38] (Ginzburg-Landau kinetic equations) for non-conserved ones. With the fundamental thermodynamic and kinetic information as input, the phase-field

method is able to predict the evolution of arbitrary morphologies and complex microstructures without explicitly tracking the positions of the interfaces. Important examples of material processes, described by the phase field approach, are solidification, solid-state structural phase transformations, grain growth and coarsening, domain evolution in thin films, pattern formation on surfaces, dislocation microstructures, crack propagation, and electromigration.[39, 40]

In this work the phase field approach is used to describe the evolution of the microstructure during the martensitic transformation; this is a non-conserved problem which is thus described by the Ginzburg - Landau kinetic equation.

$$\frac{\partial \eta_k}{\partial t} = L\beta_k \Delta \eta_k - L \frac{\partial G}{\partial \eta_k} + \xi_k, \quad (k = 1, 2, \dots, n) \quad (4.1)$$

where n is the number of variants, L is a kinetic coefficient, G the Gibbs free energy, η the order parameter, β a material parameter and ξ thermal noise. The driving force for the evolution of the microstructure is $L \frac{\partial G}{\partial \eta_k}$. The interface energy between the different phases is described by $L\beta_k \Delta \eta_k$. The approaches to model the martensitic transformation differ usually by the chosen development in the order parameters of the free energy G . Here, the phase field model proposed by Levitas *et al.* [33, 34] is chosen which has successfully described thermal and stress induced martensitic transformation. In the following section this model is introduced.

4.1 Phase field model

A multi-variant martensitic microstructure can consist of austenite and n martensitic variants. These are represented in terms of the distribution of n order parameters η_k with ($k = 1, 2, \dots, n$). The order parameters η_k vary from zero to one, where $\eta_k = 1$ corresponds to the k -th martensitic variant, $\eta_k = 0$ corresponds to austenite or other martensitic variants and $0 < \eta_k < 1$ represents transitional regions or interfaces. The evolution of the variants is described by the time dependent Ginzburg-Landau kinetic equation given by the kinetic Ginzburg Landau equation (see eq. 4.1). The specific Gibbs free

energy proposed by Levitas *et al.* [34] is given by:

$$G = -\sigma_{ij}C_{ijmn}^{-1}\sigma_{mn} - \sigma_{mn}\epsilon_{mn}^k[a\eta_k^2 + (4 - 2a)\eta_k^3 + (a - 3)\eta_k^3] \\ + \sum_{k=1}^n [A\eta_k^2 + (4\Delta G^\theta - 2A)\eta_k^3 + (A - 3\Delta G^\theta)\eta_k^4] + \sum_{i=1}^{n-1} \sum_{j=i+1}^n F_{ij}(\eta_i, \eta_j)$$

where C is the elasticity tensor. The transformation strain is given by:

$$\epsilon_{mn}^t = (\epsilon_{ti})_{mn}[a\eta_i^2 + (4 - 2a)\eta_i^3 + (a - 3)\eta_i^4] \\ + \sum_{i=1}^{n-1} \sum_{j=i+1}^n \eta_i^2 \eta_j^3 [3(\eta_i(\epsilon_{ti})_{mn} + \eta_j(\epsilon_{tj})_{mn} + (a - 3)(\eta_i(\epsilon_{tj})_{mn} + \eta_j(\epsilon_{ti})_{mn}))]$$

and the difference of the chemical free energy of austenite and martensite:

$$\Delta G^\theta = A_0(\theta - \theta_e)/3, \quad A = A_0(\theta - \theta_c)$$

where θ the temperature, θ_c the critical temperature where the austenite becomes unstable, and θ_e is the equilibrium temperature. A_0 is a material parameter. An additional term is needed for variant to variant transformation, which also removes the possibility that more than one η_k equals one simultaneously:

$$F_{ij}(\eta_i, \eta_j) = \eta_i \eta_j (1 - \eta_i - \eta_j) (B[(\eta_i - \eta_j)^2 - \eta_i - \eta_j] + D\eta_i \eta_j) + \eta_i^2 \eta_j^2 (\eta_i Z_{ij} + \eta_j Z_{ji}) \quad (4.2)$$

with

$$Z_{ij} = \bar{A} - A + \sigma_{mn}[(a - 3)(\epsilon_{tj})_{mn} + 3(\epsilon_{ti})_{mn}]$$

and a, B, D, \bar{A}, A are material parameters.

The stresses σ and strains (elastic ϵ^e , transformation ϵ^t) are calculated by standard equations of linear elasticity: the relation between strains ϵ_{ij} and displacements u_i

$$\epsilon_{ij} = 0.5(u_{i,j} + u_{j,i}) = \epsilon_{ij}^e + \epsilon_{ij}^t \quad (4.3)$$

Hooke's law

$$\sigma_{ij} = C_{ijmn}\epsilon_{mn}^e = C_{ijmn}(\epsilon_{mn} - \epsilon_{mn}^t) \quad (4.4)$$

and the equilibrium equation

$$\nabla \sigma = 0 \quad (4.5)$$

Given: Initial values for stresses σ^t and order parameters η_k^t at time t
 Find: Stresses $\sigma^{t+\Delta t}$ and order parameters $\eta_k^{t+\Delta t}$ at $t + \Delta t$.

1. Solve n Ginzburg-Landau kinetic equations 4.1 separately in order to calculate the order parameters $\eta_k^{t+\Delta t}$ at time $t + \Delta t$.
2. Evaluate the total transformation strain at $t + \Delta t$
3. Solve the elastic problem equations (4.3–4.5)
4. Update stresses at $t + \Delta t$

Figure 4.1: Summary of the finite element solution algorithm

4.2 Implementation

The phase field model of Levitas *et al.* [33, 34] is implemented using the framework of finite elements. The solution of the coupled time dependent system of equations (4.1,4.3–4.5) is achieved as proposed by J. Y. Cho[41]: to integrate the equations in time, the total observation time is subdivided into N time steps with small time increments Δt . Then, in order to find unknown parameters at the end of each time step, it is assumed that:

1. for the k -th equation 4.1, all order parameters η_k , ($k = 1, 2, \dots, n$) and stresses are fixed and known from the previous time step.
2. for the equations 4.3–4.5, all order parameters are fixed and known from the previous solution of n equations 4.1.

These assumptions correspond to an explicit time integration scheme and allow to decouple the equations at any small time step; i.e., any k -th equation of 4.1 and the system of equations 4.3–4.5 can be solved separately. For the solution at any time step, the finite element algorithms with implicit time integration for heat transfer problems (eq. 4.1) and elasticity problems (eq. 4.3–4.5) are used. The finite element algorithm for the solution is summarized in Figure 4.1.

4.3 Simulations of thin films - Geometry, approximations and solution

The focus of the phase field simulations is on the influence of the film thickness on the martensitic transformation. The thin films are approximated as a two dimensional cut in the out of plane direction of the film. The films are always five times as wide as the film thickness. This film thickness to film width ratio is optimized for reliable simulations results. The substrate is approximated as an elastic area three times as thick as the thin film. Eq. 4.1 is defined on the thin film domain. The system of equations 4.3–4.5 are defined on both domains.

The following boundary conditions are applied for eq. 4.1: On the boundaries the zero flux condition ($-\mathbf{n}(-c\nabla\eta_1) = 0$) and ($-\mathbf{n}(-c\nabla\eta_2) = 0$) is applied. On the left and right sides periodic boundary conditions are used.

The boundary conditions for the elastic problem (eq. 4.3–4.5) are: On the left and right side the boundaries are free with periodic boundary conditions. The bottom of the MgO is fixed. The top of the film is free. Continuity is assumed between the two domains .

The simulations are carried out with the finite element software package COMSOL MULTIPHYSICS 4.2A. An essential step of solving a problem with finite elements is meshing of the geometry. A dense mesh is necessary especially for detailed structures such as the microstructure of martensite. However, a higher mesh density also leads to more knot points on which the problems has to be solved. Hence the mesh is limited by the size of the main memory of the computer used. Thus, the mesh has to be chosen in such a way that it is fine enough at critical points in the geometry. A coarser mesh is applied elsewhere. The proposed geometry and the mesh used in this work are shown in Figure 4.2. The top region is the thin film showing the martensitic transformation. A triangular mesh with quadratic Lagrange elements is applied. The element to area ratio is 0.37 with a maximal element size of 0.2 nm. On the MgO substrate the element to area ratio is significantly smaller with 0.0087 with a maximal element size of 1.7 nm.

The finite element algorithm is implemented using segregated solvers to decouple the equations. An algebraic multigrid solver [42] is chosen for all equations. The coarse problem is then solved by the PARDISO[43] algorithm. As initial condition uniformly distributed random values of η_1 and η_2 in the range of $\eta_1, \eta_2 \in [0 - 0.1]$ are applied; this is the implementation of the thermal

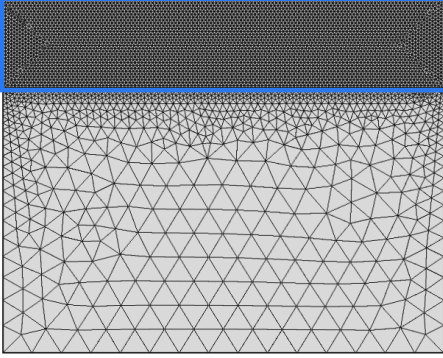


Figure 4.2: Typical meshing result for a geometry used in this work. The 5 nm thick film is marked in blue. The substrate is below.

noise ζ . All values except for θ_e and θ_c are adapted from Levitas *et al.* for the shape memory alloy NiAl.[34] For this alloy the potential landscape has been thoroughly tested and unphysical minima are unlikely. Thus, the results here mirror only trends that can also be expected for other alloys. The parameters used are: $a = 2.98$; $A = 5320$ MPa; $\theta_e = 300$ K; $\theta_c = 250$ K; $A_0 = 4.4$ MPa/K; $B = 0$; $D = 5000$ MPa; $\beta = 2.33 \times 10^{-11}$ N; $L = 2596.5$ m²/Ns; $E = 198.3$ GPa; $\nu = 0.33$; $\rho = 5850$ kg/m³.

$$\epsilon_{t1} = \begin{pmatrix} 0.215 & 0 & 0 \\ 0 & -0.078 & 0 \\ 0 & 0 & -0.078 \end{pmatrix}; \epsilon_{t2} = \begin{pmatrix} -0.078 & 0 & 0 \\ 0 & 0.215 & 0 \\ 0 & 0 & -0.078 \end{pmatrix}$$

The two variants chosen correspond to a-c twinning which has also been observed in the martensite phase of Ni-Mn-Sn (see also chapter 5.3).

Time dependence

The simulation results for a 5 nm thin film in dependence of time is shown in Figure 4.3. As temperature 149 K is chosen. At $t = 0$ the initial condition is shown. It develops quickly ($t = 6 \times 10^{-13}$ s) into a kind of tweed like structure often also observed in the premartensitic phase.[44] After $t = 2 \times 10^{-12}$ s the typical a-c twinning structure with an angle of 45° relative to the substrate becomes visible. The transformation is finished after 0.4 ns. The time dependence is similar to simulations in former publications.[45] In the following, all simulations will be carried out up to this time.

4. PHASE FIELD SIMULATIONS

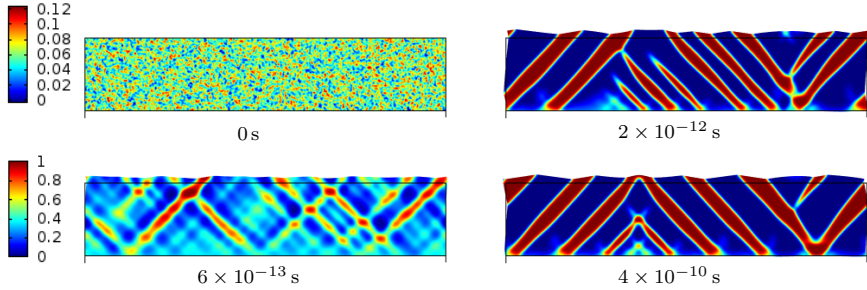


Figure 4.3: The time dependence of the microstructure is shown. After 0.4 ns the transformation is stationary. η_1 is plotted here. Only the thin film is shown.

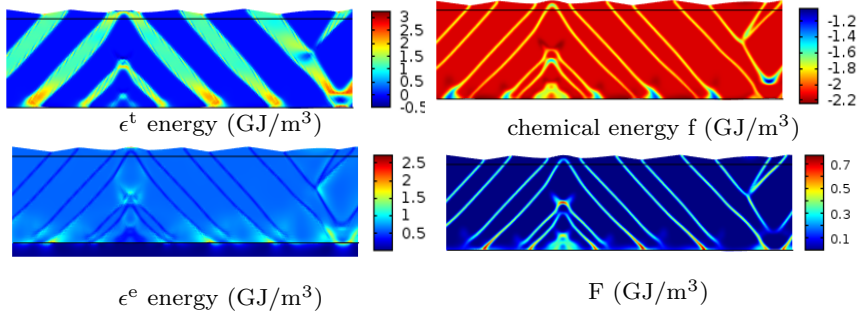


Figure 4.4: The energy contributions for the 5 nm thick film after completion of the transformation in the thin film area is presented. For clarity, only ϵ^t of η_1 is shown. ϵ^e is also presented on the relevant substrate region.

Energy terms

All energy terms of the Gibbs potential are shown for the 5 nm thick sample after the transformation is completed in Figure 4.4. The transformation strain energy shows the highest values close to the substrate due to a higher stress level. The highest elastic energy can also be observed in this area. The elastic energy in the MgO substrate reduces quickly after about 0.5 nm. The chemical energy depends directly on the degree of transformation. Hence, close to the

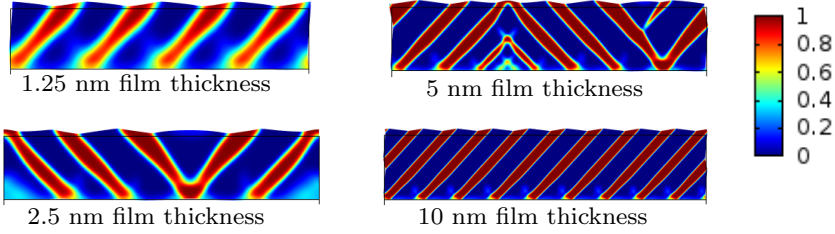


Figure 4.5: The thickness dependence of the microstructure is shown. η_1 is plotted here. Only the thin film is shown.

substrate the chemical energy is reduced. The F energy terms (see eq. 4.2) show contributions at the interfaces between the variants and especially close to the substrate, if a large transformation occurs. Furthermore, a crossing of the same variant leads to enhanced F energy. However, note that the F energy is an order of magnitude smaller than the other energy contributions.

Comparison to the crystallographic theory

The simulations are tested to known theoretical results. The fraction of martensitic variants can be calculated analytically in the framework of the crystallographic theory. The equation is given as:[8]

$$\lambda = \left(1 - \sqrt{1 + \frac{2(\alpha^2 - 1)(\beta^2 - 1)(\alpha^2 + \beta^2)}{(\beta^2 - \alpha^2)}} \right) \quad (4.6)$$

With the values of α and β used in the simulations the variant fraction is $\lambda = 0.305$. For the simulations λ is calculated by averaging η_1 over the thin film area. It is difficult to give exact values due to the diffuse interface. If the complete diffuse area is taken into account, λ is overestimated with $\lambda = 0.34$. However, if we consider only η_1 values larger than 0.5 the average results in $\lambda = 0.3$. Thus, we can conclude that the simulation results for a-c twinning is in reasonable agreement with the crystallographic theory.

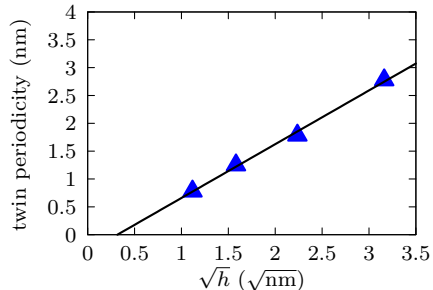


Figure 4.6: The twin periodicity in dependence of the square root of the film thickness is shown. A linear fit is applied.

Thickness dependence

The thickness dependence of the microstructure and the corresponding energy terms are investigated in the following. The simulations are carried out for films with thickness of 1.25 nm, 2.5 nm, 5 nm and 10 nm. The microstructure of the thin films is shown in Fig. 4.5. For all film thicknesses the typical a-c twinning structure is visible. However, the degree of the transformation is reduced close to the substrate as is best visible for the 1.25 nm thick film.

The microstructural dependence on the film thickness can be tested to known experimental results. Diestel *et al.* [46] showed that the twinning periodicity Λ of Ni-Mn-Ga in dependence of the film thickness can be described by the following scaling law:

$$\Lambda = \sqrt{\frac{\gamma}{E\epsilon^2}} D \quad (4.7)$$

where γ is the twin boundary energy, D is the size of the martensitic lamella which corresponds here to the film thickness, ϵ the transformation strain, and E the Young Modulus. The dependency is a special case of the universal Landau-Lifshitz-Kittel scaling law, originally developed for magnetic domains. [47, 48] The twinning periodicity of the simulations is plotted against the square root of the film thickness as shown in Figure 4.6. The results fit very well to the expected linear relationship as is proven by the linear fit.

The transformation in dependence of temperature is investigated in the following. Random initial conditions as above are applied. The first stable martensitic structure is observed at 254 K. The following temperature steps are calculated using the result of the previous temperature step as initial condition.

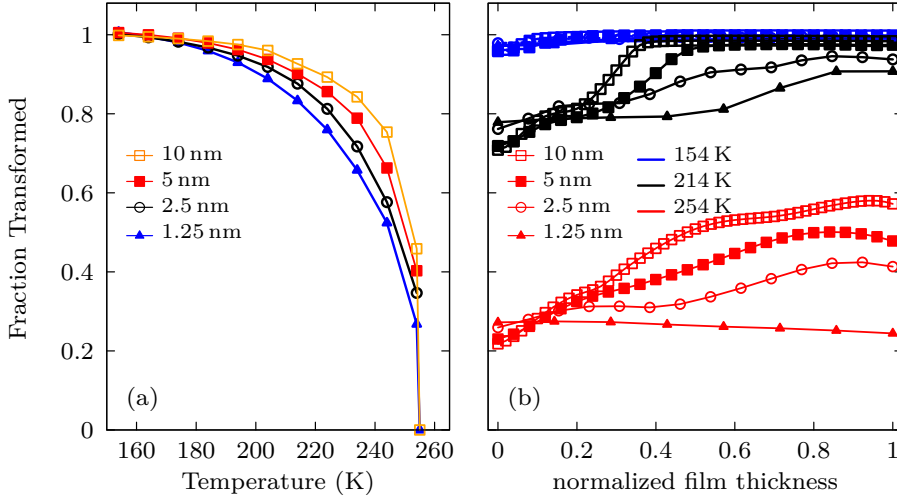


Figure 4.7: In (a) the temperature dependence of the transformation degree is shown. The average of the transformation degree along the horizontal for selected temperatures for different film thicknesses is shown in (b).

The calculations are carried out up to 154 K where the transformation for all films is finished. The degree of the transformation is determined using the order parameters η_1 and η_2 . The average value of $\eta_1 + \eta_2$ over the film area equals one, if the transformation is complete in the whole area. An average value of zero corresponds to the austenite phase. The degree of the transformation is plotted in Figure 4.7 (a). The transformations starts for all films at 254 K and finishes at 154 K. Between these temperatures the transformation behavior differs: with decreasing film thickness the transformation rate decreases. Thus, to achieve the same degree of transformation, a higher degree of undercooling is required.

The transformation degree in dependence of the height above the substrate is calculated in the following to gain insight into the influence of the rigid substrate. For this, $\eta_1 + \eta_2$ is averaged along the horizontal. The result is shown in Figure 4.7 (b). At high temperatures the transformation is suppressed close to the substrate. For the 10 nm film the transformation degree decreases quickly

4. PHASE FIELD SIMULATIONS

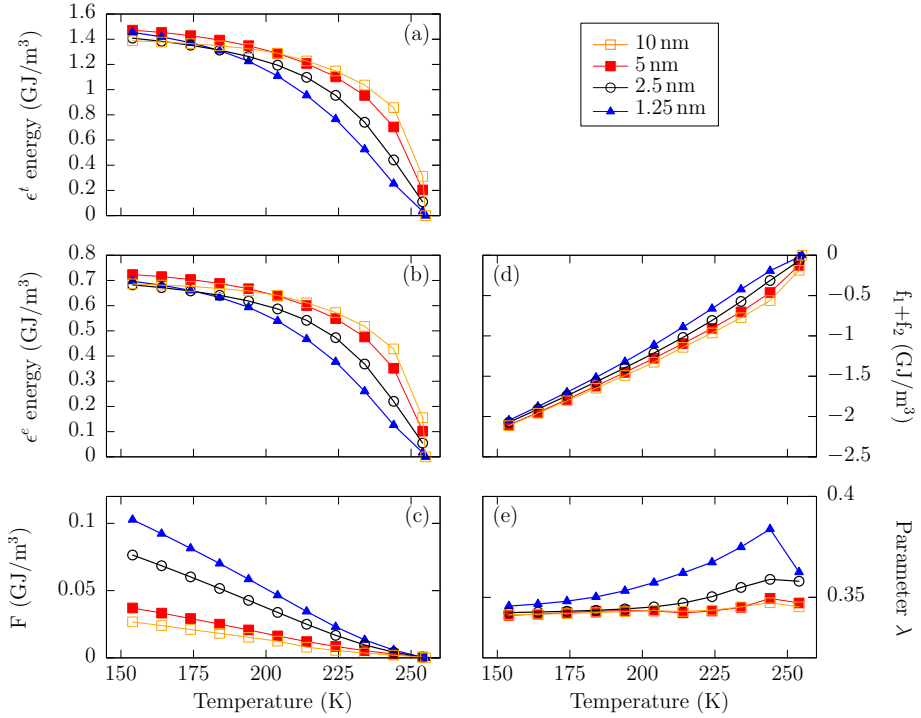


Figure 4.8: The temperature dependence of energetic contributions and parameters for different film thicknesses is shown. In (a) the transformation strain energy, in (b) the elastic strain energy, in (c) the F energy term, in (d) the chemical energy and in (e) the variant fraction is shown.

at around 5 nm above the substrate. This tendency is mirrored in the thinner films. With decreasing temperature the transformation progresses in the whole thin film area. At 214 K the transformation is finished in a large area of the 10 nm film. At around 3 nm above the substrate, its influence becomes clearly visible. At 154 K the transformation is complete and virtually no influence of the substrate is visible for all films. Thus we can understand the different transformation behaviors in terms of the importance of the rigid substrate. The thinner the film, the larger the influence on the transformation. The thicker

films show a combination of both regimes. At first, the transformation far above the substrate completes. If the temperature difference is large enough, the rest of the transformation finishes.

The influence of the film thickness on the most important energy terms and parameters is discussed in the following. In Figure 4.8 the temperature dependence of these parameters is shown. The transformation- and elastic strain energy mirror the transformation behavior. At 154 K, where the transformation is finished for all films, no clear relation between film thickness and transformation- or elastic strain energy can be seen. F , which is a function of the number of twin boundaries, clearly increases with decreasing film thickness. This corresponds well to the universal Landau-Lifshitz-Kittel scaling law. The chemical energy f and F show in the low temperature region a linear dependence on the temperature. This behavior is according to the model. The variant fraction λ is at first closer to equality ($\lambda = 0.5$) and decreases with decreasing temperature to 0.34 for all thin films. This behavior is most pronounced for the 1.25 nm thick film. In this film the transformation is most suppressed. Hence, for a low transformation degree in very thin films, a λ value close to equality seems to be energetically favorable. For the finished transformation, λ is close to the value predicted by the crystallographic theory. This corresponds to the result in the former subsection.

4.4 Summary and Discussion

The phase field model of Levitas *et al.* [33, 34] has been successfully used to model the martensitic transformation in thin films. The simulation results are in good agreement with the crystallographic theory and experimental results for the twinning periodicity. The analysis of the thickness dependence show that a suppression of the transformation close to the substrate is present. Large undercooling is required to overcome this energy barrier. The suppression of the transformation becomes more pronounced for thinner films leading to a more shallow transformation progression.

The simulations were carried out for material parameters of NiAl. Thus, the exact details of the thickness dependence are expected to be different for Ni-Mn-Sn. Furthermore, a linear increase of the chemical energy is assumed in this model. This is only the case close to equilibrium of the chemical energies. Thus, while it is possible to overcome the suppression due to the large amount

4. PHASE FIELD SIMULATIONS

of chemical energy, this might not be the case in real materials. However, the observed trends should be transferable to the thin films discussed in the following chapter.

5 Ni-Mn-Sn in thin films

Abstract

In this chapter the experimental results of the thickness dependence of Ni-Mn-Sn films are discussed. At first, the structural characteristics of the films in the austenitic state is investigated. The structural quality of the thin films can have a large impact on the transition and therefore is of great importance. In the following, the martensitic structure and the austenite-martensite transition are investigated using x-ray diffraction. The magnetic properties and the electric transport properties are discussed in detail. The influence of the film thickness on the transformation behavior is analyzed using the electric transport measurements. At last, the magnetoresistance of the thin films is discussed.

5.1 Introduction

Ni_2MnSn belongs to the class of Heusler compounds (X_2YZ). [15] By definition, they crystallize in the $L2_1$ structure as shown in Figure 5.1. It is a face centered cubic structure (space group $Fm\bar{3}m$) with a four atom basis. [49] The coordinates of these four basis sites A, B, C, and D, are given by $A = (0, 0, 0)$, $B = (\frac{1}{2}, \frac{1}{2}, \frac{1}{2})$, $C = (\frac{1}{4}, \frac{1}{4}, \frac{1}{4})$, $D = (\frac{3}{4}, \frac{3}{4}, \frac{3}{4})$. The structure has inversion symmetry, making two sites (C and D) equivalent. These are occupied by the X element. In the Wyckoff notation, the C and D sites are named 8c, and the other two sites are denoted as 4a for the Z element and 4b for Y. [49] The structure deviates from the ideal Heusler structure for off-stoichiometric Ni_2MnSn with a different Mn to Sn ratio. This due to inherent disorder between Mn and Sn on the 4a site. A Heusler alloy with complete disorder on the 4a and 4b sites has the B2 structure

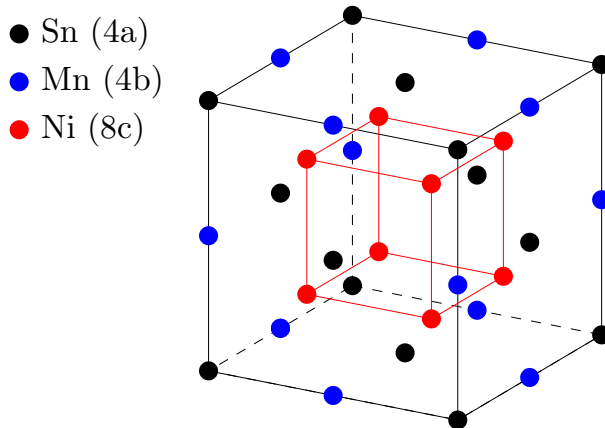


Figure 5.1: The crystal structure of the Heusler alloy Ni_2MnSn . In parentheses the Wyckoff positions are listed.

(space group $\text{Pm}\bar{3}\text{m}$). Thus for the off-stoichiometric Heusler compounds a mixture of L2_1 and B2 order is expected.

Certain off-stoichiometric compositions of Ni_2MnSn are ferromagnetic shape memory alloys.[15] The basic properties of a ferromagnetic shape memory alloy are the martensitic transition temperature M_s , the Curie temperature of the austenite T_c^A and of the martensite phase T_c^M . A summary of this data is presented for $\text{Ni}_{50}\text{Mn}_{50-x}\text{Sn}_x$ in the phase diagram shown in Figure 5.2.[50] M_s depends linearly on the valence electron per atom (e/a) value, which is adjusted by the Mn to Sn ration. T_c^A is around 320 K and decreases weakly with increasing (e/a) value. The e/a value has a large influence on T_c^M : With increasing e/a value T_c^M decreases linearly from around 240 K at $e/a= 8.1$ to 137 K at $e/a= 8.185$. The structure of the martensite phase is also determined by the e/a value. In the phase diagram the different possible phases 10M , 14M and L1_0 are indicated by different shades of blue. An introduction into the different martensitic structures is given in section 5.3

In order to investigate the influence of the film thickness on all important quantities, two sample series with different composition are produced; these are marked in Figure 5.2 with red dotted lines. Note that these are

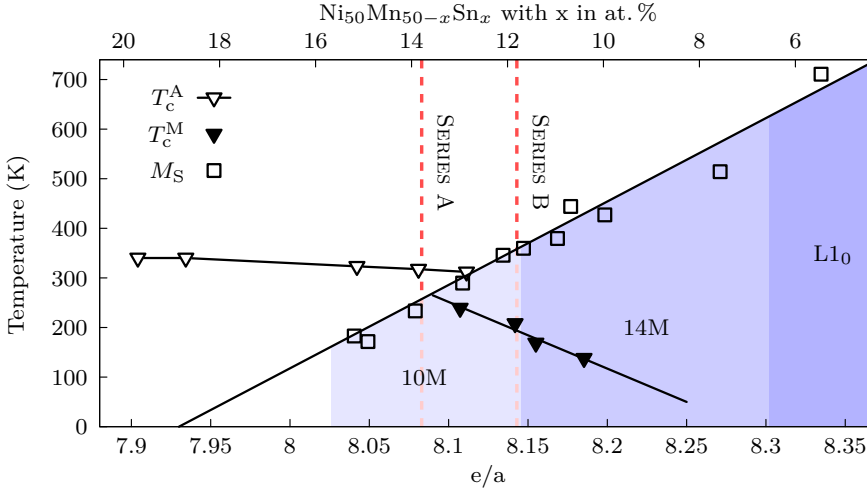


Figure 5.2: The magnetic and structural phase diagram of Ni–Mn–Sn. The triangles and the squares correspond to the magnetic and martensitic transition temperatures, respectively. The regions corresponding to different martensitic structures are colored in different shades of blue. The data is adapted from Planes *et al.* [50].

the expected bulk values. The first sample series (SERIES A) has a composition of $\text{Ni}_{51.6}\text{Mn}_{32.9}\text{Sn}_{15.5}$ which corresponds to $e/a = 8.083$. Thus, this series is ferromagnetic at room temperature and shows the martensitic transition around 260 K. The second sample series (SERIES B) has a composition of $\text{Ni}_{51.6}\text{Mn}_{34.9}\text{Sn}_{13.5}$ corresponding to $e/a = 8.143$. The martensitic transformation is around 360 K. Thus, the sample SERIES B is in the martensitic phase at room temperature. This allows to investigate the structure of the martensitic phase at room temperature using the XRD system equipped with the Euler cradle. It is also possible to investigate the structural transition at elevated temperatures using the XRD system with the heating stage. Furthermore, in this sample series T_c^M becomes visible. Hence, with these two sample series it is possible to investigate the thickness dependence of T_c^A , T_c^M and M_s .

The Ni–Mn–Sn films investigated in this work were grown on MgO(001) substrates using an ultra high vacuum (UHV) sputtering system as described

5. NI-MN-SN IN THIN FILMS

in section 3.1. The thin films were deposited from elemental Ni, Mn and Sn targets with a purity of 4N. During deposition, the substrate was heated to a temperature of 600°C and rotated at 10 rpm. The deposition temperature is optimized to maximal sample quality without Mn evaporation, which starts at around 650°C. The sputtering pressure was set to 2.3×10^{-3} mbar. The deposition rate was 0.32 nm/s. The films are capped by a 2 nm MgO layer deposited by e-beam evaporation.

For SERIES A films with 20 nm, 35 nm, 50 nm, 75 nm, 100 nm and 200 nm thickness have been fabricated. A slightly different selection of film thicknesses has been prepared for SERIES B: 10 nm, 20 nm, 35 nm, 50 nm and 100 nm.

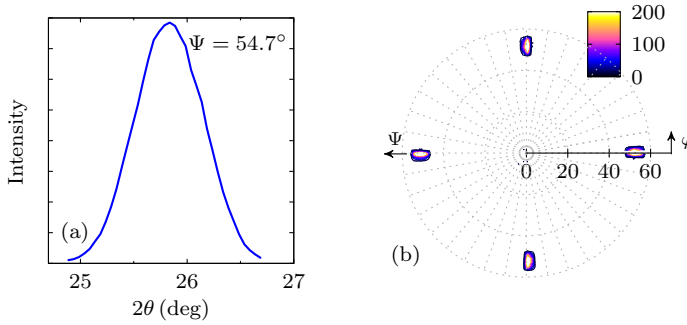


Figure 5.3: The (111) peak of a 50 nm thick film of SERIES A and the corresponding polefigure is shown in (a) and (b), respectively.

5.2 Structure in the austenite phase: thin film quality

The thin film structure and its quality are analyzed in this section. For this, XRD is a powerful method. It can be used to measure properties like the thin film growth on the substrate (epitaxial, textured or polycrystalline), the chemical order, the grain size, grain orientation and microstrain.[51] For the analysis, the samples have to be investigated in the austenite phase.

Experimental results

The films grow epitaxially with the in-plane relation $\text{MgO [100]} \parallel \text{Ni-Mn-Sn [110]}$. This is shown by the four fold symmetry of the (111) peak polefigure for a 50 nm sample of SERIES A (see Figure 5.3). The sample is oriented such that $\varphi = 0$ corresponds to MgO [100] . The presence of the (111) peak shows partial $L2_1$ order of the films.[52]

The detailed thickness dependence of the austenitic structure of both sample series is presented in Figure 5.4. SERIES A is in the austenitic state at room temperature (RT) and is therefore characterized at RT. SERIES B is in the martensitic state at RT. Hence, this series is measured at 374 K well above the transition temperature to get austenite. Figure 5.4 (a) shows the XRD scans for the films of SERIES A in the thickness range of 20 nm to 200 nm. The XRD results of SERIES B at high temperature are very similar and not shown here.

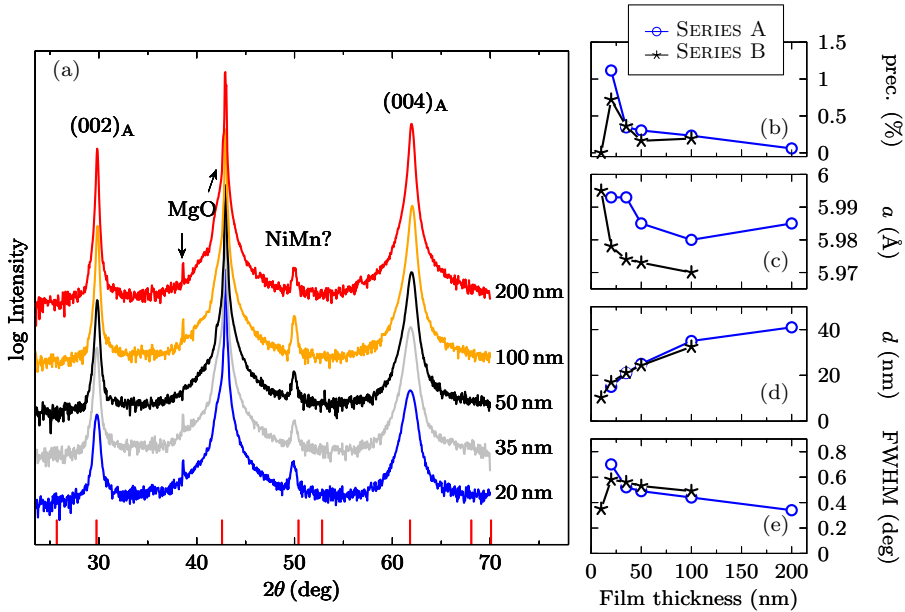


Figure 5.4: The XRD measurements of SERIES A at room temperature are shown in (a). The red bars mark all possible reflections of the cubic L₂₁ phase of Ni-Mn-Sn. In (b) the NiMn precipitate fraction, in (c) the lattice constant, in (d) the out of plane grain size d , and in (e) the Full width at half maximum of the rocking curve is shown in dependence of the film thickness.

All films show very intense (002) and (004) peaks of the cubic phase. No other peaks of the cubic phase are visible indicating a highly textured growth in [001] direction. At 49.7°, an additional peak is visible which cannot be indexed accordingly. The intensity of this peak is very low and not correlated to the film thickness. A possible explanation is a NiMn precipitate due to grain boundary segregation.[53] The precipitate fraction is shown in Figure 5.4 (b); it is approximated as the ratio of the total intensity of the (004)_A and the precipitate peak. The precipitate fraction increases to lower film thicknesses, indicating segregation at interfaces. The 10 nm film of SERIES B shows no segregation, possibly because of less grain boundaries.

Lattice constants

The out-of-plane lattice constants at room temperature (RT) are analyzed in the following. They are determined from the XRD spectra using the Bragg equation.[51] To get comparable results, the RT lattice constants of SERIES B are required. These are determined in the following way: The XRD measurements at 374 K give the lattice constants at this temperature. The coefficient of linear thermal expansion α is known from a linear fit to the lattice constant's temperature dependence of the 100 nm thick film of SERIES B (see section 5.3) With α , the lattice constant at RT is extrapolated. The result, the RT out-of-plane lattice constants of both series, is shown in Figure 5.4 (c).

The lattice constant of SERIES A is 5.993 Å for the 20 nm and 35 nm thick films. The 10 nm thick film of SERIES B has a lattice constant of 5.995 Å. For thicker films, both series show a drop of the lattice constants to 5.985 Å for SERIES A and 5.97 Å for SERIES B. This drop can be attributed to a compression of the lattice: The lattice constant of MgO (5.957 Å)¹ is smaller than the Ni-Mn-Sn lattice constant. The in-plane lattice constant of the thin film has to be compressed to fit to the substrate. This compression leads to an expansion of the out-of-plane lattice. The compression is quickly relaxed by dislocations[54] leading to the cubic bulk lattice constant. The lattice constants of SERIES B fit better to the MgO substrate than SERIES A's. This is also visible in the lower degree of expansion visible for example at the two 20 nm thick films.

The lattice constants of the thicker films are close to the values found in bulk samples. Krenke *et al.* [15] found 5.995 Å for Ni₅₀Mn₃₅Sn₁₅. This is comparable to 5.985 Å of SERIES A (Ni_{51.6}Mn_{32.9}Sn_{15.5}). The small deviation could be explained by the higher Ni content since Ni has a smaller atomic radius compared to Mn. There is no literature data available for the bulk lattice constant of SERIES B (Ni_{51.6}Mn_{34.9}Sn_{13.5}). However, when examining a similar difference in composition (Ni₅₀Mn₃₂Sn₁₈ and Ni₅₀Mn₃₀Sn₂₀) Krenke *et al.* [15] found that the lattice constants of these two compositions differ by 0.015 Å. This difference is similar to the difference observed between SERIES A and SERIES B.

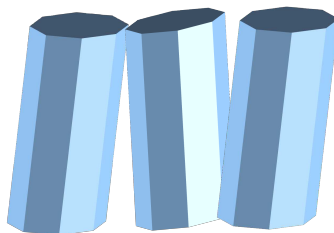


Figure 5.5: Sketch of a columnar structure with some grain misorientation.

Grain size and microstrain

A further analysis of the peak shape and broadening can give information about microstrain and the out-of-plane grain size of the films. Both effects, a decreasing grain size and an increasing micro strain, lead to peak broadening. For the analysis, either a Williamson-Hall analysis or a Rietveld refinement are possible methods.[51] However, all methods fail to give reliable results if the peak broadening is on the same scale as the instrumental broadening. This is the case for the films above 50 nm thickness. Here the peak broadening is 0.21° and the instrumental broadening 0.18° . Nevertheless, a qualitative analysis is possible for all films. While peak broadening due to grain size effects is independent of the diffraction angle, this is not the case for microstrain. With an increasing diffraction angle, the influence of microstrain on the peak broadening increases.[51] For all thin films the contribution due to microstrain is clearly visible in the different peak broadening of the (002) and (004) peaks. Since the microstrain contribution is the lowest for the (002) peak, the Debye-Scherrer formula[30] is used here to gain information about the lower limit of the grain size for SERIES A and SERIES B.

The grain size of both sample series is shown in Figure 5.4 (d). The 10 nm film of SERIES B shows a grain size of 10 nm indicating a columnar growth (shown in Figure 5.5) and a very low degree of microstrain. With increasing film thickness, the grain size of both sample series increase up to a maximum of about 40 nm for the 200 nm thick film. This grain size corresponds to the value of instrumental broadening. Thus, a larger grain size can be expected.

¹ $4.212 \times \sqrt{2} = 5.957 \text{ \AA}$. The factor $\sqrt{2}$ is due to the growth relation: MgO [100] || Ni-Mn-Sn [110]

The grain size of both sample series is comparable for all film thicknesses. A columnar growth is very likely for all film thicknesses. A sketch of a columnar structure is shown in Figure 5.5.

An analysis of the 20 nm film of SERIES A, using the Rietveld program MAUD, results in a grain size of 20 nm and a microstrain of 0.5%. The size of the microstrain is comparable to other Heusler thin films like Co₂VAl grown on MgO.[55]

Grain orientation (Mosaicity)

The grain misorientation of the thin films, sketched in Figure 5.5, is determined by rocking curves of the (004) diffraction spot (ω -curves, see section 3.2). A wider rocking curve implies a higher degree of grain misorientation. The full width at half maximum (FWHM) of the rocking curves is presented in Figure 5.4 (e). The following trends can be observed: For SERIES A, the FWHM increases with decreasing film thickness. The FWHM of the 20 nm thick film is 50% wider than the one of the 200 nm thick film. The rocking curve FWHM of SERIES B show a comparable trend for films thicker than 20 nm. The FWHM of the 20 nm thick film is smaller than the 20 nm thick sample of SERIES A. The 10 nm thick film shows a large decrease of the FWHM from 0.58° for the 20 nm thick film down to 0.35°.

The observed trends can be understood as follows: Misfit dislocations and local relaxation of thin films lead to a larger degree of grain misorientation.[56] The generation of misfit dislocations depends on the film thickness.[54] It can be separated into three different thickness regimes. In the first regime, the film thickness is so low that the compressed film does not relax. Here, the energy of a misfit dislocation is higher than the strain energy of the film. In the second regime, the film thickness exceeds a critical film thickness. In this case, the strain energy is higher than the misfit dislocation energy. Hence, misfit dislocations are formed and the film relaxes. In the third regime, the film grows further without additional misfit dislocation. The film is fully relaxed in this regime. Thus, the 10 nm film of SERIES B is most likely in the first regime. Dislocations are not formed, and the grain misorientation is low. With increasing thickness, the second regime is reached. This is the case for the 20 nm thin films. Here, the highest degree of grain misorientation is found. The difference in the grain misorientation of the 20 nm thick films

can be understood with the lower misfit of SERIES B. The strain is lower, and hence less dislocations are present. With further increasing film thickness the third regime is reached and the influence of the lattice relaxation close to the substrate/thin film interface is reduced. This leads to a smaller average grain misorientation. The same trend has also been observed for AlN films grown on Pt.[57]

Summary

The results on the structure and sample quality are as follows:

- the thin films of both sample series grow epitaxially on MgO.
- partial $L2_1$ order is present
- a small amount of precipitate (NiMn?) is visible. The precipitate fraction increases with decreasing film thickness.
- columnar growth is likely for all films
- a small compression of the lattice is visible leading to:
 - a tetragonal distortion of the lattice close to the substrate
 - a higher dislocation density with decreasing film thickness
 - a higher degree of grain misorientation with decreasing film thickness
- the 10 nm sample of SERIES B is an exception: It shows no precipitate and a very low rocking curve FWHM.

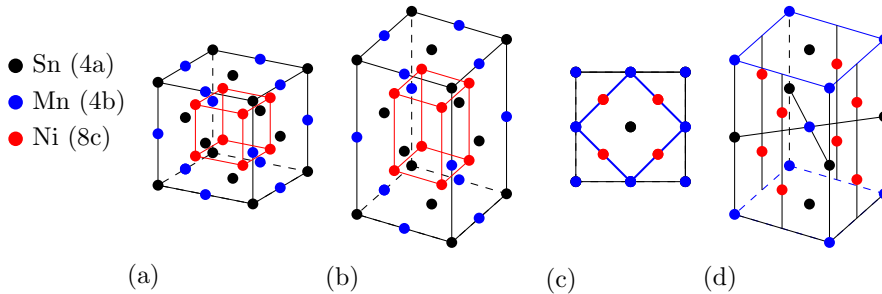


Figure 5.6: The $L2_1$ structure of Ni-Mn-Sn is shown in (a). A shear leads to a tetragonal distorted structure as shown in (b). The relation of the tetragonal unit cell to the $L2_1$ structure is shown in (c). The lattice of the $D0_{22}$ structure is presented in (d).

5.3 Martensitic structure

In the beginning of this section an introduction to the description of martensitic structures is given. In the second part the martensitic structure of the Ni-Mn-Sn thin films is analyzed.

The Basics

Generally, the martensitic structures can be divided into the class of non-modulated and modulated (layered) structures. The non-modulated martensite can be described by a shear of the lattice. Modulated structures involve not only a shear of the lattice but also a displacement of atomic layers along certain crystallographic directions.

One example for a non modulated structure also observed in Ni-Mn-Sn is the transformation from the austenite $L2_1/B2$ phase to the tetragonal distorted $D0_{22}/L1_0$ phase. The cubic to tetragonal transformation is depicted in Figure 5.6. In (a) the $L2_1$ structure is shown. The shear in one direction leads to a tetragonal structure (b). The crystallographic relationship between the $L2_1$ and the $D0_{22}$ crystal structure is shown in Figure 5.6 (c). In (d) the unit cell of the $D0_{22}$ phase is shown.

The modulated structures are more difficult to describe. The determination of the atom positions via XRD or other scattering methods is also more challenging. In the literature there are two main ways to model the atomic positions:

- periodic shuffling
- periodic stacking

The periodic shuffling is described by functions using harmonic terms. The displacement Δ_j of the j plane from its regular position is given by:

$$\Delta_j = A \sin(2\pi j/L) + B \sin(4\pi j/L) + C \sin(6\pi j/L) \quad (5.1)$$

where L is the modulation period. A , B and C are constants which are fitted to experimental reflection data.

The construction of a layered structure by periodic stacking is achieved using closed packed planes. These planes are also called *basal planes*. They are derived from 110 type austenite planes. The unit cell can be, e.g., monoclinic (M) or orthorhombic (O). The description of the layered structure can be done according to Zhdanov[58] or Otsuka[59]. The Zhdanov notation describes the stacking sequence explicitly. The Otsuka notation denotes the symmetry of the unit cell of the modulated structure and the number of shifted basal planes. In Figure 5.7 (a) the (001) projection of the Ni-Mn-Sn structure is shown. The relation of the unit cell of the cubic phase and the modulated phase is depicted for the example of the 4O structure. In (b) the (110) type austenite planes are sketched. Typical examples for structures described by the periodic stacking are shown in (c)-(e). In (c) the 14M structure is sketched. This is a monoclinic (M) structure with 14 shifted basal planes. In the Zhdanov notation this structure is $(5\bar{2})_2$. The 10M structure with 10 shifted basal planes, Zhdanov notation: $(3\bar{2})_2$, is shown in (d). The 4O structure, Zhdanov notation: $(2\bar{2})$, is presented in (e).

The difference between the two approaches, periodic shuffling or stacking, is visualized for the 14 layered structure in a HRTEM simulation done by Pons *et al.* [60] for Ni-Mn-Ga. The simulation with periodic stacking (14M) is shown in Figure 5.8 (a). The $(5\bar{2})_2$ sequence marked by the colored bars is clearly visible. The shuffling approach as shown in Figure 5.8 (b) leads to a more wavy like structure. The displacement waves form a pseudo $(4\bar{3})_2$

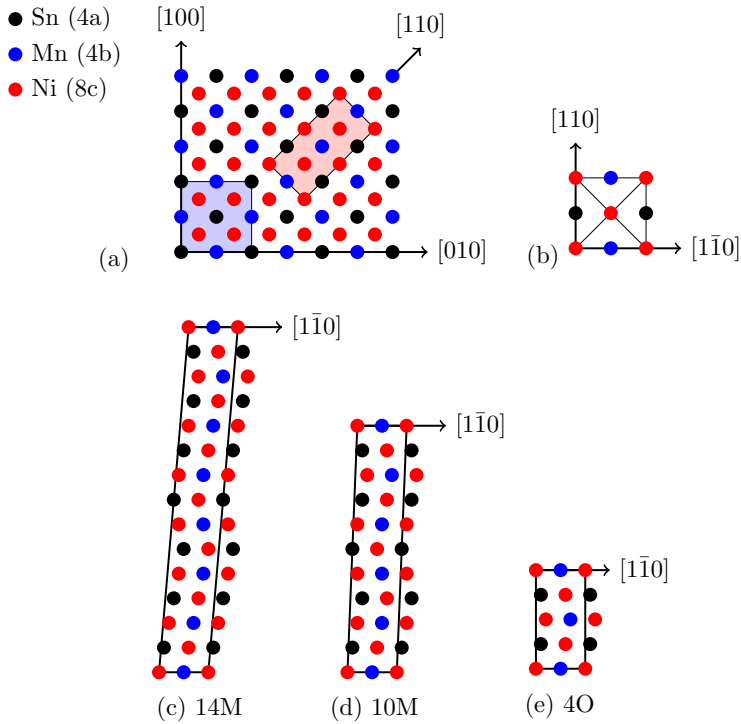


Figure 5.7: In (a) the projection of the $L2_1$ structure on the (001) plane is shown. The unit cell of the $L2_1$ structure is marked in blue. The 4O unit cell is shown by the red marked area. Shuffling along the $[1\bar{1}0]$ direction of the structure shown in (b) leads to the modulated structure presented in (c) - (e).

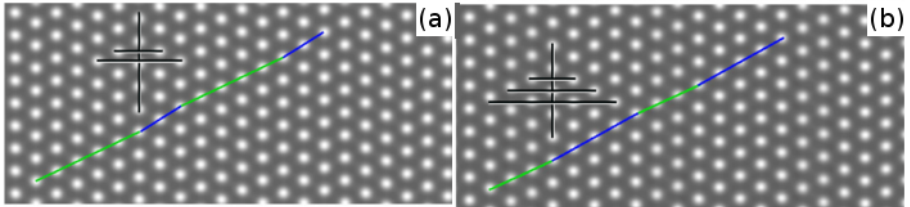


Figure 5.8: HRTEM simulation of Ni-Mn-Ga. In (a) the periodic stacking mechanism is assumed. The atom positions resulting from the periodic shuffling approach are shown in (b). The blue and green lines indicate the stacking sequence. The black lines show the necessary atom positions for nanotwinning. The different atom positions are best seen, when the image is viewed along the colored lines. Taken from [60].

structure. An important aspect that applies to modulated structures becomes visible here: The planes of the $(5\bar{2})_2$ structure separating the blocks of five and two planes are twin planes. This fact is visualized by the additional reference lines. However, this is not the case for the shuffled structure. If a modulated structure consists of nanotwins such as the 14M structure here, the structure is then called adaptive martensite.[61]

For the 14 layered structure, Pons *et al.* [60] showed that the 14M description is the best fitting for Ni-Mn-Ga. For the 10M structure of Ni-Mn-Ga, both descriptions lead to similar atom positions such that no differentiation between the two was possible.

In this work, the notation of Otsuka *et al.* [59] is used, since in previous works[60, 15, 62] a good agreement with this description has been found. The bulk martensite phase of Ni-Mn-Sn has been investigated in former studies. Krenke *et al.* [15] showed that with decreasing valence electron concentration e/a either $L1_0$, 14M or 10M phase can be observed. 4O, 6M, and 10M structures were measured in works of Sutou *et al.* [62] for $Ni_{50}Mn_{37}Sn_{13}$. The unit cell in the martensitic phase is either monoclinic, orthorhombic or tetragonal.

Experimental Results

The martensitic structure of SERIES B is investigated by XRD measurements. The XRD patterns measured at different tilt angles relative to the substrate

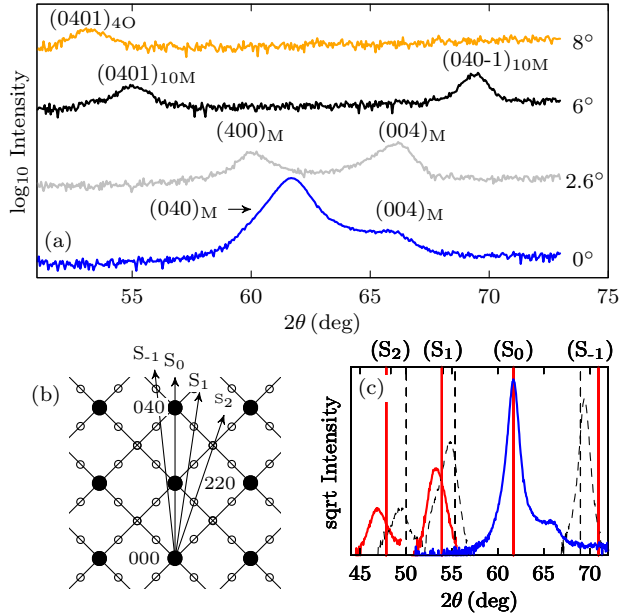


Figure 5.9: (a) The XRD patterns of the 100 nm thick film of SERIES B at different tilt angles. The reciprocal space map for a commensurate 4O phase is shown in (b). The arrows marked by S_{-1} to S_2 show schematically the 2θ scans. In (c) the superlattice peaks of the 4O/10M phase and the expected commensurate positions are presented by red solid lines/black dashed lines, respectively.

normal are shown in Figure 5.9 (a). The substrate is oriented such that the [100] direction of the Ni-Mn-Sn film in the austenite phase is parallel to the beam. At 0° and 2.6° the $(400)_M$, $(040)_M$ and $(004)_M$ peaks of the orthorhombic martensite phase are visible. The lattice constants are $a_{\text{orth}} = 6.156 \text{ \AA}$, $b_{\text{orth}} = 6.005 \text{ \AA}$ and $c_{\text{orth}} = 5.644 \text{ \AA}$. Lattice constants of all phases are described with reference to the cubic $L2_1$ unit cell. The $(040)_M$ peak shows a shoulder on the right hand side, which is due to a broad distribution of the crystallite orientation belonging to the $(004)_M$ peak. At higher tilt angles additional peaks appear. As we will show below, the additional peaks are probably due to the formation of 4O and 10M superstructures.

Table 5.1: The superstructures and the lattice constants of the orthorhombic phase of the 100 nm thin film of SERIES B is given together with bulk literature data.

Composition	e/a	Superstructures	$a_{\text{orth}}(\text{\AA})$	$b_{\text{orth}}(\text{\AA})$	$c_{\text{orth}}(\text{\AA})$
Ni _{51.6} Mn _{34.9} Sn _{13.5}	8.143	4O, 10M	6.156	6.005	5.644
Ni ₅₀ Mn ₃₆ Sn ₁₄ [63]	8.08	4O	6.16	6.07	5.6
Ni ₅₀ Mn ₃₇ Sn ₁₃ [62]	8.11	4O, 6M, 10M	6.08	5.95	5.77
Ni ₅₀ Mn ₃₇ Sn ₁₃ [15]	8.11	10M	6.1	6.07	5.61
Ni ₅₀ Mn ₄₀ Sn ₁₀ [15]	8.2	14M	6.128	6.05	5.57

The expected reciprocal space map for a commensurate² 4O superstructure is presented in Figure 5.9 (b). Generally, such a diffraction pattern consists of two distinct sets of reflections. The first group are intense peaks of the conventional unit cell with reciprocal vectors \mathbf{a}^* , \mathbf{b}^* and \mathbf{c}^* . The second group are satellite reflections which need an additional vector for indexing. This additional vector is called modulation vector \mathbf{q} and is usually given as:

$$\mathbf{q} = \alpha\mathbf{a}^* + \beta\mathbf{b}^* + \gamma\mathbf{c}^* \quad (5.2)$$

where α , β and $\gamma \in [0, 1]$. For the 4O superstructure, three additional diffraction peaks appear in the $\langle 110 \rangle$ directions. The arrows marked by S_{-1} to S_2 show 2θ scans at different tilts. The expected positions for these kind of 2θ scans of commensurate 4O and 10M superstructure peaks are marked by red solid lines and black dashed lines, respectively, in Figure 5.9 (c). All peaks in the vicinity of the $(040)_M$ peak that are measurable in the Bragg-Brentano geometry are shown. The peak positions do not fit exactly to the expected position of a commensurate superstructure. Thus the superstructure is incommensurate (IC). The tilt angles used to measure the peaks are $18^\circ(18.4^\circ)$, $14^\circ(14.05^\circ)$, $8^\circ(8.14^\circ)$, $6.2^\circ(6.35^\circ)$ and $5.8^\circ(5.2^\circ)$. The values in parentheses are the calculated tilt angles for the expected commensurate diffraction spot positions. Similar as in NiMnGa,[64] the modulations are along \mathbf{c}^* , which corresponds to the $\langle 110 \rangle_A$ directions

²In a commensurate superstructure, the basal planes have the same distance as in the non-modulated structure. In a reciprocal space map of a commensurate superstructure, the extra diffraction spots fit exactly between the diffraction spots of the non-modulated structure.

Table 5.2: The tilt and the crystallographic orientation is listed for selected martensitic peaks.

Diffraction spot	$\Psi_{\max}(deg)$	crystallographic orientation
$(0401)_{10M}$	6.2	$\langle 100 \rangle_A$
$(040-1)_{10M}$	5.8	$\langle 100 \rangle_A$
$(0401)_{4O}$	8	$\langle 100 \rangle_A$
$(400)_M$	2.6	$\langle 100 \rangle_A$
$(040)_M$	0	$\langle 001 \rangle_A$
$(004)_M$	2.6/1.8	$\langle 100 \rangle_A / \langle 110 \rangle_A$

in the austenite crystal structure. For the measured 4O (IC) superstructure the modulation vector is $\mathbf{q}_{4O} = 0.55\mathbf{c}^*$ and for the 10M (IC) superstructure $\mathbf{q}_{10M} = 0.42\mathbf{c}^*$. The superstructure peaks at lower 2θ values fit well to $2\mathbf{q}$. The corresponding commensurate modulation lengths would be $\mathbf{q}_{4O} = \frac{2}{4}\mathbf{c}^* = 0.5\mathbf{c}^*$ and $\mathbf{q}_{10M} = \frac{2}{5}\mathbf{c}^* = 0.4\mathbf{c}^*$. [64] The incommensurateness δ is usually given by $\mathbf{q}_{4O} = \gamma_c(1 + \delta)\mathbf{c}^*$, where γ_c is the parameter of a commensurate superstructure. The incommensurateness is $\delta_{4O} = 0.091$ for 4O and $\delta_{10M} = 0.047$ for the 10M superstructures. The 10M superstructure is close to the commensurate value, while the 4O structure shows a larger deviation.

Comparison of the martensite phase to literature values

A summary of the superstructures and the lattice constants found in this work and in the literature is given in Table 5.1. Compared to the literature, a reasonable agreement of the lattice constants and superstructures is seen. In most works with close composition, 4O and 10M superstructure are found as well. The lattice constants found in this work seem to be reasonable: The composition differs between the literature and SERIES B. The lattice constants are sensitive to a change in composition and hence a small deviation is expected.

Real space orientation

The real-space orientation of the observed martensitic unit cells is investigated by polefigure scans of the peaks $(0401)_{10M}$, $(040-1)_{10M}$, $(0401)_{4O}$, $(400)_M$, $(040)_M$

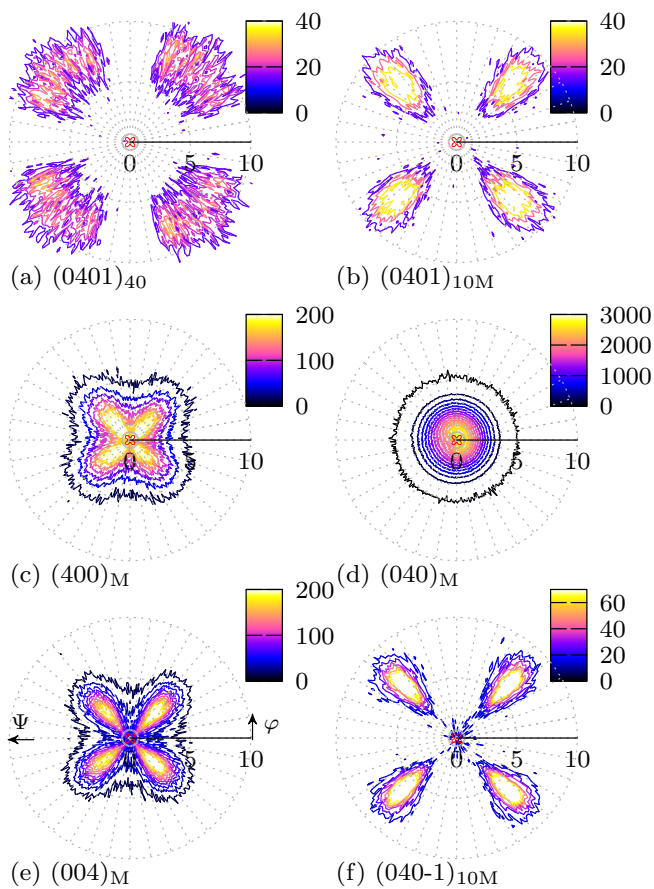


Figure 5.10: Pole figure measurements of the orthorhombic peaks and selected superstructure peaks. The four fold symmetry verifies epitaxial growth on the MgO substrate.

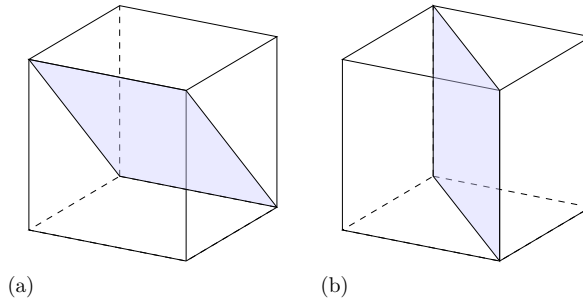


Figure 5.11: Two examples of 101 twinning planes. The type of twinning plane shown in (a) leads to polefigure reflections in $\langle 100 \rangle_A$ direction. Reflections in $\langle 110 \rangle_A$ direction are caused by the type of twinning plane shown in (b).

and $(004)_M$ (shown in Figure 5.10). The substrate is oriented such that the $[100]$ MgO direction is at $\varphi = 0^\circ$. Thus $\varphi = 45^\circ$ is the $[100]$ direction of Ni-Mn-Sn in the austenite phase ($[100]_A$). The $(040)_M$ pole figure is dominated by one reflection close to the substrate normal. The polefigures of the $(400)_M$ and $(004)_M$ peaks show four intense reflections in $\langle 100 \rangle_A$ orientation indicating four coherent variants. Due to an overlap of the $(040)_M$ and the $(400)_M$ peak a strong signal is also seen close to the origin of the $(400)_M$ peak. For the $(004)_M$ the overlap is negligible and variants with considerably less intensity are visible in the $\langle 110 \rangle_A$ directions. The polefigures of the 10M superstructure show maximal intensity in the $\langle 100 \rangle_A$ orientation. A much broader signal is measured for the polefigure of $(0401)_{4O}$. It is also oriented in $\langle 100 \rangle_A$, but in a broader φ range of about 30° . The information is summarized in Table 5.2 together with the tilt angle where the maximal intensity is observed.

The observed orientation of the polefigure of the $(400)_M$ and $(004)_M$ can be explained by twinning in the (101) plane. In Figure 5.11 two examples of the (101) planes are shown. There are 6 possible orientations of the twinning planes altogether. 4 orientations with an angle of 45° relative to the substrate normal as shown in (a) (TYPE A). 2 twinning planes perpendicular to the substrate

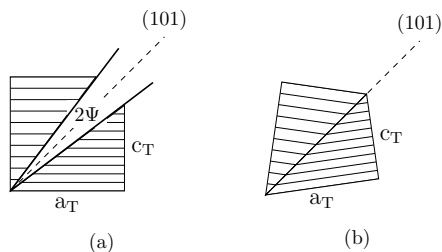


Figure 5.12: Rotation due to a coherent adjustment of two orientation variants of the tetragonal normal martensite along the (101) plane. The shading indicate the lattice planes relevant for XRD measurements. (a) a result of the cubic to tetragonal transformation. The rotation angle Ψ is the angle required to restore the crystal lattice continuity. In (b) the crystal with restored lattice continuity is shown.

as shown in (b) (TYPE B). The intense diffraction spots in $\langle 100 \rangle_A$ orientation can be caused by TYPE A twinning planes. TYPE B twinning planes can be the reason for the less intense diffraction spots in $\langle 110 \rangle_A$ direction. The observed tilt angles can be explained by $a_{\text{orth}} - c_{\text{orth}}$ and $b_{\text{orth}} - c_{\text{orth}}$ twinning in the (101) plane. For a coherent interface, a rotation of the variants is necessary. This rotation or tilt angle Ψ can be calculated by the following relation:[65]

$$\Psi = 45^\circ - \arctan(a_T/c_T) \quad (5.3)$$

where a_T and c_T are the tetragonal axes involved in the twinning. This is visualized in Figure 5.12. The measured maximal intensity at $\Psi = 2.6^\circ$ in $\langle 100 \rangle_A$ orientation fits well to $a_{\text{orth}} - c_{\text{orth}}$ twinning. With the measured lattice parameters, Ψ is calculated to 2.5° which is quite close to the observed value of $\Psi = 2.6^\circ$. The tilt angle $\Psi = 1.8^\circ$ observed in $\langle 110 \rangle_A$ orientation for the $(004)_M$ polefigure fits well to $b_{\text{orth}} - c_{\text{orth}}$ twinning. Ψ is calculated to 1.8° which is very close to the observed value of $\Psi = 1.8^\circ$. The lower amount of the TYPE B twins in comparison with TYPE A twins can be understood in terms of phase compatibility. The TYPE A twins can most likely form a better interface to the austenite layer close to the substrate³[65] and hence these are favored to the

³This austenite layer is verified by resistivity (section 5.5, magnetization (section 5.4) and phase field simulations (chapter 4)

TYPE B twins.

The superstructure polefigures show only diffraction spots in $\langle 100 \rangle_A$ orientations. This can be explained in the following way: A tilt along the $\langle 100 \rangle_A$ orientation corresponds to the $\langle 110 \rangle$ direction in reciprocal space. The superstructure spots occur only in $\langle 110 \rangle$ directions. This is visible at the reciprocal space map (see Figure 5.9 (b)). Hence, only in this orientation diffraction spots due to the superstructures are expected. The broader distribution of $(0401)_{4O}$ in the φ direction could be caused by the higher degree of incommensurateness compared to the 10M modulation leading to additional stacking faults.

Temperature dependence

The temperature dependence of the structural transformation is measured with XRD for the 100 nm thick film as shown in Figure 5.13 (a). At 375 K the sample is in the austenite state as can be seen by the high intensity of the $(004)_A$ peak and the very low intensity of the martensitic peaks. With decreasing temperature the intensity of the $(004)_A$ peak decreases, while the superstructure and orthorhombic peaks become more intense. The martensite start temperature M_s is around 340 K as will also be shown by resistivity measurements. In Figure 5.13 (b), the normalized integrated intensity of each diffraction spot is shown. The intensities of the superstructure peaks (4O, 10M) start to increase quite close to M_s . The peaks belonging to the orthorhombic phase start to intensify at around 335 K. The intensity of the 4O peak starts to increase at the same temperature as the 10M phase, but the trend with decreasing temperature is similar to the orthorhombic phase. Above M_s there is a very low but measurable intensity for the superstructure peaks, which can be explained by nucleation processes maybe close to defects in the premartensitic phase.

The temperature dependence of the lattice constants is presented in Figure 5.13 (c). Down to 335 K, a thermal contraction of the austenite phase is visible at the decreasing lattice constant a_{cub} . A linear fit is used to determine the austenite lattice constant $a_{\text{cub}} = 5.97 \text{ \AA}$ at room temperature. At 345 K the $(400)_M$ and $(004)_M$ peaks of the orthorhombic phase become visible, allowing to determine a_{orth} and c_{orth} . Both show a decreasing lattice constant with decreasing temperature. Due to an overlap of the $(004)_A$ and the $(040)_M$ peaks, the lattice constant b_{orth} becomes visible at lower temperatures compared to

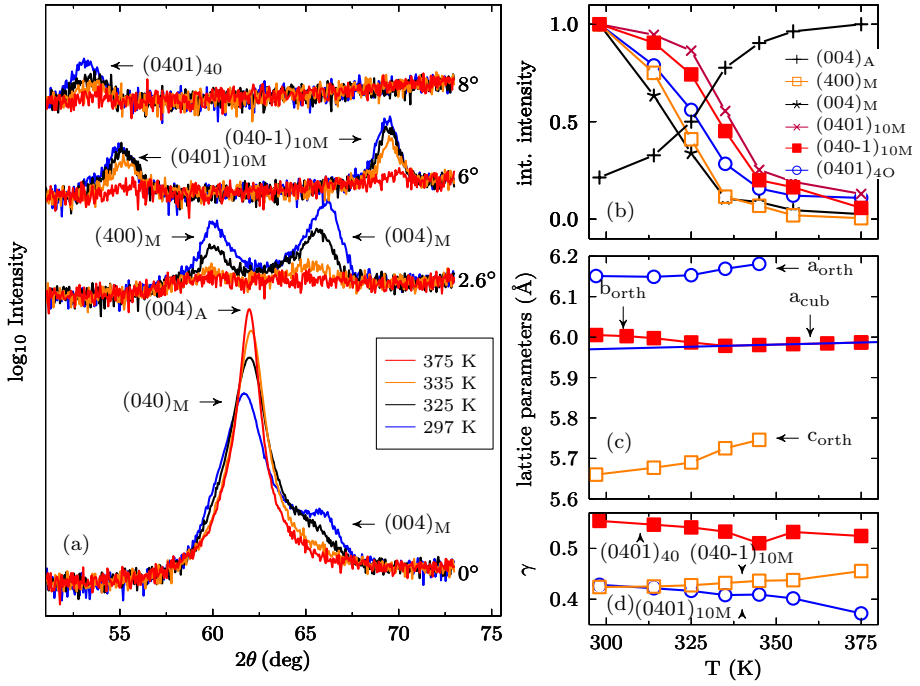


Figure 5.13: The XRD signal of the structural transformation of the 100 nm thin film of SERIES B is shown in (a). The normalized integrated intensity of all peaks is plotted in (b). In (c) the temperature dependence of the orthorhombic (martensite) and cubic (austenite) lattice constants is shown. The temperature dependence of the γ parameter is presented in (d). The sample is measured on the cooling branch of the thermal hysteresis.

the other two lattice constants.

The temperature dependence of the γ parameter of the modulation vectors $\mathbf{q} = \gamma \mathbf{c}^*$ belonging to the superstructure peaks is presented in Figure 5.13 (d). For the calculation the RT value of \mathbf{c}^* is used, since only here the (220) peak is measurable in this setup. With decreasing temperature the following trends are visible: the γ_{4O} parameter of the 4O phase increases. A small dip is visible at 345 K which could be caused by uncertainty of the \mathbf{c}^* value or the development of the orthorhombic phase.

At high temperature, the γ_{10M} parameter of the 10M peaks shows an asymmetric modulation length around the $(040)_M$ peak. This asymmetry becomes smaller with decreasing temperature and vanishes around 315 K. Between 335 K and 355 K the $(0401)_{10M}$ is close to the commensurate value.

A possible explanation for the asymmetry is based on the modulated lattice relaxation model[66] predicting a shift of the satellite peaks. The model is characterized by two assumptions:

- existence of sharp dip in the transverse phonon dispersion around $\mathbf{q} = 1/3[110]$
- existence of premartensitic nuclei

Both assumptions are valid for the investigated sample. A dip in the the TA_2 phonon branch at $\mathbf{q} = 0.35[110]$ has been calculated by Ağduk *et al.* [67] The asymmetry of the modulation vectors is visible in a temperature region before the martensitic transformation starts. This is a premartensitic phase where nuclei like the observed 10M and 4O phase exist. The general trend of an increase of the γ parameter with decreasing temperature has also been observed for a 10M superstructure in Ni-Mn-Ga by Righi *et al.* [64]

TEM

A further structural characterization at room temperature is carried out using TEM. In Figure 5.14, a TEM image along the $[011]_A$ zone axis of the 100 nm thick film is shown. In some regions nanotwins are visible. Most domains as well as the modulation of the nanotwins show an inclination in the range of 30° to 36° in respect to the MgO surface. This corresponds to (101) twinning planes which viewed from the $[011]$ direction show an inclination of 30° . An

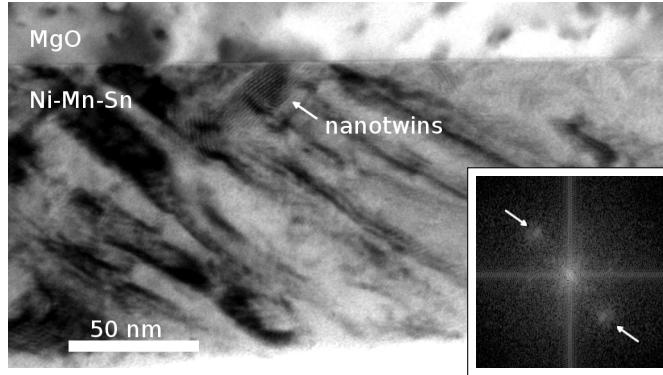


Figure 5.14: A TEM image along the $[011]_A$ zone axis of the 100 nm thick Ni-Mn-Sn film of SERIES B at room temperature is shown. A FFT of the region where the nanotwins are visible is shown in the inset. The arrows indicate the features due to the periodicity of the nanotwins.

FFT shown in the inset of Figure 5.14 of the region containing the nanotwins confirms these with a periodicity of approximately 1 nm.

Film thickness dependence of the martensitic structure

The influence of the film thickness on the structural properties at room temperature is shown in Figure 5.15 (a). With decreasing film thickness the following trends are visible: the shoulder due to the $(004)_M$ peak on the right side of the $(020)_M$ and $(040)_M$ peak decreases. The out-of-plane lattice constant first decreases down to 5.974 Å for 35 nm film thickness and then increases again up to a maximum of 6.005 Å for 10 nm thickness. This is shown in Figure 5.15 (b). Both trends, the decreasing lattice constant and the vanishing shoulder, are comparable to the temperature dependent XRD measurements of the martensitic phase transformation. These measurements show that the formation of martensite leads to an increase in the lattice constant and to the formation of the shoulders. Thus, these results indicate that the structural transformation shifts to lower temperatures with decreasing film thickness. This will also be shown by resistivity and magnetization measurements. The expansion of the out-of-plane lattice constant from 35 nm to 10 nm can be ascribed to a

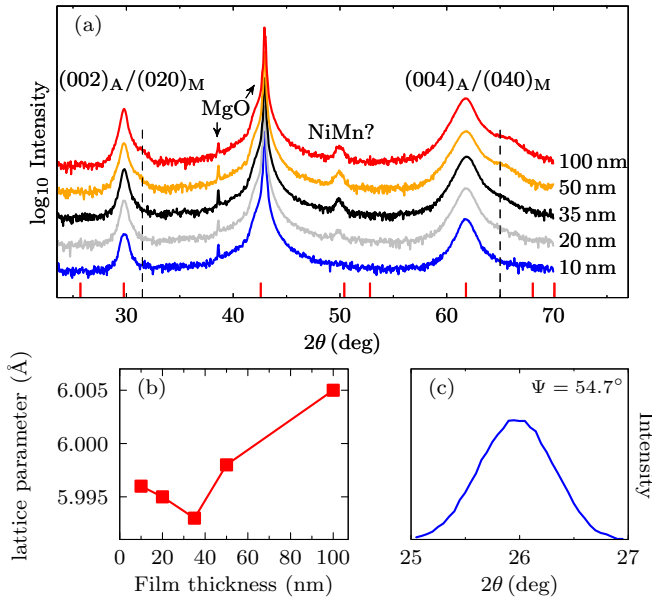


Figure 5.15: The XRD patterns of the thin films of SERIES B with different thicknesses at room temperature is shown in (a). The red bars show the Bragg positions of the Cubic phase. The dashed lines indicate the shoulder positions. The evolution of the lattice parameter with the film thickness is shown in (b). In (c) the (110) reflection of Ni-Mn-Sn is shown.

compression of the in-plane lattice due to the misfit to the MgO substrate. The influence of the MgO substrate reduces with increasing film thickness (see also section 5.2).

The (110) peak shown in Figure 5.15 (c) corresponds to the (111) superstructure peak of the $L2_1$ Heusler phase and thus also indicates a well ordered $L2_1$ structure of SERIES B.

Summary and Conclusion

To conclude, the temperature dependent XRD measurements show a structural transformation from a cubic austenite phase to a martensitic phase. The most

important findings are:

- The martensite phase is orthorhombic. Furthermore, modulated 10M and 4O phases are found.
- The martensitic transformation is also visible in the thickness dependent XRD measurements; these indicate a shift to lower martensite start temperatures with decreasing film thickness.

In the following sections, the influence of the film thickness on the martensitic transformation will be further investigated by magnetization (section 5.4) and resistivity measurements (section 5.5).

5.4 Magnetism

The magnetism of the austenite and martensite phase in $\text{Ni}_{50}\text{Mn}_{25+x}\text{Sn}_{25-x}$ is mainly determined by the interplay of the Mn_a atoms on the Sn sites (Wyckoff notation: 4a) and of the Mn_b atoms on the regular (Wyckoff notation: 4b) sites.[68, 69] The distortion of the lattice due to the martensitic transformation leads to a change in the interatomic spacing. This enhances anti-ferromagnetic coupling especially between the 4a and 4b sites.[68, 69] This also leads to different magnetic moments of Mn_a and Mn_b . The change of magnetic moments and coupling parameters shifts the martensite Curie temperature T_c^M to lower temperatures compared to the austenite.[50, 69] (see also Figure 5.2). As a consequence, the magnetization in the martensite phase is lower than in the austenite phase over a wide temperature range. Thus, a reduction of the magnetization can be observed for the transformation from a ferromagnetic austenite phase to the martensite.

Experimental results

The change of the magnetic properties during the MT is investigated in the following. The MT can be influenced by a magnetic field and hence a low field of 5 mT/15 mT is chosen to measure SERIES A/SERIES B. (see also section 5.8). The magnetization is measured in-plane. The temperature dependence of the magnetization is shown in Figure 5.16.

All thin films are ferromagnetic below the austenite Curie temperatures T_c^A which are estimated by differentiation of the magnetization. Below T_c^A , the measurements reveal a significant difference in the behavior of the two sample series.

The thin films of SERIES A show a rise of the magnetization of up to $1.1 \mu_B/\text{f.u.}$ The field cooled (FC) and field heated (FH) measurements do not retrace and a hysteresis is visible. The hysteresis is attributed to the martensitic transformation in these films. At the onset of the transformation from the austenite to the martensite phase (M_s), a drop in the magnetization is visible. This is due to the lower magnetization of martensite compared to austenite. For thinner films, M_s shifts to lower temperatures and the transformation range widens; this is visible at the wider temperature range where the magnetization drops.

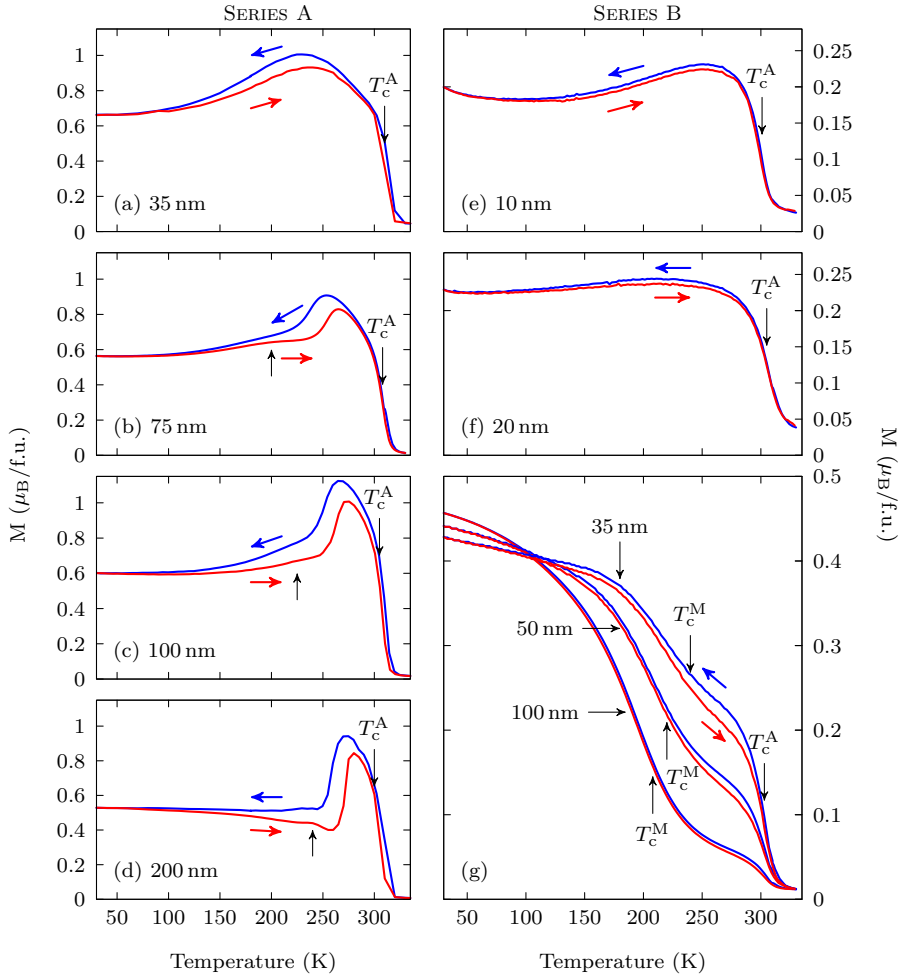


Figure 5.16: The magnetization in dependence of temperature is shown for SERIES A in (a) - (d) and SERIES B in (e) - (g). The samples of SERIES A have been measured with an applied field of 5 mT, the samples of SERIES B with an applied field of 15 mT. The austenite T_c^A and martensite T_c^M Curie temperature is marked in the plots. The arrows indicate field cooling (blue arrow) and field heating (red arrow). The black arrows in (b)-(d) mark possible martensite to austenite transitions.

The 200 nm thick film shows a kink during FC and FH at around 230 K and 240 K, respectively. It is marked by a black arrow for the FH curve. For the 100 nm and 75 nm thick films a kink is only visible during FH at around 220 K and 200 K, respectively. The thinner films have a larger fraction of austenite in this temperature range, possibly hiding the kinks. The decrease of the kink temperature might be an effect of the film thickness, possibly due to undercooling/overheating (see also the chapters 5.6 and 4). A possible explanation for the kink is a martensite to martensite transformation between different martensitic structures. Sutou *et al.* [62] measured two martensite to martensite transformations for $\text{Ni}_{50}\text{Mn}_{37}\text{Sn}_{13}$, where one of these transformations is at 250 K (257 K) for FC (FH).

SERIES B shows two Curie temperatures for films above 20 nm thickness; T_c^A of the austenite and T_c^M of the martensite phase. As has been shown in section 5.2, M_s is well above T_c^A and hence the samples are mainly in the martensitic state at T_c^A . The visible T_c^A stems from residual austenite. Similar as in SERIES A, a shift of the transformation to lower temperatures can be seen; this is noticeable at the higher degree of austenite at lower film thicknesses. Below 35 nm thickness, the films show a drop in the magnetization. This can be understood in the following way: the lower transition temperature and the widening of the transformation range leads to a higher fraction of austenite than martensite at T_c^A . With decreasing temperature, the martensite fraction increases. Hence, a drop in the magnetization can be observed. The upturn of the magnetization curves at low temperatures, visible for the 10 nm thick sample, stems from a paramagnetic contamination of the substrates.

The magnetization values at low temperatures are similar for all samples of SERIES A. The tendency is different for SERIES B: The magnetization decreases slightly for the films with a thickness above 20 nm. The 10 nm and 20 nm thick film show a large drop in the magnetization. The origin of this effect will be investigated in future studies. The differences in the transformation behavior and its origins will be discussed in section 5.7.

Curie temperatures

The Curie temperatures T_c^A and T_c^M as well as bulk values are summarized in Table 5.3. T_c^A is lower than the bulk value for all films. With decreasing film thickness, T_c^A of both sample series increase slightly. The 10 nm thick film

Table 5.3: The Curie temperatures of the austenite T_c^A and martensite T_c^M of both sample series as well as bulk literature values are listed.

h (nm)	10	20	35	50	75	100	200	bulk[50]
SERIES A								
T_c^A (K)			310		308	305	300	317
SERIES B								
T_c^A (K)	301	305	305	302		301		≈ 312
T_c^M (K)			240	225		195		203

of SERIES B is an exception; it shows the same T_c^A value as the 100 nm thick film of the same series. Both effects, the lower T_c^A and the variation with film thickness, could be caused by a different degree of chemical order or by lattice strain.

T_c^M of the 100 nm film is comparable to the bulk value for a similar stoichiometry. For thinner films, T_c^M increases from 195 K at 100 nm to 240 K at 35 nm film thickness. The rise of T_c^M can be caused by the higher degree of ferromagnetic austenite. The austenite couples to the paramagnetic martensite and hence leads to ferromagnetic order of martensite at higher temperatures.

Magnetic properties of the austenite and martensite phase

The temperature dependence of the magnetization of the 200 nm thick sample of SERIES A at 5 mT and 1 T is shown in Figure 5.17 (a). At 1 T, a clear increase of the magnetization is visible. The magnetization change at the MT is $0.7 \mu_B/f.u.$ at 1 T and $0.42 \mu_B/f.u.$ at 5 mT. These values are in agreement with literature values. Planes *et al.* [50] found a magnetization change of $1 \mu_B/f.u.$ at a magnetic field of 1 T for bulk $Ni_{50}Mn_{35}Sn_{15}$. The lower degree of magnetization change can be well explained by residual austenite in thin films. Furthermore, the transition of $Ni_{50}Mn_{35}Sn_{15}$ is at lower temperatures. Here, a higher drop in the magnetization is possible. For fields below 15 mT a reduced magnetization change has been measured by Planes *et al.* [50]

The reduced magnetization change can be understood when looking at hysteresis loops in the austenite and martensite phase. In Figure 5.17 (b) the

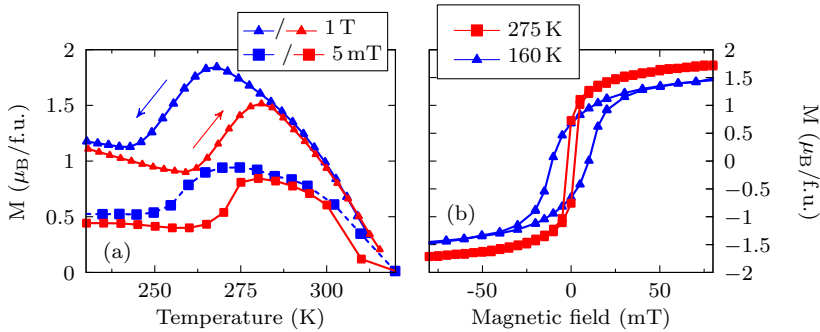


Figure 5.17: In (a) the temperature dependence of the magnetization at an applied field of 5 mT and 1 T is shown for the 200 nm thick film of SERIES A. The arrows indicate the temperature change direction. In (b) the magnetization in dependence of the magnetic field is shown for the 100 nm thick film of SERIES A. The hysteresis is measured at 275 K in the austenite phase and at 165 K in the martensite phase

magnetic field dependence of the magnetization for a 100 nm thick film of SERIES A is shown. The film thickness is different, however, the same trends should apply to the 200 nm thick sample. The thin film has been measured at two temperatures: At 275 K in the austenite phase, and at 160 K well in the martensite phase. Close to zero applied field, the difference between the magnetization curves decreases due to a lower coercive field of the austenite phase. Thus, at 5 mT the magnetizations difference between austenite and martensite is lower than at 1 T.

The coercive field increases from 2 mT in the austenite to 10 mT in the martensite phase. This behavior can be attributed to an increased crystalline anisotropy due to the tetragonal distortion. The easy axis of the magnetization is along the c-axes for a tetragonal unit cell. Hence, an out of plane orientation of the c-axis turns the easy axis out of plane. This leads to the observe increase in the coercive field. A similar trend has also been observed for Ni-Mn-Ga thin films.[70]

Summary

To summarize, clear signs of the MT can be observed in the magnetic behavior of both sample series. The most important characteristics are:

- The magnetization change for the 200 nm sample of SERIES A in the vicinity of the MT is in good agreement with literature values.
- The Curie temperature of the austenite and martensite are in good agreement with literature values.
- With decreasing film thickness, the transformation range widens and M_s shifts to lower temperatures. This results in:
 - A wide temperature range, where the magnetization decreases
 - A shift of the martensite Curie temperature to higher temperatures
- The coercive field of the martensite phase is larger compared to the austenite phase. This is caused by an increased crystalline anisotropy.

5.5 Electrical transport

Electric transport measurements are carried out to study the martensitic transformation of SERIES A and SERIES B. This characterization method is based on a resistivity increase due to the martensitic transformation. The resistivity can be measured in a very wide temperature range due to its independence of the Curie temperature and is thus advantageous for the here discussed sample series. The physical origin of the resistivity change can be linked to a variation of the density of electronic states close to the Fermi surface and a higher scattering probability due to defects.[71] The variation of the electronic density of states can be of magnetic and structural origin.[73] The magnetic origin of this variation can be explained by a formation of an antiferromagnetic lattice that is incommensurate with the crystal lattice, i.e. a magnetic superstructure, that induces a superzone gap in the Brillouin zone.[72, 73] The structural origin of this variation in the electronic density of states can be attributed to band shifts caused by the lattice distortion.[74, 71] Defects caused by the formation of twinning planes and dislocations during the transformation give additional contributions to the resistivity due to a reduced charge carrier mobility.

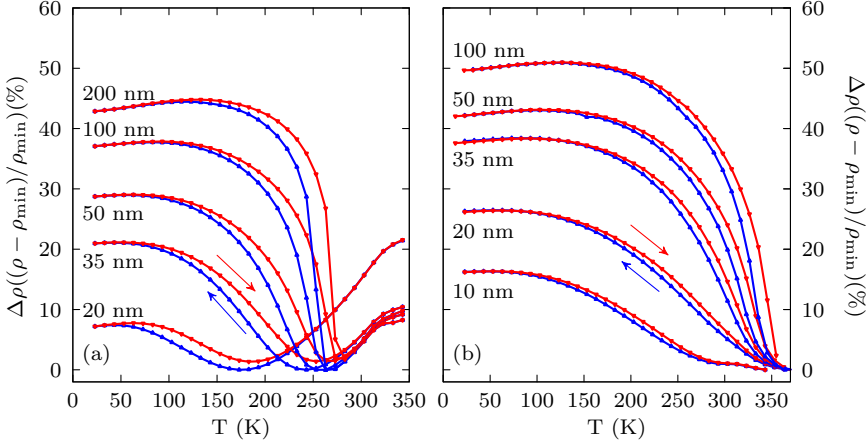


Figure 5.18: The relative resistivity change of SERIES A and SERIES B are shown in (a) and (b), respectively. The arrows indicate the temperature change direction.

Experimental results

The electric transport measurements are presented as relative changes of the resistivity, defined as $\Delta\rho(T) = (\rho(T) - \rho_{\min})/\rho_{\min}$, in Figure 5.18. The 75 nm thick film is omitted here for clarity. The signs of the martensitic transformation, increasing resistivity with decreasing temperature and a thermal hysteresis, are clearly visible for all film thicknesses of both sample series. Prior to the martensitic transformation there are distinct features visible in the $\Delta\rho(T)$ curves: SERIES A, presented in Figure 5.18 (a), shows a linear decrease in the resistance with a kink at the Curie temperature T_c^A . The linear decrease is due to electron-phonon interaction in metals. The kink is caused by the suppression of spin-disorder scattering due to the spontaneous magnetization below T_c^A . [75] The 10 nm sample of SERIES B, presented in Figure 5.18 (b), shows not only a kink but a cusp-like feature.⁴

⁴A very similar behavior has been observed by Chatterjee *et al.* [76] for bulk $\text{Ni}_{50}\text{Mn}_{38}\text{Sn}_{12}$ ($e/a = 8.14$), where the martensitic transition is also close to the Curie temperature. Kataoka [75] investigated possible influences on the anomaly at T_c^A . It was found that an increased mean free path of electrons, a lower electron concentration and a reduced stability of the ferromagnetic

In the martensite phase, after the hysteresis is closed, $\Delta\rho(T)$ is linear, but with a gentler slope compared to the austenite phase (see also Figure 5.19 (a)).

In the following the effect of the martensitic transformation on the resistivity is discussed. A few general trends can be observed in both sample series: For film thicknesses of 10 nm and 20 nm, a broad temperature range is observed. The slope of $\Delta\rho(T)$ in the transformation region is approximately constant over a wide temperature range. With increasing film thickness the slope of $\Delta\rho(T)$ becomes steeper and the transformation range is narrowed. Furthermore, the transformation shows two regimes. In the first regime a steep linear increase of $\Delta\rho(T)$ with decreasing temperature is observed. In the second regime, the slope of $\Delta\rho(T)$ is non-linear; it gets gentler with decreasing temperature.

The onset of the transition is reduced for low film thicknesses. This is best visible for the example of the 20 nm thin film of SERIES A. The amplitude of the complete resistance change caused by the transformation reduces with decreasing film thickness.

Discussion

The thickness dependence of the total resistivity change $\Delta\rho_{\max}$ and the transformation characteristics show qualitatively a different behavior for the two sample series. The first aspect is discussed in the following, while the transformation characteristics are reviewed in section 5.6

The total increase of the resistivity change $\Delta\rho_{\max}$ differs significantly, e.g. the 100 nm thick film of SERIES B shows about 50 % change while SERIES A's 100 nm thick film shows only 38 %. To understand the origin of this effect and the decrease of $\Delta\rho_{\max}$ with decreasing film thickness, the following model is proposed: Substrate constraints and local Mn concentration differences at the interfaces can lead to an austenite layer at the MgO interfaces which cannot transform.[65, 77] This assumption is also supported by the simulations results

state lead to a more pronounced cusp. Since this cusp occurs close to a martensitic transition, premartensitic effects such as nuclei at defects are a likely cause. These nuclei can weaken the magnetic interactions or lower the carrier density. The magnetic interactions are lowered due to the lower Curie temperature of the martensitic nuclei. The carrier density can be reduced due to the structural transformation.[74, 71, 73] This fits well to the findings of Kataoka[75]. A reduced free path of electrons due to the nuclei weakens the cusp. Hence, with the assumption that the lower magnetic interactions and the reduced electron density have a stronger influence than the reduced mean free path, premartensitic nuclei are a likely cause for the cusp. All films above 10 nm thickness of SERIES B show the martensitic transition well above T_c^A , hiding the cusp.

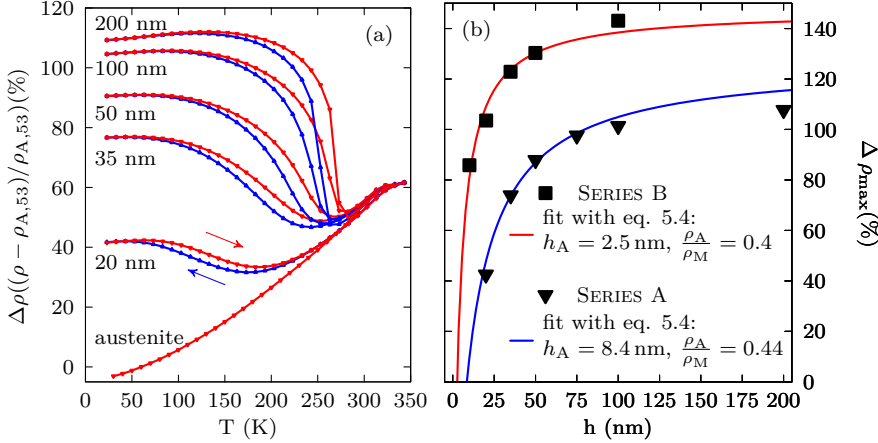


Figure 5.19: The resistivity of SERIES A and a 20 nm thin film, that is stable in the austenite phase, is shown in (a). All resistivities are normalized to a common value at 343 K. In (b) the total resistivity change at a temperature of 53 K is plotted. A fit with eq. 5.4 is applied. The arrows indicate the temperature change direction.

(see chapter 4) and the magnetization measurements of SERIES B (see section 5.4), where a clear signal of residual austenite is visible. This austenite layer gets a pronounced influence with decreasing film thickness. Due to the lower resistivity of the austenite, a decrease of $\Delta\rho_{\max}$ can be expected. With the assumption of an austenite layer and a martensite layer, we can propose a parallel resistance model. In this model, the relative total resistivity change $\Delta\rho_{\max}$ would be:

$$\frac{\Delta\rho_{\max}}{100} = \frac{h}{h_A + \frac{\rho_A}{\rho_M}(h - h_A)} - 1 \quad (5.4)$$

where h is the film thickness, h_A the thickness of the austenite layer, ρ_M/ρ_A the resistivity of the martensite/austenite phase. For the correct description of h_A , the austenite resistivity ρ_A at low temperatures and a renormalization of the resistivity change to ρ_A is required. ρ_A is approximated using the resistivity data of a 20 nm thin film with a slightly deviating composition. This film shows no martensitic transformation and a comparable resistivity behavior.

An example of the renormalized resistivity curves of SERIES A and of the austenite sample is shown in Figure 5.19 (a). As a common temperature for the renormalization, the measurement values at 53 K are chosen. The resistivity values are also normalized to a common value at 343 K. The same procedure is done for SERIES B. Both, $\Delta\rho_{\max}$ and the fit with Eq. 5.4, is shown in Fig. 5.19 (b) for both sample series. The fit shows a good agreement to the experimental data. According to the fit a austenite layer thickness of $h_A=8.4 \text{ nm}/h_A=2.5 \text{ nm}$ is present in the samples of SERIES A/SERIES B. The higher austenite fraction of SERIES A fits well to the lower $\Delta\rho_{\max}$ values. Thus, the different austenite layer thickness is most likely the reason for the observed $\Delta\rho_{\max}$ values. The sample quality and the phase compatibility between austenite and martensite could be the cause of differing austenite fractions. A detailed discussion on the possible influences on the transformation behavior and its relation to the residual austenite can be found in section 5.7.

The fit with eq. 5.4 gives information about the ratio of $\rho_A^{53K}/\rho_M^{53K}$, as well. It is 0.4 for SERIES B and 0.44 for SERIES A. To get a more comparable quantity for both sample series, the ratio

$$\frac{\rho_M^{53K}}{\rho_A^{343K}} = \frac{\rho_M^{53K}}{\rho_A^{53K}} \times \frac{\rho_A^{53K}}{\rho_A^{343K}} \quad (5.5)$$

is calculated. The ratio of $\rho_A^{53K}/\rho_A^{343K}$ is derived from the resistivity of the thin film that is stable in the austenite phase.

The value of $\rho_M^{53K}/\rho_A^{343K}$ is 1.38 for SERIES A and 1.51 for SERIES B. The experimental values are summarized together with literature values in Table 5.4. The experimental results are comparable to bulk samples with similar composition.

In the here assumed model of a thin austenite layer, some possible influences have been neglected: Different kinds of martensitic structures that can lead to other ρ_M values. The resistivity of the austenite at 53 K can be different for the thin films. Furthermore, effects due to anisotropic conductance in a mixture of austenite and martensite can lead to an increasing resistivity with decreasing film thickness.[79] All these influences can also have an impact on the fit results.

Table 5.4: The resistivity ratio of martensite to austenite is shown for SERIES A and SERIES B together with bulk literature data.

Composition	e/a	$\rho_M^{53K} / \rho_A^{343K}$
SERIES A		
Ni _{51.6} Mn _{32.9} Sn _{15.5}	8.083	1.38
Ni ₅₀ Mn ₃₆ Sn ₁₄ [76]	8.08	1.31
Ni ₅₀ Mn ₃₆ Sn ₁₄ [78]	8.08	1.48
SERIES B		
Ni _{51.6} Mn _{34.9} Sn _{13.5}	8.143	1.51
Ni ₅₀ Mn ₃₈ Sn ₁₂ [76]	8.14	1.44

Origins of the resistivity change in the martensite phase

In the beginning of this section, possible origins of the resistivity increase due to the MT, a variation of the electronic density of states close to the Fermi level due to different magnetic or structural phases and defects, have been discussed. In the following, the impact of each contribution is studied. The contribution of magnetic effects can be studied using SERIES B. In the case of 35 nm up to 100 nm thick films, most of the resistivity increase is in a temperature range above T_C^M . Thus, the main impact on the resistivity increase should be due to the different structural phase and defects. Magnetic superstructures are unlikely, because the martensite phase is not magnetic in this temperature range. An indication of the importance of defects can be achieved by comparing the slopes of $\Delta\rho$ vs. T at low temperatures. They show a pronounced difference for the austenite and martensite samples (see Figure 5.19 (a)). The gentle progression of $\Delta\rho(T)$ of the samples in the martensitic state indicate a high residual resistivity at 0K. A high residual resistivity is caused by defects such as twinning planes and dislocations.

Summary

To summarize, clear signs of the MT can be observed in the resistivity behavior of both sample series. The most important findings are:

- A widening of the transformation range and a shift of M_s to lower temperatures with decreasing film thickness is found. This is in good agreement with the magnetization measurements.
- The thickness dependence of the maximal resistivity increase due to the MT is well described by a parallel resistance model assuming a thin austenite layer at the MgO interface. The model gives information about:
 - the austenite layer thickness. The austenite layer of SERIES A is thicker than SERIES B's. This could be caused by a different phase compatibility and sample quality.
 - the resistivity ratio of the austenite and martensite phase. The results are in good agreement with bulk literature values.
- The main influences on the resistivity change during the MT are most likely the structural change leading a variation in the electronic density of states at the Fermi level and defects.

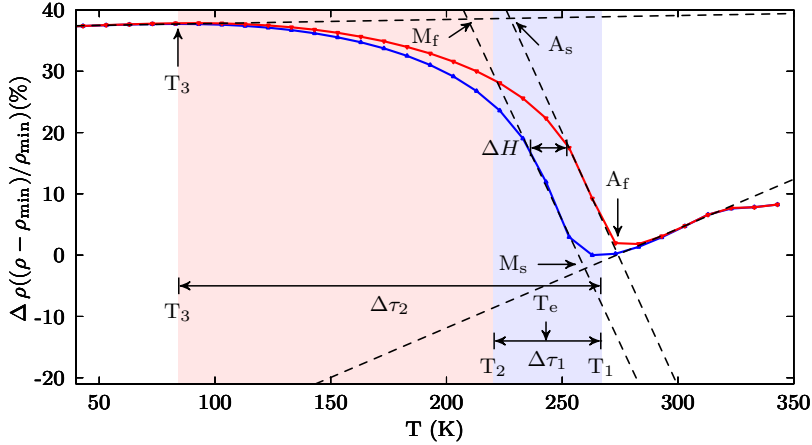


Figure 5.20: The analysis of the martensitic transformation is shown for the example of the 100 nm thick film of SERIES A. The blue colored area corresponds to the linear transition region $\Delta\tau_1$. The red colored area shows the non-linear transition region.

5.6 Analysis of the martensitic transformation

In this section, the procedure and all necessary values to quantify the MT are introduced on the basis of a measurement example. The normalized resistivity measurement of a 100 nm thick sample of SERIES A is shown in Figure 5.20. The characteristic temperatures of a martensitic transformation (M_s , M_f , A_s , A_f) are deduced by the common method [2, 80] of extrapolating linear regions and calculating the interceptions of those extrapolations. For example, M_s is obtained by extrapolating the linear region of $\rho(T)$ in the austenite and the linear range during the forward transition. The interception of these two lines marks M_s .

The real hysteresis, i.e. the range where the heating curve does not retrace the cooling curve, is wider than the temperature range between the calculated M_f and A_f values; at low temperatures the slope of $\Delta\rho(T)$ diverges from the linear approximation and flattens at the edges of the hysteresis. Two different transition ranges are defined to quantify the range of the linear regions $\Delta\tau_1$

Table 5.5: The characteristic temperatures and the Hysteresis width ΔH for both sample series.

h (nm)	M_s (K)	A_f (K)	M_f (K)	A_s (K)	ΔH (K)
SERIES A					
20	207	215	64	90	27.9
35	244	254	107	126	19.3
50	252	263	159	176	17.5
75	255	269	197	216	18.5
100	259	274	212	228	16.8
200	263	275	233	255	17.6
SERIES B					
10	281	290	116	125	9.6
20	331	339	151	164	10.8
35	330	336	218	232	9.8
50	335	344	254	263	9.2
100	347	358	288	302	13.0

and the complete transition range $\Delta\tau_2$. The first definition $\Delta\tau_1$ is defined as $\Delta\tau_1 = T_1 - T_2$ where $T_1 = (M_s + A_f)/2$ and $T_2 = (M_f + A_s)/2$. For $\Delta\tau_2$ the end of the transition has to be found. Here the temperature T_3 where the maximal resistivity occurs is chosen as reference. $\Delta\tau_2$ is then defined as $\Delta\tau_2 = T_1 - T_3$. A further value important for further analysis is the temperature T_e defined as $T_e = (T_1 + T_2)/2$. This is the average temperature of forward and reverse transformation where the transformation is half way in the linear approximation. Here, the fraction of austenite and martensite should be equal. The width of the hysteresis ΔH is determined using the linear extrapolations of the transformation. ΔH is evaluated at the temperature where the resistivity increase of the forward and reverse transformation is equal to $\rho_{\max}/2$. This approximates the temperature where the fraction of martensite and austenite are equal. The characteristic temperatures and the hysteresis width are summarized in Table 5.5. The M_s temperatures of the thickest films of SERIES A and SERIES B are in good agreement with the bulk literature values. The bulk value

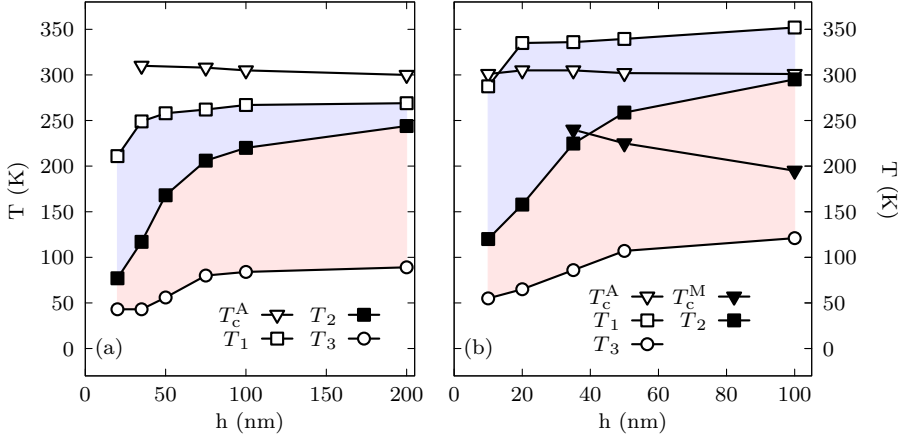


Figure 5.21: The structural and magnetic phase diagram is shown in (a) for SERIES A and (b) for SERIES B. $T_1 = (M_s + A_f)/2$ is the average temperature above which the austenite phase is stable. $T_2 = (M_f + A_s)/2$ is the average temperature above which martensite loses stability in the linear approximation. Above T_3 martensite loses stability. T_c^A and T_c^M are the austenite and martensite Curie temperatures, respectively. The blue colored area corresponds to the linear transition region $\Delta\tau_1$. The red colored area shows the non-linear transition region.

for SERIES A/SERIES B is 255 K/357 K. This is quite close to the measured M_s temperatures 263 K and 347 K for SERIES A and SERIES B, respectively.

A general overview of the transition temperatures (T_1, T_2, T_3) and the Curie Temperatures (T_c^A, T_c^M) in dependence of the film thickness is presented in Figure 5.21. Both sample series show the general trend of reducing transition temperatures with decreasing film thickness. The film thickness has the largest influence on T_2 , which is the average temperature where the martensite phase loses stability in the linear approximation. A comparison with T_3 shows that the linear approximation gets better for low film thicknesses. For example the difference between T_2 and T_3 changes by more than a factor of 4 from 155 K of the 200 nm sample to 34 K of the 20 nm sample of SERIES A. T_3 itself is also dependent on the film thickness; it reduces below 100 nm film thickness. T_1 ,

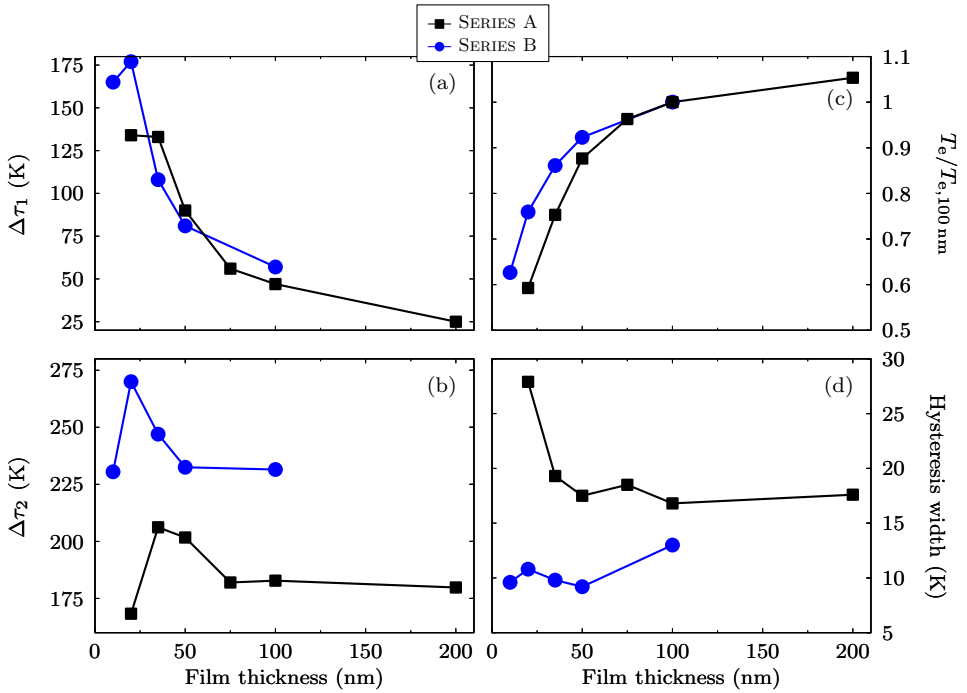


Figure 5.22: In (a) the transition range $\Delta\tau_1$ using the linear approximation is shown. The complete transition range $\Delta\tau_2$ is presented in (b). The temperature T_e is normalized to the value at 100 nm. It is shown in (c). The hysteresis width is plotted in (d).

which is the average temperature where the austenite phase loses stability, shows the least dependency on the film thickness; large temperature drops are only visible for very thin films. This leads to an increase of both transformation ranges $\Delta\tau_1$ and $\Delta\tau_2$ with decreasing film thickness as shown in Figure 5.22 (a) and (b), respectively. $\Delta\tau_1$ increases rapidly for SERIES A by more than a factor of five from 25 K of the 200 nm sample to 134 K of the 20 nm thick film. SERIES B shows a similar behavior between 100 nm and 50 nm thickness. For the films thinner than 50 nm, $\Delta\tau_1$ of SERIES B increases rapidly up to a maximum of 177 K for 20 nm film thickness. $\Delta\tau_2$ shows a large difference between the

two sample series. At 100 nm thickness, $\Delta\tau_2$ of SERIES B is 48 K wider than SERIES A's. Up to 75 nm/50 nm film thickness, SERIES A/SERIES B show no significant change in the width of $\Delta\tau_2$. Below 75 nm/50 nm thickness, a rise of $\Delta\tau_2$ is visible with a maximum at 35 nm/20 nm film thickness for SERIES A/SERIES B, respectively. For the thinnest films of both sample series, $\Delta\tau_2$ decreases again due to a lower T_1 value. Generally, $\Delta\tau_2$ for SERIES B is much wider than for SERIES A over the whole thickness range.

The film thickness dependence of the transition temperatures in the linear approximation can be well compared using T_e . For this, T_e is normalized to the maximal value at 100 nm thickness. It is shown in Figure 5.22 (c). It can be clearly seen, that T_e of SERIES A decreases more rapidly with decreasing film thickness than SERIES B.

The width of the hysteresis ΔH presented in Figure 5.22 (d) shows the largest deviations between SERIES A and SERIES B. Similar to T_1 , T_3 and $\Delta\tau_2$, there is no large change between 200 nm and 100 nm thickness of SERIES A for ΔH . Small variations of ΔH occur down to 50 nm. Below 50 nm a steep increase is visible from 18 K at 50 nm up to 28 K for 20 nm film thickness. SERIES B shows overall a smaller ΔH and the opposite trend with reducing film thickness: ΔH drops from 13 K for 100 nm down to 9 K for 50 nm thickness. Below 50 nm, there is no clear trend visible; ΔH varies around 10 K.

5.7 Origins of the transformation behavior

The influence of the film thickness and composition on the transformation behavior can be of multiple origin. The possible causes can be classified into five major groups:

1. Size scale effects
2. Rigid substrate/clamping
3. Crystal/sample quality
4. Phase compatibility
5. Martensite to martensite transformation between different martensitic structures

The theoretical basics of these effects have been introduced in section 2.1. At first, the results on the sample quality are shortly reviewed. Subsequently, the phase compatibility of both sample series is determined. In the last part the transformation behavior is compared and discussed to the theoretical models and experimental data.

Review of the sample quality

Here, the results of section 5.2 are shortly reviewed. The sample quality in the austenite phase shows differences between SERIES A and SERIES B. The lattice mismatch to the MgO substrate is larger for SERIES A than for SERIES B. This indicates a larger dislocation density close to the substrate for SERIES A. This is also visible at the rocking curve width. The out-of-plane grain size as approximated by the Debye-Scherrer formula is similar for both series. The precipitate fraction decreases with increasing film thickness and is the highest for the 20 nm thick sample of SERIES A. The 10 nm sample of SERIES B is an exception: It shows no precipitate, a very low rocking curve FWHM and a low dislocation density.

Phase compatibility

The necessary data to determine the eigenvalue λ_2 is experimentally only available for SERIES B. However, an approximation based on literature values can be made for SERIES A. Brown et al.[63] determined the lattice parameters of the martensite phase for $\text{Ni}_{50}\text{Mn}_{36}\text{Sn}_{14}$ ($e/a=8.08$) with $M_s = 221$ K which is reasonable close to SERIES A ($\text{Ni}_{51.6}\text{Mn}_{32.9}\text{Sn}_{15.5}$, $e/a=8.083$) with $M_s = 263$ K. One of the six transformation stretch matrices for the cubic to orthorhombic transformation is given by:[8]

$$\mathbf{U} = \begin{pmatrix} \beta & 0 & 0 \\ 0 & \frac{\alpha+\gamma}{2} & \frac{\alpha-\gamma}{2} \\ 0 & \frac{\alpha-\gamma}{2} & \frac{\alpha+\gamma}{2} \end{pmatrix} \quad (5.6)$$

where $\alpha = a/a_0$, $\beta = b/a_0$ and $\gamma = c/a_0$. With the lattice values of SERIES A $a_0 = 5.985 \text{ \AA}$, $a = 6.16 \text{ \AA}$, $b = 5.6 \text{ \AA}$, $c = 6.07 \text{ \AA}$ and SERIES B $a_0 = 5.97 \text{ \AA}$, $a = 6.156 \text{ \AA}$, $b = 5.644 \text{ \AA}$, $c = 6.005 \text{ \AA}$ we find $\lambda_2 = 1.014$ for SERIES A and $\lambda_2 = 1.005$ for SERIES B. Thus, the phase compatibility of SERIES B is better than SERIES A's.

Table 5.6: The fit results and parameters of the Malygin model.[28]

	l (nm)	k_a	k_0	$k_B T_{e0}/q\omega$	Λ (nm)	d (nm)
SERIES A	40	1	1.4	0.0064	25	50
SERIES B	40	1	2	0.0064	25	50

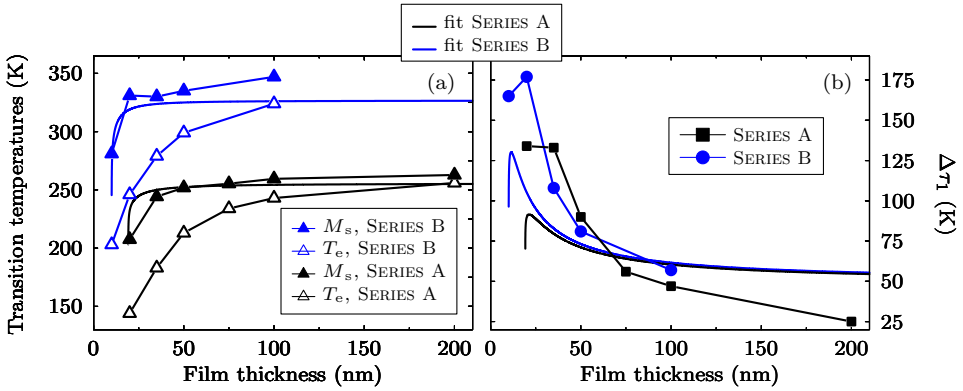


Figure 5.23: T_e and M_s is shown in (a). A fit with eq. 2.10 to T_e is applied. In (b) the transformation width in the linear approximation is shown. A fit with eq. 2.11 is applied. The fit results are presented in Table 5.6

Discussion

The discussion is structured according to the five major causes introduced above. Note that for example the sample quality and the phase compatibility influence the same parameters.

Size scale effects

At first, the size scale effects on the transformation are discussed. For this, the two characteristic values, T_e and $\Delta\tau_1$, are compared with the Malygin model. It is not possible to compare $\Delta\tau_2$, because a linear transformation is assumed in this model. T_e and $\Delta\tau_1$ are plotted together with the fits of eq. 2.10 and eq. 2.11 in Figure 5.23. Since both equations rely on the same parameters, a

multi branch fit routine is used to achieve the best fit to both data sets. k_0 and k_a are unknown and similar values as used by Malygin[28] are assumed. All parameters are set to the same value for both series except k_0 ; this is a material dependent parameter and has also been used in [28] to adjust the fit to different materials. A complete list of the parameter set is given in Table 5.6. The values for grain size and defect distance are reasonable in comparison with the experimental available data. The nucleus diameter l of 40 nm is in good agreement with the literature; Yu *et al.* [81] found 34 nm length for an oblate nucleus.

A qualitative agreement of the fit to the experimental data is visible: The Malygin model predicts a sudden drop of T_e at the *critical thickness*. Below this thickness, the transformation is completely suppressed. SERIES A shows a drop of T_e at higher film thicknesses than SERIES B. This trend is well reproduced by the fit. The model predicts a critical film thickness of 18 nm for SERIES A and 8 nm for SERIES B. However, the experimentally measured T_e does not follow the fit exactly; T_e decreases at higher film thicknesses compared to the fit.

The increase in $\Delta\tau_1$ towards lower film thicknesses is well reproduced by the fits. For SERIES B the expected drop close to the critical thickness is visible. The smaller increase of $\Delta\tau_1$ for a higher critical film thickness of SERIES A is well described. However, the fits overestimate $\Delta\tau_1$ for larger film thicknesses and underestimate $\Delta\tau_1$ for thinner films.

The failure to reproduce the exact features of the transformation can be caused by wrong assumptions in the model or neglected influences. Among these assumptions are a constant defect distance Λ and grain size d , while the rocking curve and the degree of contamination indicate at least a lower value for Λ for the thin films of SERIES A. Among the neglected energy contributions are the interphase/grain boundary energy as well as strain energy as proposed by Meng *et al.* [19] These contributions could also lead to a shift of M_s and T_e towards lower temperatures. The neglect of the rigid substrate is the most likely reason for the failure to reproduce the exact features of the transition. As comparison, the M_s values are plotted in Figure 5.23 (a). The fit reproduces the behavior of the M_s values quite well. The influence of the rigid substrate on this parameter is much lower, if the substrate does not induce a high stress level in the thin film. This would be the case for a large lattice mismatch, which is not the case for the here investigated films.

To summarize, the Malygin model describes only qualitatively the trend

of decreasing T_e and increasing $\Delta\tau_1$ with decreasing film thickness. Quantitatively, large deviations can be observed.

Rigid Substrate

Most likely the effect of the rigid substrate is the dominant influence on the transition. This is supported by the large undercooling needed to achieve complete transformation as shown by the $\Delta\tau_2$ values. The transformation behavior is in good agreement with the calculated transition curves in chapter 4: the transformation is suppressed close to the substrate until the necessary driving force in form of chemical energy is provided. This leads to a shallow transformation curve in very thin films and to the observed different transformation regions $\Delta\tau_1$ and $\Delta\tau_2$ for thicker films.

Sample Quality

The sample quality can have influence on:

- critical film thickness
- residual austenite
- hysteresis width
- undercooling

All aspects are influenced by the interaction probability of defects with the interfaces of the martensite phase. Thus, a different number of defects can change the MT significantly. Additionally, different grain sizes can lead to confinement effects as proposed by Malygin [28]. Furthermore, different interphase/grain boundary energy as well as strain energy can be expected. [19]

The sample qualities of both series differ towards thinner films. This indicates a large influence of the thin film/substrate interface on the sample quality. Thus, close to the substrate a different defect density is expected compared to the average value of the thin film. This applies especially for thicker films.

The hysteresis width ΔH should depend on the average value of the defect density. Thus, an influence of the film thickness is expected only for thinner films. This is seen in the experimental results: ΔH correlates quite well for SERIES B in the thickness range of 50 nm down to 10 nm. At first, ΔH increases

to a maximum at 20 nm thickness and then decreases for the 10 nm sample. Both rocking curve FWHM and the precipitate fraction show the same behavior. SERIES A shows a correlation of ΔH with the rocking curve FWHM and precipitate fraction in the thickness range of 50 nm down to 20 nm.

The residual austenite fraction should only be influenced in the area close to the substrate. On the average, SERIES B has a better sample quality than SERIES A. Hence, for all thicknesses a higher degree of residual austenite is expected for SERIES A. This fits well to the experimental results. The electrical transport measurements show a higher residual austenite fraction for SERIES A.

The importance of the region close to the substrate on the critical film thickness becomes larger with decreasing film thickness. Thus, the lower critical film thickness of SERIES B might be influenced by the better sample quality.

An influence of the dislocation density/ grain misorientation on undercooling is not visible. On the average, $\Delta\tau_1$ and $\Delta\tau_2$ are larger for SERIES B than for SERIES A. The dislocation density/ grain misorientation of the sample series is similar above 20 nm film thickness and larger for the 20 nm thick film of SERIES A. Hence, a large influence of the dislocation density/ grain misorientation is unlikely. However, slight composition gradients can induce some variation in the transition temperatures. This would increase $\Delta\tau_2$.

Phase compatibility

The phase compatibility can have influence on:

- critical film thickness
- residual austenite
- hysteresis width
- undercooling

The influence of the phase compatibility can be understood in the following way: A better phase compatibility leads to a coarser laminate structure. A lower number of interfaces reduces the probability of interaction with defects. Thus the transition is less hindered by defects. Furthermore, a coarser laminate

structure requires less energy for its formation due to the lower number of interfaces. This effect becomes important at low film thicknesses: Here a high chemical energy is required to overcome the additional energy contributions of the substrate. Thus, the importance of a higher energy due to a finer laminate structure increases with decreasing film thickness. Both, the additional energy and the probability to interact with defects, can have a large influence on the critical film thickness, the residual austenite, undercooling and the hysteresis width. SERIES B has a lower critical film thickness, a lower fraction of residual austenite and a lower hysteresis width than SERIES A, which agrees well with the better phase compatibility of SERIES B.

The influence of the phase compatibility on the hysteresis width can be predicted by eq. 2.6. If we assume the same parameter values for both series, a factor of 1.35 between ΔH of SERIES B and SERIES A is calculated. This value is quite close to the experimental value of 1.29 for the difference in ΔH between the 100 nm thick films. For thinner films, a much larger difference between ΔH and even a different trend is visible: ΔH of SERIES B reduces below 100 nm film thickness, while ΔH of SERIES A varies only marginally and increases below 50 nm thickness. In the region above 50 nm thickness, an influence due to different sample quality is unlikely (see discussion above). Instead, a change of λ_2 with decreasing film thickness could be a possible cause. The phase compatibility can be influenced by different lattice constants of the austenite or the martensite phase. A change of the austenite lattice constant leads to the same variations of λ_2 for both sample series. Hence, this cannot be the reason for the different trend in ΔH . However, different martensitic structures are possible. König *et al.* [82] found a decreasing hysteresis width with decreasing film thickness even down to $\Delta H = 0$ K in an alloy with λ_2 close to 1; the origin for the variation was determined to be a change in the tetragonality of the martensitic structure. Future investigations with low temperature XRD measurements will clarify this issue for the here investigated films.

The degree of undercooling seems not to be related to the phase compatibility. $\Delta\tau_1$ of SERIES B is larger than SERIES A's for almost all film thicknesses. $\Delta\tau_2$ of SERIES B is significantly larger than SERIES A's. This is unexpected, since the phase compatibility of SERIES B is better than SERIES A's. A possible explanation might be the occurrence of different martensitic structures at lower temperatures. These would change the phase compatibility. Hints for this have been observed in the magnetic measurements of SERIES A (see section 5.4).

Martensite to martensite transformation

A martensite to martensite transformation between different martensitic structures, observed in the magnetic measurements of SERIES A, can lead to undercooling and a change in the phase compatibility. The undercooling due to the martensite to martensite transition is caused by the energy required for the transformation. Sutou *et al.* [62] found undercooling in the range of about 50 K involving two martensite to martensite transitions. Thus, a martensite to martensite transformation can be responsible for some additional undercooling. However, the whole $\Delta\tau_2$ range of around 200K cannot be explained. A change in the phase compatibility due to a martensite to martensite transformation can have influence on the hysteresis width, undercooling, residual austenite and the critical film thickness. Here, only a possible influence on undercooling ($\Delta\tau_2$) has been observed.

Conclusion

To conclude, the rigid substrate has large influence on the transformation of the thin films. This is visible at the large degree of undercooling required. Additionally, size scale effects and confinement of the nucleus as proposed by Malygin can change the transformation behavior. However, the effects predicted by this model fit only qualitatively. Effects such as energy terms due to interphase/grain boundaries and strain energies as proposed by Meng *et al.* could also influence the onset of the transition.

The differences between the two sample series could be caused by different sample quality and the phase compatibility (λ_2 parameter). SERIES B shows a better phase compatibility and a better sample quality close to the MgO/thin film interface. Thus, this combination might lead to the observed smaller hysteresis, lower critical film thickness and also less residual austenite of SERIES B. A martensite to martensite transformation could explain the wider transformation range $\Delta\tau_2$ of SERIES B. Influences due to composition gradients cannot be excluded. They could also influence the transformation range $\Delta\tau_2$.

5.8 Magnetoresistance

Magnetoresistance (MR) is a change in electric resistivity ρ by applying a magnetic field B :

$$MR = \frac{\rho(B) - \rho(0\text{T})}{\rho(0\text{T})} \quad (5.7)$$

The origin of the magnetoresistance in magnetic metals can generally be classified into orbit and spin contributions. The orbit contribution is based on a change in electron orbit under electric and magnetic fields due to Lorentz force. The spin contribution is due to electron scattering by e.g. spin fluctuations or spin disorder in a magnetic metal; it is correlated with the magnetization M and can be described by the following relation [83, 84]:

$$MR = -A \left(\frac{M(T, B)}{M_{\text{sat}}} \right)^2 \quad (5.8)$$

where A is a constant and M_{sat} the saturation magnetization. The MR usually shows a large decrease towards lower temperatures; this is only due to the enhancement of the magnetic resistivity value at zero magnetic field with rising temperature. Major contributions to the MR stem from electron-magnon scattering.[85].

In the Mn rich Ni-Mn-X ($X = \text{In, Sn, Sb}$) alloys, additional magneto resistance effects have been found during the martensitic transformation. Two major contributions to the MR of the MT have been identified:

- Magnetic field induced austenite (MFIA)
- Interface scattering

The MFIA effect can be understood as follows: The energetic contribution of the magnetic field to the Gibbs energy is given by:[2]

$$G = U - TS - \mu_0 HM \quad (5.9)$$

where $\mu_0 HM$ is the Zeeman energy. Since the magnetization is higher in the austenite than in the martensite (see also section 5.4), an applied magnetic field favors the austenite phase. The resistivity is generally smaller in the austenite than in the martensite phase and hence the MFIA leads to a negative MR .

During the MT both phases coexist over a certain temperature interval. At the interfaces between the phases, additional scattering occurs due to spin transport between areas with different magnetizations [86, 87]. An applied field reduces the difference between the magnetization of the phases and hence a negative *MR* results. This effect is expected to be maximal, when both phases have equal fractions; here the maximal number of interfaces is expected.

Experimental Results

The magnetoresistance of both sample series is discussed in the following. At each temperature point the magnetoresistance is measured up to 1 T including the virgin curve. Selected examples of the *MR* loops are shown in Figure 5.24 (a) for the 200 nm and (b) 50 nm thin film of SERIES A. The most striking effect is the irreversible negative *MR* during the virgin loop of the 200 nm (50 nm) thick sample at 273 K (243 K) during the martensite - austenite transition. The amplitude of the irreversible *MR* of the 50 nm sample is lower and also shifted to lower temperatures compared to the 200 nm thin film. For measurements during the austenite-martensite transition, a positive irreversible *MR* is visible. This is shown for the 50 nm sample at 223 K. All measurements show a negative reversible *MR* of different amplitude. At -1 T, a gap between the virgin curve and the field loop is visible. This is due to an overdrive of the magnet. After the measurement at 1 T is recorded, the field increases by about 0.02 T before it ramps back to 1 T and the measurement continues with the loop.

The magnetoresistance is analyzed in terms of reversible and irreversible *MR*. At first, the amplitude of the reversible *MR* (*RMR*) in dependence of the temperature is analyzed for selected samples. The irreversible *MR* (*IMR*) is discussed later in this section.

In Figure 5.24 (c) -(g) *RMR* at 1T for samples of both series is shown. All samples of SERIES A show two maxima of the *RMR* during the forward and reverse transformation. The first maximum is located close to T_c^A and can be attributed to a reduced spin flip scattering due to an applied magnetic field.[75] The amplitude of the *RMR* at T_c^A depends on the film thickness and reduces continuously from 0.9 % for the 200 nm sample to 0.58 % for the 20 nm sample. The second maximum can be attributed to the martensitic transformation. For thick films with a small transformation range, a clear peak and a shift of the maximum is observable leading to a hysteresis. The *RMR*

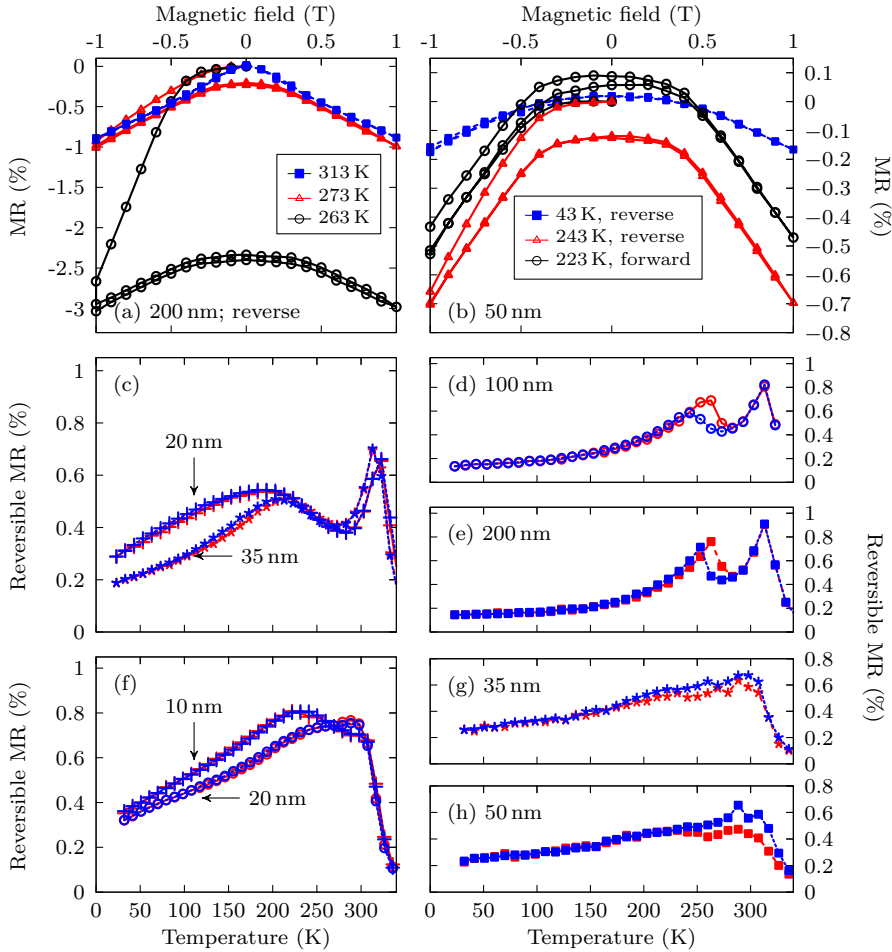


Figure 5.24: The magnetoresistance (MR) for selected samples in dependence of the magnetic field is shown in (a) and (b) for the forward and reverse transition at selected temperatures. The reversible MR at 1 T is plotted for selected samples in (c) to (e) for SERIES A and in (f) - (h) for SERIES B. In (c) - (h) the blue/red color marks cooling/heating, respectively.

of the transformation is maximal for the 200 nm film. With decreasing film thickness the *RMR* decreases and the hysteresis widens. At 20 nm thickness the *MR* of the MT increases slightly again. The samples thicker than 20 nm of SERIES B do not show pronounced peaks since these films are in the martensite phase at T_c^A , but a clear hysteresis is visible. For thinner films the peak at T_c^A emerges. The transformation peaks become very pronounced for the 10 nm sample and are even larger than the spin flip scattering peak; for all other samples the latter peak is larger than the transformation *RMR* one. At low temperatures, a linear or quadratic kind of decrease in the *RMR* is visible.

For a better overview about the *RMR* in dependence of the transformation and magnetization, all relevant measurements are plotted normalized in Figure 5.25. The maxima of the transformation *RMR* are midway in the steepest part of the forward and reverse transformation, respectively, if the transition is below T_c^A . For all films of SERIES A, the *RMR* curves of the heating and cooling branches intercept in the hysteresis range. Below this interception, the cooling branch shows higher *RMR* than the heating branch, above the relation inverts. The same behavior is also visible for the films of SERIES B, where the transformation has just started around T_c^A (10 nm and 20 nm). For thicker films, only the second part of hysteresis is visible, where the forward *RMR* is larger than the reverse one.

The irreversible *MR* (*IMR*) is plotted in Figure 5.26 in relation to the reversible *MR* and resistivity. At temperatures above the transition, the *IMR* is close to zero for all samples. On further cooling the *IMR* becomes maximal around the same temperature as the *RMR*, where the transition shows the steepest increase. Note that the *IMR* is always positive on the cooling branch. On the heating branch the *IMR* has a negative amplitude like the *RMR*. For the 200 nm film a small offset is visible between the maxima of the *IMR* and *RMR*, which is most likely caused by a too low measurement resolution for this film: the maximum of *RMR* and *IMR* would be directly between 260 K and 270 K, where the steepest part of the transformation is visible as well.

Discussion

The origin of *IMR* can be understood in terms of the MFIA. In Figure 5.27 a sketch of the potentials during the MT on the cooling and heating branch of the hysteresis is shown. During cooling, an undercooling effect can be observed

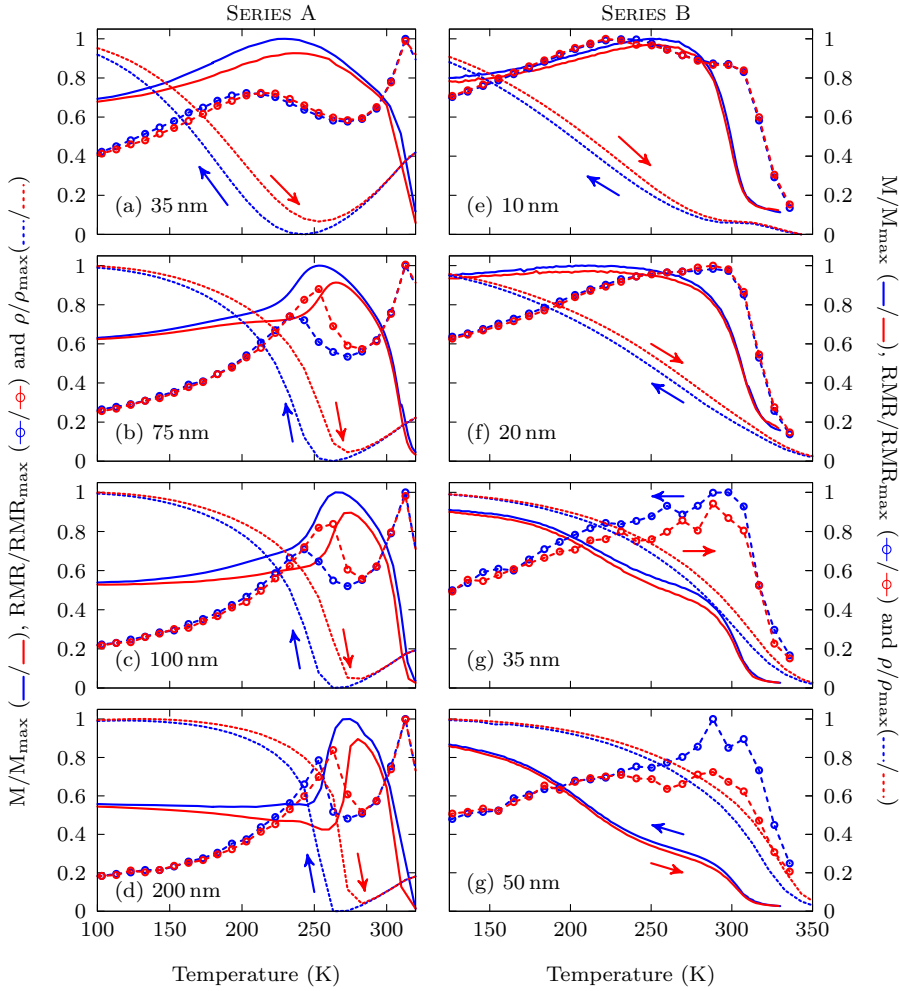


Figure 5.25: The reversible magnetoresistance for selected thin films of SERIES A and SERIES B in dependence of temperature. The magnetization and resistivity is plotted for orientation. All values are normalized. The arrows indicate the temperature change direction.

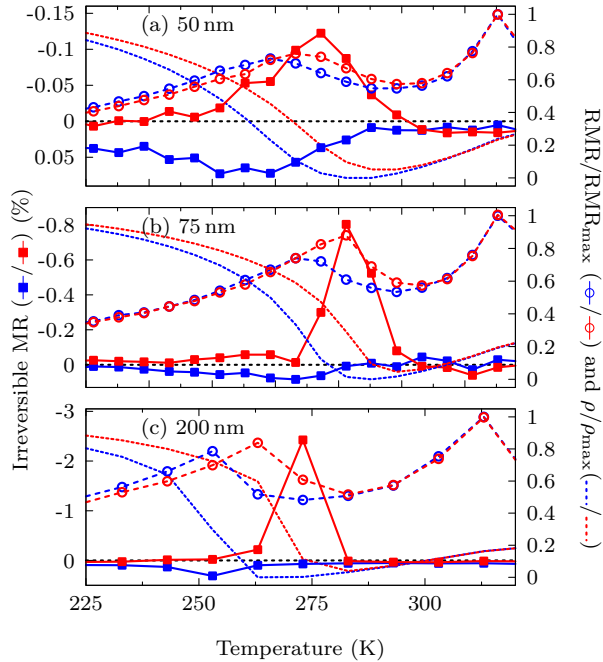


Figure 5.26: The temperature dependence of the irreversible magnetoresistance is presented for selected thin films of SERIES A. The normalized reversible MR and resistivity is plotted for orientation. The blue/red color marks cooling/heating, respectively.

leading to a metastable fraction of austenite. The reverse happens during heating: overheating is present and a metastable fraction of martensite exists. If a magnetic field is applied, the potential of the martensite is raised in energy. The energy barrier to transform to austenite is very low, allowing to transform a large fraction of martensite. When the magnetic field is removed and the potential is in its initial state, the transformation from the austenite back to the martensite is less likely because the energy barrier is much higher. Thus on the heating branch the large negative *IMR* due to MFIA is the dominant contribution. On the cooling branch a positive *IMR* has been observed. Here the applied magnetic field also lowers the potential of the austenitic phase

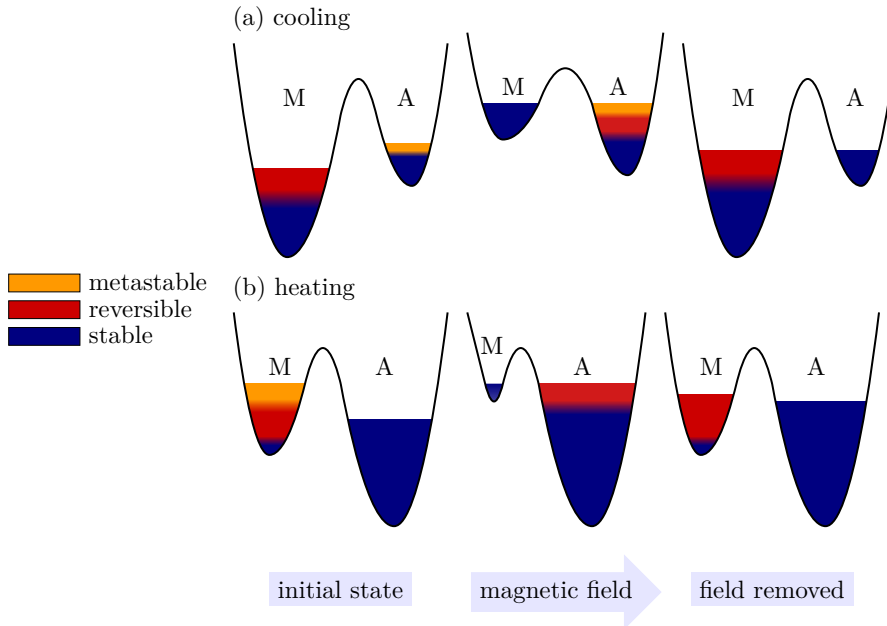


Figure 5.27: The potentials of the Martensite (M) and Austenite (A) phase during the forward ((a), cooling) and reverse ((b), heating) transition are sketched. The magnetic field favors the austenite phase.

leading to a larger fraction of austenite. This effect is in terms of the here assumed Gibbs energy reversible. However, due to the perturbing influence of the magnetic field on the metastable austenite, a transformation of the latter to martensite is possible. This could explain the positive and also comparably small *IMR* on the cooling branch. A positive and a negative *IMR* has also been observed by Wang *et al.* [88] for bulk $\text{Ni}_{49.5}\text{Mn}_{34.5}\text{In}_{16}$ with an applied field of up to 6 T. A magnetic memory effect caused by prior measurements is unlikely, because close to T_c^A larger *IMR* effects should be visible then.

The contributions of the MT to the *RMR* cannot be clearly separated. In the temperature region with the largest transformation rate, interface effects as well as MFIA can have influence on the MT. The *RMR* is larger during the reverse transition which indicates MFIA: due to overheating of the martensite

the reversible transformation of martensite to austenite should be enhanced leading to the larger *RMR*. The position of the maximum of the *RMR* caused by MFIA should be in the steepest part of the transition. Energetically, temperature and magnetic field have an influence on the transition.(see eq. 5.9). Thus, where a small temperature difference is needed for a large part of the transition, a magnetic field has maximal influence. Interface contributions should lead to the same amplitude during forward and reverse transformation. This temperature is probably in the vicinity of the highest transformation rate as well. Thus, a combination of both effects is likely. In this temperature region the *RMR* does not correlate with the magnetization. With decreasing temperature, where the transformation rate is very low, the *RMR* correlates with the magnetization as described by eq. 5.8. In the low temperature region, the *RMR* shows different behavior depending on the temperature where the martensite is stable (M_f). The thin films with a low M_f temperature show a linear dependence of the *MR* with temperature; this can be understood in terms of the linear dependence of the transition over most of the temperature range and thus a linear decrease of the *MR* can also be expected. The films, where most of the transition is finished at lower temperatures, show a typical behavior of electron-magnon scattering.[85]

The thickness dependence of the *MR* can be understood as follows: The magnetic field and the temperature have the same energy scaling as can be seen in eq. 5.9. In other words, if a large temperature difference is required to finish the transformation, a high field is also needed to achieve the transition. Hence, the MFIA which is responsible for the *IMR* (and partly also for the *RMR*) decreases significantly for thinner films. For thinner films, an increase of the *RMR* is visible which is very pronounced for the 10 nm thin film. The interfaces to the MgO could lead to additional scattering effects. Furthermore, for the thinner films a lower twinning periodicity is expected.[46] This leads to more interfaces and thus a higher scattering probability is likely.

6 Summary and Conclusions

In this work the martensitic transformation of thin films on a rigid substrate has been studied both theoretically and experimentally. The film thickness has been varied to gain insight into the importance of the rigid substrate and other possible constraints.

At first, phase field simulations have been conducted to understand the influence of the rigid substrate on the transformation behavior. The model of Levitas *et al.* [33, 34] is employed to predict the microstructure of a two variant system of NiAl; this serves here as a model system to predict the *c/a* twinning behavior in thin films. *c/a* twinning is also observed in the martensitic structure of Ni-Mn-Sn which is investigated experimentally. The transformation is finished after 0.4 ns which is in good agreement with the literature. An emphasis has been laid on the energetic contributions and the microstructure. The fraction of variants can be predicted by the crystallographic theory. At the beginning of the austenite to martensite transformation it deviates from the theoretical value. For low temperatures where the transformation is finished a good agreement has been found. The twinning periodicity predicted by this model is also in good agreement with a special case of the universal Landau-Lifshitz-Kittel scaling law. This law predicts an increase of the twinning periodicity with increasing film thickness. The transformation slope itself gets gentler with decreasing film thickness. The reason is a layer at the substrate that needs additional chemical energy (undercooling) to transform.

For the experimental investigation, the ferromagnetic shape memory alloy Ni-Mn-Sn has been chosen as a model system. It has a low misfit to the MgO substrate and hence is an ideal candidate for these investigation: A low misfit leads to more comparable thin film quality and less macro stress in the films.

6. SUMMARY AND CONCLUSIONS

The effect of macro stress on the martensitic transformation is well understood and hence has not been the focus of this investigation. The Ni-Mn-Sn thin films were epitaxially grown on a MgO substrate in a thickness range of 10 nm up to 200 nm. Two different compositions have been chosen with $\text{Ni}_{51.6}\text{Mn}_{32.9}\text{Sn}_{15.5}$ (SERIES A) and $\text{Ni}_{51.6}\text{Mn}_{34.9}\text{Sn}_{13.5}$ (SERIES B). SERIES A is in the austenite state at room temperatures and shows the martensitic transformation at 260 K. SERIES B is in the martensitic state at room temperature with a transition temperature of 350 K. The properties of the thin films have been investigated by X-ray diffraction, electric transport, and magnetic measurements.

The thin film quality has been investigated by X-ray diffraction of the thin films in the austenite state. The grain structure of the films is most likely columnar and has a low mosaicity. Towards thinner films, a higher degree of mosaicity and some tetragonal distortion has been found due to the small misfit between substrate and thin film. SERIES A has a larger misfit between substrate and thin film than SERIES B. Thus, close to the substrate / thin film interface SERIES A shows a higher degree of dislocation density and grain misorientation compared to SERIES B. A small contamination probably due to grain boundary segregation of NiMn is also present.

The analysis of the martensitic structure of SERIES B has shown that at room temperature an orthorhombic phase and modulated structures (4O, 10M) are present. The structural transition has been observed by temperature dependent X-ray diffraction measurements.

The magnetic and electric transport measurements show a clear dependence on the martensitic transformation. The magnetic moment decreases during the transition and the resistivity increases. For SERIES A, a good agreement between both measurements for the martensitic transformation behavior has been found. The martensitic transformation of SERIES B cannot be observed by magnetic measurements, because the austenite and martensite Curie temperature are below the transition temperature. However, this offers the possibility to investigate the thickness dependence of the martensitic Curie temperature, which increases with decreasing film thickness. This is probably caused by an increase of the austenite fraction in the relevant temperature regime.

Generally, the magnetic and electric transport properties of the thickest films correspond well to available bulk data.

The theoretically predicted suppression of the transformation at the interface is visible in the magnetic and electric transport measurements. The

maximal resistivity change due to the martensitic transformation has been used to calculate the thickness of the austenite layer. The degree of residual austenite in samples of SERIES A is larger than in SERIES B's.

The two sample series do not only differ in the austenite layer thickness, but also the transformation behavior changes. Generally, a shift of the transition to lower temperatures and an increase of the transition range with decreasing film thickness has been found. This can mainly be attributed to the influence of the rigid substrate. Additionally, size scale effects and confinement of the nucleus as proposed by Malygin [6] can change the transformation behavior. However, the effects predicted by this model fit only qualitatively. Effects such as additional energy terms due to interphase/grain boundaries and strain energies as proposed by Meng *et al.* [19] can also lead to reduced transition temperatures.

The critical thickness, where the transformation is suppressed, and the hysteresis of SERIES B are smaller than SERIES A's. Both, the sample quality close to the substrate/thin film interface and the phase compatibility, are better for SERIES B compared to SERIES A. As a common cause for the differences in the hysteresis size, the critical thickness and the residual austenite fraction, the different phase compatibility and sample quality are the most likely candidates.

The magnetoresistance combines resistivity, magnetism and transformation characteristics. It can be caused by magnetic field induced austenite (MFIA) or magnetic scattering effects. Irreversible and reversible magnetoresistance (*RMR*) has been found. The irreversible magnetoresistance (*IMR*) is explained in terms of over- or undercooling and the resulting different energy barriers for the forward/reverse transformation during MFIA. Since the influence of the magnetic field and the temperature are correlated, the largest *IMR* and also *RMR* has been found for the thickest films, where the transformation is steepest. In regions where the magnetoresistance is most likely dominated by magnetic scattering it mirrors the magnetic behavior.

To conclude, the influence of the film thickness has been investigated using phase field simulations and Ni-Mn-Sn thin films grown on MgO. The rigid substrate has a huge influence on the transformation behavior. Important parameters that influence the functionality in thin films seem to be the phase compatibility and sample quality.

7 Outlook

In the future the focus will be on the inverse magnetocaloric effect in thin films. Due to the magnetic field induced reverse transition, the isothermal application of a magnetic field leads to an increased entropy [2]. Hence, an adiabatic field induced reverse transition cools the material by an amount ΔT . In order to maximize ΔT , multilayer structures of different shape memory Heusler alloys will be prepared and investigated. An increased ΔT is expected due to a high interface entropy. One important aspect for the efficiency of the Heusler alloys is the phase compatibility. As has been shown in this work, the phase compatibility has influence on the hysteresis and the residual austenite at the interfaces. Thus the details of the martensitic structure are important. Hence, low temperature XRD measurements will be conducted to gain insight into the structural transition. Furthermore, the kind of martensite to martensite transition indicated by the magnetization measurements of SERIES A can be analyzed.

Bibliography

- [1] A. Sozinov, A. A. Likhachev, N. Lanska, and K. Ullakko, "Giant magnetic-field-induced strain in NiMnGa seven-layered martensitic phase," *Applied Physics Letters*, vol. 80, no. 10, pp. 1746–1748, 2002. [Online]. Available: <http://link.aip.org/link/?APL/80/1746/1>
- [2] P. J. Shamberger and F. S. Ohuchi, "Hysteresis of the martensitic phase transition in magnetocaloric-effect Ni-Mn-Sn alloys," *Phys. Rev. B*, vol. 79, p. 144407, Apr 2009. [Online]. Available: <http://link.aps.org/doi/10.1103/PhysRevB.79.144407>
- [3] S. Y. Yu, Z. H. Liu, G. D. Liu, J. L. Chen, Z. X. Cao, G. H. Wu, B. Zhang, and X. X. Zhang, "Large magnetoresistance in single-crystalline Ni₅₀Mn_{50-x}In_x alloys (x = 14–16) upon martensitic transformation," *Applied Physics Letters*, vol. 89, no. 16, p. 162503, 2006. [Online]. Available: <http://link.aip.org/link/?APL/89/162503/1>
- [4] B. Winzek, S. Schmitz, H. Rumpf, T. Sterzl, R. Hassdorf, S. Thienhaus, J. Feydt, M. Moske, and E. Quandt, "Recent developments in shape memory thin film technology," *Materials Science and Engineering: A*, vol. 378, no. 1–2, pp. 40 – 46, 2004, ;ce:title;European Symposium on Martensitic Transformation and Shape-Memory; /ce:title;. [Online]. Available: <http://www.sciencedirect.com/science/article/pii/S0921509303015168>
- [5] D. C. Dunand and P. Müllner, "Size Effects on Magnetic Actuation in Ni-Mn-Ga Shape-Memory Alloys," *Advanced Materials*, vol. 23, no. 2, pp. 216–232, 2011. [Online]. Available: <http://dx.doi.org/10.1002/adma.201002753>

- [6] G. Malygin, "Size effects under martensitic deformation of shape-memory alloys," *Technical Physics*, vol. 54, pp. 1782–1785, 2009, 10.1134/S106378420912010X. [Online]. Available: <http://dx.doi.org/10.1134/S106378420912010X>
- [7] A. Roytburd, T. Kim, Q. Su, J. Slutsker, and M. Wuttig, "Martensitic transformation in constrained films," *Acta Materialia*, vol. 46, no. 14, pp. 5095 – 5107, 1998. [Online]. Available: <http://www.sciencedirect.com/science/article/pii/S1359645498001657>
- [8] K. Bhattacharya, *Microstructure of Martensite*. Oxford: Oxford University Press, 2003.
- [9] S. Kaufmann, R. Niemann, T. Thersleff, U. K. Rösler, O. Heczko, J. Buschbeck, B. Holzapfel, L. Schultz, and S. Fähler, "Modulated martensite: why it forms and why it deforms easily," *New Journal of Physics*, vol. 13, no. 5, p. 053029, 2011. [Online]. Available: <http://stacks.iop.org/1367-2630/13/i=5/a=053029>
- [10] R. Vishnoi, R. Singhal, and D. Kaur, "Thickness dependent phase transformation of magnetron-sputtered Ni–Mn–Sn ferromagnetic shape memory alloy thin films," *Journal of Nanoparticle Research*, vol. 13, pp. 3975–3990, 2011, 10.1007/s11051-011-0321-3. [Online]. Available: <http://dx.doi.org/10.1007/s11051-011-0321-3>
- [11] V. Recarte, J. I. Pérez-Landazábal, V. Sánchez-Alárcos, V. A. Chernenko, and M. Ohtsuka, "Magnetocaloric effect linked to the martensitic transformation in sputter-deposited Ni–Mn–Ga thin films," *Applied Physics Letters*, vol. 95, no. 14, p. 141908, 2009. [Online]. Available: <http://link.aip.org/link/?APL/95/141908/1>
- [12] R. Vishnoi and D. Kaur, "Size dependence of martensite transformation temperature in nanostructured Ni–Mn–Sn ferromagnetic shape memory alloy thin films," *Surface and Coatings Technology*, vol. 204, no. 23, pp. 3773 – 3782, 2010. [Online]. Available: <http://www.sciencedirect.com/science/article/pii/S0257897210003208>
- [13] R. Niemann, O. Heczko, L. Schultz, and S. Fähler, "Metamagnetic transitions and magnetocaloric effect in epitaxial Ni–Co–Mn–In films,"

- Applied Physics Letters*, vol. 97, no. 22, p. 222507, 2010. [Online]. Available: <http://link.aip.org/link/?APL/97/222507/1>
- [14] K. Załęski, J. Dubowik, I. Gościańska, B. Andrzejewski, and T. Toliński, "Magnetostructural transformations in Ni₅₁Mn₃₆Sn₁₃ Heusler alloy thin films," *Central European Journal of Physics*, vol. 9, pp. 558–561, 2011, 10.2478/s11534-011-0004-9. [Online]. Available: <http://dx.doi.org/10.2478/s11534-011-0004-9>
- [15] T. Krenke, M. Acet, E. F. Wassermann, X. Moya, L. Mañosa, and A. Planes, "Martensitic transitions and the nature of ferromagnetism in the austenitic and martensitic states of Ni – Mn – Sn alloys," *Phys. Rev. B*, vol. 72, p. 014412, Jul 2005. [Online]. Available: <http://link.aps.org/doi/10.1103/PhysRevB.72.014412>
- [16] M. H. Sadd, *Elasticity: Theory, Applications, Numerics*. Oxford: ELSEVIER SCIENCE Ltd, 2009.
- [17] J. W. Christian, *The Theory of Transformations in Metals and Alloys*. Oxford: ELSEVIER SCIENCE Ltd, 2002.
- [18] M. T. Dove, *Structure and Dynamics: An atomic view of materials*. Great Clarendon Street, Oxford: Oxford University Press, 2003.
- [19] Q. Meng, Y. Rong, and T. Y. Hsu, "Nucleation barrier for phase transformations in nanosized crystals," *Phys. Rev. B*, vol. 65, p. 174118, May 2002. [Online]. Available: <http://link.aps.org/doi/10.1103/PhysRevB.65.174118>
- [20] Z. Zhang, R. D. James, and S. Müller, "Energy barriers and hysteresis in martensitic phase transformations," *Acta Materialia*, vol. 57, no. 15, pp. 4332 – 4352, 2009. [Online]. Available: <http://www.sciencedirect.com/science/article/pii/S135964540900336X>
- [21] J. Cui, Y. S. Chu, O. O. Famodu, Y. Furuya, J. Hattrick-Simpers, R. D. James, A. Ludwig, S. Thienhaus, M. Wuttig, Z. Zhang, and I. Takeuchi, "Combinatorial search of thermoelastic shape-memory alloys with extremely small hysteresis width," *Nat Mater*, vol. 5, pp. 286–290, 2006. [Online]. Available: <http://dx.doi.org/10.1038/nmat1593>

- [22] J. M. Ball and R. D. James, "Proposed experimental tests of a theory of fine microstructure and the two-well problem," *Philosophical Transactions: Physical Sciences and Engineering*, vol. 338, no. 1650, pp. pp. 389–450, 1992. [Online]. Available: <http://www.jstor.org/stable/53973>
- [23] G. Malygin, "Heterogeneous nucleation of martensite at dislocations and the martensitic-transformation kinetics in shape memory alloys," *Physics of the Solid State*, vol. 45, pp. 345–351, 2003, 10.1134/1.1553542. [Online]. Available: <http://dx.doi.org/10.1134/1.1553542>
- [24] G. Malygin, "Heterogeneous nucleation of martensite on precipitates and the martensitic-transformation kinetics in shape memory alloys," *Physics of the Solid State*, vol. 45, pp. 1566–1571, 2003, 10.1134/1.1602897. [Online]. Available: <http://dx.doi.org/10.1134/1.1602897>
- [25] A. Potekaev, A. Klopotov, V. Kulagina, and V. Gyunter, "Influence of structural defects on the structural-phase transformations in relatively unstable states of functional materials," *Steel in Translation*, vol. 40, pp. 881–887, 2010, 10.3103/S0967091210100050. [Online]. Available: <http://dx.doi.org/10.3103/S0967091210100050>
- [26] B. Li, X. M. Zhang, P. C. Clapp, and J. A. Rifkin, "Molecular dynamics simulations of the effects of defects on martensite nucleation," *Journal of Applied Physics*, vol. 95, no. 4, pp. 1698–1705, 2004. [Online]. Available: <http://link.aip.org/link/?JAP/95/1698/1>
- [27] G. A. Malygin, "Diffuse martensitic transitions and the plasticity of crystals with a shape memory effect," *Physics-Uspokhi*, vol. 44, no. 2, p. 173, 2001. [Online]. Available: <http://stacks.iop.org/1063-7869/44/i=2/a=R03>
- [28] G. Malygin, "Nanosopic size effects on martensitic transformations in shape memory alloys," *Physics of the Solid State*, vol. 50, pp. 1538–1543, 2008, 10.1134/S1063783408080258. [Online]. Available: <http://dx.doi.org/10.1134/S1063783408080258>
- [29] BESTEC, BERLIN.
- [30] B. D. Cullity and S. R. Stock, *Elements of X-ray diffraction*. Upper Saddle River, NJ: Prentice Hall, 2001.

-
- [31] H. Ebel, *X-Ray Spectrom.*, vol. 28, p. 255, (1999).
- [32] N. Teichert, "Magnetic shape memory alloys in thin films," Master's thesis, Universität Bielefeld, 2012.
- [33] V. I. Levitas and D. L. Preston, "Three-dimensional Landau theory for multivariant stress-induced martensitic phase transformations. I. Austenite \leftrightarrow martensite," *Phys. Rev. B*, vol. 66, p. 134206, Oct 2002. [Online]. Available: <http://link.aps.org/doi/10.1103/PhysRevB.66.134206>
- [34] V. I. Levitas and D. L. Preston, "Three-dimensional Landau theory for multivariant stress-induced martensitic phase transformations. II. Multivariant phase transformations and stress space analysis," *Phys. Rev. B*, vol. 66, p. 134207, Oct 2002. [Online]. Available: <http://link.aps.org/doi/10.1103/PhysRevB.66.134207>
- [35] N. S. Ottosen and H. Petersson, *Introduction to the Finite Element Method*. Prentice Hall, 1992.
- [36] J. S. Langer, M. Bar-on, and H. D. Miller, "New computational method in the theory of spinodal decomposition," *Phys. Rev. A*, vol. 11, pp. 1417–1429, Apr 1975. [Online]. Available: <http://link.aps.org/doi/10.1103/PhysRevA.11.1417>
- [37] J. W. Cahn, "Spinodal decomposition," *Acta Metall.*, vol. 9, p. 795–801, 1961.
- [38] Cahn, J. W. and Allen, S. M., "A microscopic theory for domain wall motion and its experimental verification in fe-al alloy domain growth kinetics," *J. Phys. Colloques*, vol. 38, pp. C7–51–C7–54, 1977. [Online]. Available: <http://dx.doi.org/10.1051/jphyscol:1977709>
- [39] H. Emmerich, "Phase-field modelling for metals and colloids and nucleation therein—an overview," *Journal of Physics: Condensed Matter*, vol. 21, no. 46, p. 464103, 2009. [Online]. Available: <http://stacks.iop.org/0953-8984/21/i=46/a=464103>
- [40] L.-Q. Chen, "Phase-field models for microstructure evolution," *Annual Review of Materials Research*, vol. 32, no. 1, pp. 113–140, 2002. [Online].

Available: <http://www.annualreviews.org/doi/abs/10.1146/annurev.matsci.32.112001.132041>

- [41] J. Y. Cho, "Finite element modeling of martensitic phase transformations," Ph.D. dissertation, Texas Tech University, 2009.
- [42] Y. Shapira, *MATRIX-BASED MULTIGRID: Theory and Applications*. Spring Street, New York: Springer, 2008.
- [43] O. Schenk and K. Gärtner, "Solving unsymmetric sparse systems of linear equations with PARDISO," *Future Generation Computer Systems*, vol. 20, no. 3, pp. 475 – 487, 2004, [; Selected numerical algorithms; \[Online\]. Available: http://www.sciencedirect.com/science/article/pii/S0167739X03001882](http://www.sciencedirect.com/science/article/pii/S0167739X03001882)
- [44] I. M. Robertson and C. M. Wayman, "Tweed microstructures II. In several phases of the Ni-Al system," *Philosophical Magazine A*, vol. 48, no. 3, pp. 443–467, 1983. [Online]. Available: <http://www.tandfonline.com/doi/abs/10.1080/01418618308234903>
- [45] A. V. Idesman, J.-Y. Cho, and V. I. Levitas, "Finite element modeling of dynamics of martensitic phase transitions," *Applied Physics Letters*, vol. 93, no. 4, p. 043102, 2008. [Online]. Available: <http://link.aip.org/link/?APL/93/043102/1>
- [46] A. Diestel, A. Backen, U. K. R. Iler, L. Schultz, and S. Fähler, "Twin boundary energy of hierarchically twinned magnetic shape memory alloys," *Applied Physics Letters*, vol. 99, no. 9, p. 092512, 2011. [Online]. Available: <http://link.aip.org/link/?APL/99/092512/1>
- [47] L. Landau and E. Lifshits, "On the theory of the dispersion of magnetic permeability in ferromagnetic bodies," *Phys. Z. Sowjetunion*, vol. 8, p. 153–169, 1935.
- [48] C. Kittel, "Theory of the structure of ferromagnetic domains in films and small particles," *Phys. Rev.*, vol. 70, pp. 965–971, Dec 1946. [Online]. Available: <http://link.aps.org/doi/10.1103/PhysRev.70.965>
- [49] Naval Research Laboratory, "Crystal lattice structures," Oct. 2008. [Online]. Available: <http://cst-www.nrl.navy.mil/lattice/>

- [50] A. Planes, L. Mañosa, and M. Acet, "Magnetocaloric effect and its relation to shape-memory properties in ferromagnetic heusler alloys," *Journal of Physics: Condensed Matter*, vol. 21, no. 23, p. 233201, 2009. [Online]. Available: <http://stacks.iop.org/0953-8984/21/i=23/a=233201>
- [51] M. Birkholz, *Thin Film Analysis by X-Ray Scattering: Techniques for Structural Characterization*. Weinheim: Wiley-VCH Verlag GmbH & Co. KGaA, 2006.
- [52] P. Webster, "Magnetic and chemical order in heusler alloys containing cobalt and manganese," *Journal of Physics and Chemistry of Solids*, vol. 32, no. 6, pp. 1221 – 1231, 1971. [Online]. Available: <http://www.sciencedirect.com/science/article/pii/S0022369771801804>
- [53] M. Huang, "Kinetic study on the phase transformations in sputter deposited NiMn thin films," *Journal of Applied Physics*, vol. 97, no. 6, p. 064906, 2005. [Online]. Available: <http://link.aip.org/link/?JAP/97/064906/1>
- [54] M. Ohring, *Materials Science of Thin Films*. Elsevier Science, 2001. [Online]. Available: <http://books.google.de/books?id=m3fai5hbc94C>
- [55] M. Meinert, J.-M. Schmalhorst, G. Reiss, and E. Arenholz, "Ferrimagnetism and disorder of epitaxial $\text{mn}_{2-x}\text{co}_x$ val heusler compound thin films," *Journal of Physics D: Applied Physics*, vol. 44, no. 21, p. 215003, 2011. [Online]. Available: <http://stacks.iop.org/0022-3727/44/i=21/a=215003>
- [56] M. D. Biegalski, D. D. Fong, J. A. Eastman, P. H. Fuoss, S. K. Streiffer, T. Heeg, J. Schubert, W. Tian, C. T. Nelson, X. Q. Pan, M. E. Hawley, M. Bernhagen, P. Reiche, R. Uecker, S. Trolier-McKinstry, and D. G. Schlom, "Critical thickness of high structural quality SrTiO_3 films grown on orthorhombic (101) DyScO [sub 3]," *Journal of Applied Physics*, vol. 104, no. 11, p. 114109, 2008. [Online]. Available: <http://link.aip.org/link/?JAP/104/114109/1>
- [57] F. Martin, P. Muralt, M.-A. Dubois, and A. Pezous, "Thickness dependence of the properties of highly c-axis textured AlN thin films," *Journal of Vacuum Science & Technology A: Vacuum, Surfaces, and Films*, vol. 22, no. 2, pp. 361–365, 2004. [Online]. Available: <http://link.aip.org/link/?JVA/22/361/1>

- [58] R. Tilley, *Crystals And Crystal Structures*. John Wiley, 2006. [Online]. Available: <http://books.google.de/books?id=ilVvOYOFcX8C>
- [59] K. Otsuka, T. Ohba, M. Tokonami, and C. Wayman, "New description of long period stacking order structures of martensites in β -phase alloys," *Scripta Metallurgica et Materialia*, vol. 29, no. 10, pp. 1359 – 1364, 1993. [Online]. Available: <http://www.sciencedirect.com/science/article/pii/S0956716X9390139J>
- [60] J. Pons, R. Santamarta, V. A. Chernenko, and E. Cesari, "Long-period martensitic structures of Ni-Mn-Ga alloys studied by high-resolution transmission electron microscopy," *Journal of Applied Physics*, vol. 97, no. 8, p. 083516, 2005. [Online]. Available: <http://link.aip.org/link/?JAP/97/083516/1>
- [61] A. G. Khachatryan, S. M. Shapiro, and S. Semenovskaya, "Adaptive phase formation in martensitic transformation," *Phys. Rev. B*, vol. 43, pp. 10 832–10 843, May 1991. [Online]. Available: <http://link.aps.org/doi/10.1103/PhysRevB.43.10832>
- [62] Y. Sutou, Y. Imano, N. Koeda, T. Omori, R. Kainuma, K. Ishida, and K. Oikawa, "Magnetic and martensitic transformations of NiMnX(X = In,Sn,Sb) ferromagnetic shape memory alloys," *Applied Physics Letters*, vol. 85, no. 19, pp. 4358–4360, 2004. [Online]. Available: <http://link.aip.org/link/?APL/85/4358/1>
- [63] P. J. Brown, A. P. Gandy, K. Ishida, R. Kainuma, T. Kanomata, K.-U. Neumann, K. Oikawa, B. Ouladdiaf, and K. R. A. Ziebeck, "The magnetic and structural properties of the magnetic shape memory compound Ni₂Mn_{1.44}Sn_{0.56}," *Journal of Physics: Condensed Matter*, vol. 18, no. 7, p. 2249, 2006. [Online]. Available: <http://stacks.iop.org/0953-8984/18/i=7/a=012>
- [64] V. A. Chernenko and J. M. Barandiaran, "Incommensurate and Commensurate Structural Modulation in Martensitic Phases of FSMA," *Materials Science Forum*, vol. 635, pp. 33–41, 2010. [Online]. Available: <http://www.scientific.net/MSF.635.33>
- [65] M. Thomas, O. Heczko, J. Buschbeck, U. K. Rösler, J. McCord, N. Scheerbaum, L. Schultz, and S. Fähler, "Magnetically induced

- reorientation of martensite variants in constrained epitaxial Ni–Mn–Ga films grown on MgO(001),” *New Journal of Physics*, vol. 10, no. 2, p. 023040, 2008. [Online]. Available: <http://stacks.iop.org/1367-2630/10/i=2/a=023040>
- [66] Y. Yamada, Y. Noda, and M. Takimoto, “‘modulated lattice relaxation’ in β -based premartensitic phase,” *Solid State Communications*, vol. 55, no. 11, pp. 1003 – 1006, 1985. [Online]. Available: <http://www.sciencedirect.com/science/article/pii/0038109885905769>
- [67] S. ğduk and G. Gökođlu, “Ab initio lattice dynamics of Ni₂MnX (X=Sn, Sb) magnetic shape memory alloys,” *Journal of Alloys and Compounds*, vol. 511, no. 1, pp. 9 – 13, 2012. [Online]. Available: <http://www.sciencedirect.com/science/article/pii/S0925838811017798>
- [68] V. D. Buchelnikov, V. V. Sokolovskiy, S. V. Taskaev, V. V. Khovaylo, A. A. Aliev, L. N. Khanov, A. B. Batdalov, P. Entel, H. Miki, and T. Takagi, “Monte Carlo simulations of the magnetocaloric effect in magnetic Ni–Mn–X (X = Ga, In) Heusler alloys,” *Journal of Physics D: Applied Physics*, vol. 44, no. 6, p. 064012, 2011. [Online]. Available: <http://stacks.iop.org/0022-3727/44/i=6/a=064012>
- [69] V. D. Buchelnikov, P. Entel, S. V. Taskaev, V. V. Sokolovskiy, A. Hucht, M. Ogura, H. Akai, M. E. Gruner, and S. K. Nayak, “Monte carlo study of the influence of antiferromagnetic exchange interactions on the phase transitions of ferromagnetic Ni-Mn-x alloys (x = In, Sn, Sb),” *Phys. Rev. B*, vol. 78, p. 184427, Nov 2008. [Online]. Available: <http://link.aps.org/doi/10.1103/PhysRevB.78.184427>
- [70] J. Dubowik, Y. V. Kudryavtsev, and Y. P. Lee, “Martensitic transformation in Ni₂MnGa films: A ferromagnetic resonance study,” *Journal of Applied Physics*, vol. 95, no. 5, pp. 2912–2917, 2004. [Online]. Available: <http://link.aip.org/link/?JAP/95/2912/1>
- [71] O. Heczko, S. Fähler, T. M. Vasilchikova, T. N. Voloshok, K. V. Klimov, Y. I. Chumlyakov, and A. N. Vasiliev, “Thermodynamic, kinetic, and magnetic properties of a Ni₅₄Fe₁₉Ga₂₇ magnetic shape-memory single crystal,” *Phys. Rev. B*, vol. 77, p. 174402, May 2008. [Online]. Available: <http://link.aps.org/doi/10.1103/PhysRevB.77.174402>

- [72] V. N. Antonov, A. Y. Perlov, P. M. Oppeneer, A. N. Yaresko, and S. V. Halilov, "Mechanism of the Giant Magnetoresistance in UNiGa from First-Principles Calculations," *Phys. Rev. Lett.*, vol. 77, pp. 5253–5256, Dec 1996. [Online]. Available: <http://link.aps.org/doi/10.1103/PhysRevLett.77.5253>
- [73] B. Zhang, X. X. Zhang, S. Y. Yu, J. L. Chen, Z. X. Cao, and G. H. Wu, "Giant magnetothermal conductivity in the Ni–Mn–In ferromagnetic shape memory alloys," *Applied Physics Letters*, vol. 91, no. 1, p. 012510, 2007. [Online]. Available: <http://link.aip.org/link/?APL/91/012510/1>
- [74] M. Ye, A. Kimura, Y. Miura, M. Shirai, Y. T. Cui, K. Shimada, H. Namatame, M. Taniguchi, S. Ueda, K. Kobayashi, R. Kainuma, T. Shishido, K. Fukushima, and T. Kanomata, "Role of Electronic Structure in the Martensitic Phase Transition of Ni₂Mn_{1+x}Sn_{1-x} Studied by Hard-X-Ray Photoelectron Spectroscopy and *Ab Initio* Calculation," *Phys. Rev. Lett.*, vol. 104, p. 176401, Apr 2010. [Online]. Available: <http://link.aps.org/doi/10.1103/PhysRevLett.104.176401>
- [75] M. Kataoka, "Resistivity and magnetoresistance of ferromagnetic metals with localized spins," *Phys. Rev. B*, vol. 63, p. 134435, Mar 2001. [Online]. Available: <http://link.aps.org/doi/10.1103/PhysRevB.63.134435>
- [76] S. Chatterjee and S. Majumdar, *Mat. Sci. Forum*, vol. 635, pp. 97–102, 2010.
- [77] P. Pörsch, M. Kallmayer, T. Eichhorn, G. Jakob, H. J. Elmers, C. A. Jenkins, C. Felser, R. Ramesh, and M. Huth, "Suppression of martensitic phase transition at the Ni₂MnGa film surface," *Applied Physics Letters*, vol. 93, no. 2, p. 022501, 2008. [Online]. Available: <http://link.aip.org/link/?APL/93/022501/1>
- [78] K. Koyama, H. Okada, K. Watanabe, T. Kanomata, R. Kainuma, W. Ito, K. Oikawa, and K. Ishida, "Observation of large magnetoresistance of magnetic Heusler alloy Ni₅₀Mn₃₆Sn₁₄ in high magnetic fields," *Applied Physics Letters*, vol. 89, no. 18, p. 182510, 2006. [Online]. Available: <http://link.aip.org/link/?APL/89/182510/1>
- [79] Y. C. Shu, *Arch. Rational Mech. Anal.*, vol. 153, pp. 39–90, 2000.

- [80] Y. Luo, P. Leicht, A. Laptev, M. Fonin, U. Rüdiger, M. Laufenberg, and K. Samwer, "Effects of film thickness and composition on the structure and martensitic transition of epitaxial off-stoichiometric Ni–Mn–Ga magnetic shape memory films," *New Journal of Physics*, vol. 13, no. 1, p. 013042, 2011. [Online]. Available: <http://stacks.iop.org/1367-2630/13/i=1/a=013042>
- [81] H. Yu, S. Sanday, and B. Rath, "On the heterogeneous nucleation of martensite," *Materials Science and Engineering: B*, vol. 32, no. 3, pp. 153 – 158, 1995. [Online]. Available: <http://www.sciencedirect.com/science/article/pii/0921510795030050>
- [82] D. König, P. Buenconsejo, D. Grochla, S. Hamann, J. Pfetzinger-Micklich, and A. Ludwig, "Thickness-dependence of the B2–B19 martensitic transformation in nanoscale shape memory alloy thin films: Zero-hysteresis in 75nm thick $\text{Ti}_{51}\text{Ni}_{38}\text{Cu}_{11}$ thin films," *Acta Materialia*, vol. 60, no. 1, pp. 306 – 313, 2012. [Online]. Available: <http://www.sciencedirect.com/science/article/pii/S1359645411006744>
- [83] T. Kasuya, "Electrical resistance of ferromagnetic metals," *Progress of Theoretical Physics*, vol. 16, no. 1, pp. 58–63, 1956. [Online]. Available: <http://ptp.ipap.jp/link?PTP/16/58/>
- [84] N. Sakamoto, T. Kyômen, S. Tsubouchi, and M. Itoh, "Proportional relation between magnetoresistance and entropy suppression due to magnetic field in metallic ferromagnets," *Phys. Rev. B*, vol. 69, p. 092401, Mar 2004. [Online]. Available: <http://link.aps.org/doi/10.1103/PhysRevB.69.092401>
- [85] B. Raquet, M. Viret, E. Sondergard, O. Céspedes, and R. Mamy, "Electron-magnon scattering and magnetic resistivity in 3d ferromagnets," *Phys. Rev. B*, vol. 66, p. 024433, Jul 2002. [Online]. Available: <http://link.aps.org/doi/10.1103/PhysRevB.66.024433>
- [86] V. O. Golub, A. Y. Vovk, L. Malkinski, C. J. O'Connor, Z. Wang, and J. Tang, "Anomalous magnetoresistance in NiMnGa thin films," *Journal of Applied Physics*, vol. 96, no. 7, pp. 3865–3869, 2004. [Online]. Available: <http://link.aip.org/link/?JAP/96/3865/1>

BIBLIOGRAPHY

- [87] S. Zhang and P. M. Levy, "Conductivity and magnetoresistance in magnetic granular films (invited)," *Journal of Applied Physics*, vol. 73, no. 10, pp. 5315–5319, 1993. [Online]. Available: <http://link.aip.org/link/?JAP/73/5315/1>
- [88] B. M. Wang, L. Wang, Y. Liu, B. C. Zhao, Y. Zhao, Y. Yang, and H. Zhang, "Strong thermal-history-dependent magnetoresistance behavior in $\text{Ni}_{49.5}\text{Mn}_{34.5}\text{In}_{16}$," *Journal of Applied Physics*, vol. 106, no. 6, p. 063909, 2009. [Online]. Available: <http://link.aip.org/link/?JAP/106/063909/1>

8 Danksagung

Für die Unterstützung während meiner Doktorarbeit, die erst zum Gelingen dieser Arbeit geführt hat, bin ich zahlreichen Menschen zu großem Dank verpflichtet. An dieser Stelle möchte ich einigen von ihnen meinen besonderen Dank aussprechen. Als erstes gilt mein Dank meinem Betreuer Prof. Dr. Andreas Hütten, der es mir ermöglicht hat meine Doktorarbeit in der Arbeitsgruppe 'Thin Films & Physics of Nanostructures' zu schreiben und mit Ratschlägen und Anregungen erheblich zum Erfolg derselbigen beigetragen hat. Auch den Betreuern der verschiedenen Apparaturen, die ich im Zuge dieser Arbeit verwendet habe, bin ich für ihre geduldigen Einweisungen und die darüber hinausgehende Unterstützung bei Problemen und Unklarheiten zu großem Dank verpflichtet. Besonders hervorheben möchte ich hierbei Markus Meinert, der mich tatkräftig bei der Herstellung der dünnen Schichten, der Röntgenfluoreszenzanalyse, der Röntgendiffraktometrie und dem Bau des Hochtemperatursetups für die Röntgendiffraktometrie unterstützt hat.

Ebenfalls großer Dank gebührt meinem Diplomanden Niclas Teichert für die Untersuchung der Probenserie SERIES A während seiner Diplomarbeit und vieler hilfreicher Diskussionen. Bedanken möchte ich mich auch bei den Kollaborationspartnern dieser Arbeit. Zum einen sind dies Ercument Yüzüak, Ilker Dincer und Yalcin Elerman von der Ankara Universität. Ihre Aufenthalte in Bielefeld und meine Aufenthalte in Ankara sowie die Magnetisierungsmessungen haben wesentlich zum Gelingen dieser Arbeit beigetragen. Zum anderen sind dies Bernhard Krumme und Heiko Wende von der Universität Duisburg, die Magnetisierungsmessungen und XMCD Messungen an meinen Proben durchgeführt haben. Dank gilt auch Inga Ennen und Peter Schattschneider von der Technischen Universität Wien für die HRTEM und EMCD Messungen.

8. DANKSAGUNG

Bedanken möchte ich mich auch bei Bernhard Eickenberg, Anna-Lena Wolff, Frank Wittbracht und Niclas Teichert für das Korrekturlesen dieser Arbeit. Danken möchte ich auch den übrigen Mitgliedern der gesamten Etage D2 für das angenehme Arbeitsklima und die tatkräftige Unterstützung, auf die man zu jeder Zeit zählen konnte. Insbesondere sind hier meine Büro-Kollegen Peter Hedwig, Niclas Teichert und Markus Meinert zu nennen, die stets ein offenes Ohr für mich hatten und mir die Zeit sowohl in Bezug auf meine Arbeit als auch zwischenmenschlich sehr angenehm gestaltet haben.

Ich danke an dieser Stelle auch Prof. Dr. Thomas Huser, der sich bereit erklärt hat meine Arbeit als Zweitgutachter zu lesen und zu bewerten. Dem Bundesministerium für Bildung und Forschung (Project Number: TUR09/I01) danke ich für die finanziellen Mittel, von denen meine Forschung bezahlt wurde.

Bedanken möchte ich mich auch ganz besonders bei meiner Freundin Birte Steffen, die mich mit sehr viel Geduld während meiner Promotionsphase unterstützt hat. Bei Birte's Eltern, Volker und Annette Steffen, möchte ich mich bedanken für die Möglichkeit viele kreative Stunden im Garten verbringen zu können. Abschließend möchte ich mich ganz besonders bei meiner Familie bedanken, die mich Zeit meines Lebens in jeglicher denkbaren Weise unterstützt und mir dadurch erst diese Doktorarbeit ermöglicht haben.